Master's thesis

NTNU
Norwegian University of Science and Technology
Faculty of Natural Sciences
Department of Physics

Andrea Berge Kastellet

Effect of Ultrasound and Microbubble Treatment on Tumor Vasculature and Liposomal Uptake in Murine Cancer Models

Master's thesis in Applied Physics and Mathematics
Supervisor: Sofie Snipstad
Co-supervisor: Catharina de Lange Davies, Caroline Einen
June 2023

NTNU
Norwegian University of
Science and Technology

Andrea Berge Kastellet

Effect of Ultrasound and Microbubble Treatment on Tumor Vasculature and Liposomal Uptake in Murine Cancer Models

Master's thesis in Applied Physics and Mathematics
Supervisor: Sofie Snipstad
Co-supervisor: Catharina de Lange Davies, Caroline Einen
June 2023

Norwegian University of Science and Technology
Faculty of Natural Sciences
Department of Physics

NTNU
Norwegian University of
Science and Technology

Preface

This master thesis is submitted to the Norwegian University of Science and Technology (NTNU) at the Department of Physics, concluding my Master of Science degree in Applied Physics and Mathematics. Animal experiments were performed by Sofie Snipstad, Caroline Einen, Jessica Lage and Veronica Nordlund. The thesis is a continuation of the author's specialization project carried out during fall 2022. Parts of the sections *Theory, Materials* and *Methods* overlap with the project thesis. Illustrations are made by the author.

I would like to thank my supervisors and co-supervisors Sofie Snipstad, Catharina de Lange Davies and Caroline Einen for their guidance and support throughout this project. Your enthusiasm and knowledge have been truly inspiring and motivating. I would also like to express my appreciation to senior engineer Astrid Bjørkøy for microscope training, and for providing the Matlab script used for analysis. My gratitude is also expressed to the other master students in the biophysics group for our fellowship, and to the entire biophysics group. Attending the weekly Friday meetings have been valuable, and your inputs to the discussion of my results were very helpful. Lastly, thanks to my classmates and friends for being supportive during the previous five years.

Andrea Berge Kastellet
Trondheim, June 2023

Abstract

Purpose: The aim for this thesis was to investigate whether ultrasound and microbubble (USMB) treatment improves drug delivery in murine tumor models. Specifically, the effect of USMB on tumor perfusion and on liposomal uptake and microdistribution was evaluated. Additionally, contrast-enhanced ultrasound imaging (CEUS) was performed in order to characterize perfusion parameters in murine tumor models, to explore the potential of CEUS as a tool for patient stratification and to test the compatibility of confocal laser scanning microscopy (CLSM) and CEUS as methods for perfusion measurment.

Materials and Methods: Animal experiments were performed using subcutaneous colorectal (CT26), breast (4T1) and pancreatic (KPC) tumors in BALB/c (CT26 and 4T1) and B6/albino (KPC) mice. CEUS imaging was performed prior to treatment. Two microbubble (MB) platforms, Sonovue® and ACT®, were employed to study the effect of USMB on tumor perfusion. Sonovue treatment utilized US of MI = 0.5. To study uptake of NPs, liposomes were injected prior to USMB treatment. ACT treatment utilized US of MI = 0.2 both for activation and enhancement. The tumor vasculature was imaged by CLSM of functional vessels labelled with fluorescent lectin, and all tumor blood vessels stained by immunohistochemistry. Perfusion was measured by quantifying total amount of vessels and functional vessels to assess the fraction of perfused tumor blood vessels. Average NP extravasation distance in CT26 tumors was calculated from CLSM images of NPs and blood vessels.

Results: US and Sonovue treatment caused a significant reduction of perfused tumor blood vessels in CT26 and 4T1 tumors. ACT and US treatment demonstrated a weak trend, but no significant reduction on perfusion in CT26 tumors. Penetration and microdistribution of NPs in CT26 tumors was not affected by US and Sonovue treatment. However, overall NP uptake in USMB treated CT26 tumors increased significantly. On the contrary, NP uptake in treated 4T1 tumors was significantly reduced compared to controls. No significant difference was observed in KPC tumors.

Conclusion: The results emphasize the importance of characterizing the effect of USMB in different tumor models. USMB using Sonovue MBs and MI = 0.5 caused significantly reduced tumor perfusion and significantly improved NP delivery to CT26 murine tumors, suggesting that patients with colorectal adenocarcinoma might benefit from USMB treatment. CEUS imaging revealed potential biomarkers for patient stratification related to perfusion but not to NP tumor uptake.

Sammendrag

Hensikt: Målet med denne oppgaven var å undersøke om ultralyd- og mikroboblebehandling (USMB) kan forbedre levering av nanomedisin i murine tumormodeller. Nærmere bestemt ble effekten av USMB på tumorperfusjon og på opptak og mikrodistribusjon av liposomer evaluert. I tillegg ble kontrastforsterket ultralydavbildning (CEUS) utført for å karakterisere perfusjonsparametere i murine tumormodeller, for å utforske potensialet til CEUS som et verktøy for pasientstratifisering, og for å teste kompatibiliteten mellom konfokal laserskanningsmikroskopi (CLSM) og CEUS som metoderfor å måle perfusjon.
Material og metode: Dyreforsøk ble utført på subkutane kolorektale (CT26), bryst- (4T1) og bukspyttkjertelsvulster (KPC) i BALB/c-mus (CT26 og 4T1) og B6/albino-mus (KPC). CEUS-avbildning ble utført før behandling. De to mikrobobleplattformene Sonovue® og ACT® ble benyttet for å studere effekten av USMB på tumorperfusjon. Sonovue-behandling benyttet ultralyd med mekanisk indeks (MI) 0,5. For å studere opptak av nanopartikler, ble liposomer injisert før USMB-behandling. ACT-behandling benyttet ultralyd med MI = 0,2 både under aktivering og forsterkning. Tumorvaskularisering ble avbildet ved hjelp av CLSM av funksjonelle blodårer som ble merket med fluorescerende lektin, og alle tumorblodårer som ble merket ved immunhistokjemisk farging. Perfusjonen i tumoren ble målt ved å kvantifisere total mengde blodårer og funksjonelle blodårer, for så å regne ut andelen av perfunderte tumorblodårer. Gjennomsnittlig ekstravasasjonsdistanse for liposomer i CT26-svulster ble beregnet utifra CLSM-bilder av liposomer og blodårer.
Resultater: Ultralyd- og Sonovue-behandling førte til signifikant reduksjon av perfunderte blodårer i CT26- og 4T1-tumorer. Ultralyd- og ACT-behandling viste en svak trend, men ingen signifikant reduksjon av perfusjon i CT26-svulster. Penetrasjon og mikrodistribusjon av liposomer i CT26-svulster ble ikke påvirket av ultralyd- og Sonovue-behandlingen. Imidlertid ble det observert en signifikant økning i totale opptaket av liposomer i USMB-behandlede CT26-tumorer. Til forskjell fra CT26, ble liposomopptaket i behandlede 4T1-tumorer signifikant redusert sammenlignet med kontrollene. Ingen signifikant forskjell ble observert i KPC-tumorer.
Konklusjon: Resultatene understreker viktigheten av å karakterisere effekten av USMB-behandling i ulike tumormodeller. USMB med Sonovue-mikrobobler og MI = 0,5 forårsaket betydelig redusert tumorperfusjon og betydelig forbedret levering av liposomer til murine CT26-tumorer, som igjen kan antyde at pasienter med kolorektal kreft kan ha nytte av USMB-behandling. CEUS-avbildning avdekket potensielle biomarkører for pasientstratifisering relatert til perfusjon, men ikke relatert til liposomopptak.

Abbreviations

Ab Antibody

ACT Acoustic Cluster Therapy®

AF647 Alexa Fluor 647

ARF Acoustic Radiation Forces

BSA Bovine Serum Albumin

BV Blood Vessel

CD31 Anti-CD31

CEUS Contrast Enhanced Ultrasound

CLSM Confocal Laser Scanning Microscopy

CMIC Cellular and Molecular Imaging Core Facility

EC Endothelial Cell

ECM Extracellular Matrix

ED Extravasation Distance

EPR Enhanced Permeability and Retention

FBV Functional Blood Vessel

FITC-LEL Fluorescein Isothiocyanate-Labeled Lectin

HES Hematoxylin Erythrosine Saffron

IFP Interstitial Fluid Pressure

IgG Immunoglobulin G

IgG-AF647 Immunoglobulin G Conjugated AF647

IHC Immunohistochemistry

MB Microbubble

MI Mechanical Index

NA Numerical Aperture

NP Nanoparticle

PBS Phosphate Buffered Saline

PDAC Pancreatic Ductal Adenocarcinoma

PE Peak Enhancement

PMT Photomultiplier Tube

PRF Pulse Repetition Frequency

QOF Quality of Fit

ROI Region of Interest

RPM Revolutions Per Minute

RT Rise Time

SD Standard Deviation

TNBC Triple-Negative Breast Cancer

US Ultrasound

USMB Ultrasound and Microbubble

WiAUC Wash-in Area Under Curve

WiR Wash-in Rate

Contents

Abbreviations i

1 Introduction **1**

2 Theory **3**

2.1 Cancer 3

2.2 Barriers to Cancer Treatment and Drug Delivery 4

2.3 Nanoparticle Drug Delivery Systems 5

2.4 Vasculature 6

2.4.1 Normal Vasculature 6

2.4.2 Tumor Vasculature 7

2.4.3 Tumor Perfusion 9

2.5 Tumor Models 9

2.5.1 CT26 Murine Colorectal Cancer Model 9

2.5.2 4T1 Murine Breast Cancer Model 10

2.5.3 KPC Murine Pancreatic Ductal Adenocarcinoma Cancer Model . . . 10

2.6 Principles of Ultrasound 11

2.7 Contrast-enhanced Ultrasound Imaging 12

2.8 Biophysical Effects of Ultrasound 13

2.9 Ultrasound and Microbubble Treatment for Drug Delivery 15

2.10 Acoustic Cluster Therapy® . . . 16
2.11 Immunohistochemical Staining . . . 17
2.11.1 Direct and Indirect Immunofluorescence . . . 18
2.12 Fluorescence Microscopy . . . 18
2.13 Confocal Laser Scanning Microscopy . . . 19

3 Materials **21**

3.1 MicroMarker™ . . . 21
3.2 Sonovue® . . . 21
3.3 ACT® formulation . . . 21
3.4 Liposomes . . . 22
3.5 Fluorescently Labeled Lectin . . . 22
3.6 Anti-CD31 . . . 22
3.7 IgG-AF647 . . . 23

4 Methods **24**

4.1 Cell Cultures . . . 24
4.2 Implantation of Cancer Cells . . . 25
4.3 CEUS . . . 25
4.3.1 CEUS Imaging . . . 25
4.3.2 CEUS Analysis . . . 26
4.4 Effect of USMB on Fraction of Functional Tumor Blood Vessels . . . 27
4.4.1 US and Sonovue Treatment of CT26 and 4T1 Animals . . . 27
4.4.2 US and ACT Treatment of CT26 Animals . . . 28
4.4.3 Tumor Sectioning . . . 29
4.4.4 Immunohistochemical Staining of Blood Vessels . . . 30

4.4.5 CLSM of Blood Vessels and HES-stained sections 31
4.4.6 Processing and Analysis of Blood Vessel Images 33
4.5 Effect of USMB on Uptake and Microdistribution of Liposomes 36
4.5.1 Animal Experiment 36
4.5.2 Tumor Sectioning 38
4.5.3 Analysis of Pearl Data 38
4.5.4 CLSM of NPs and Blood Vessels 38
4.5.5 NP Extravasation Distance 39
4.6 Statistical Analysis and Plotting 42

5 Results **43**

5.1 CEUS 43
5.1.1 CEUS Curves 43
5.1.2 CEUS Parameters 45
5.1.3 Relationship between CEUS Parameters and Tumor Weight 49
5.2 Effect of US and Sonovue on Fraction of Functional Tumor Blood Vessels . 50
5.2.1 HES Images 50
5.2.2 CLSM Blood Vessel Single Images 51
5.2.3 CLSM Tile Scans of CT26 and 4T1 Tumors 52
5.2.4 Total Amount of Blood Vessels and Fraction of Functional Blood Vessels for CT26 Tumors 53
5.2.5 Total Amount of Blood Vessels and Fraction of Functional Blood Vessels for 4T1 Tumors 55
5.2.6 Relationship between Fraction of Functional Blood Vessels and Total Amount of Blood Vessels 57
5.2.7 Relationship between Fraction of Functional Blood Vessels and Tumor Weight 59

5.2.8 Relationship between CEUS Parameters and Fraction of Functional Blood Vessels . . . 61

5.2.9 Relationship between CEUS Parameters and Total Amount of Blood Vessels . . . 62

5.3 Effect of US and ACT on Fraction of Functional Tumor Blood Vessels . . . 63

5.3.1 CLSM Tile Scans . . . 63

5.3.2 Total Amount of Blood Vessels and Fraction of Functional Blood Vessels . . . 64

5.3.3 Relationship between Fraction of Functional Blood Vessels and Total Amount of Blood Vessels . . . 65

5.3.4 Relationship between Fraction of Functional Blood Vessels and Tumor Weight . . . 67

5.4 Effect of USMB on Uptake and Microdistribution of Nanoparticles in Tumors 68

5.4.1 Nanoparticle Uptake in Tumors . . . 68

5.4.2 CLSM Images of Blood Vessels and NPs . . . 70

5.4.3 Nanoparticle Extravasation Distance . . . 70

5.4.4 Relationship between Nanoparticle Uptake and CEUS data . . . 73

6 Discussion **76**

6.1 CEUS . . . 76

6.2 Effect of USMB Treatment on Tumor Perfusion . . . 78

6.2.1 Effect of US and Sonovue on Tumor Perfusion . . . 78

6.2.2 Effect of US and ACT on Tumor Perfusion . . . 80

6.2.3 Relationship between Tumor Vasculature Parameters . . . 80

6.2.4 Relationship between Tumor Vasculature Parameters and CEUS . . . 81

6.3 Effect of USMB on Uptake and Microdistribution of Liposomes . . . 82

6.3.1 Relationship between CEUS and Liposomal Uptake in Tumors . . . 83

6.4 Implications and Clinical Relevance of USMB for Drug Delivery 84

6.5 Future Work 84

7 Conclusion **86**

A Tables **94**

A.1 CEUS Data 94

A.2 Vasculature Parameters 100

A.3 Tumor Uptake Data from Pearl 103

A.4 Nanoparticle Extravasation Data 104

A.5 Tumor Weight 106

A.6 Correlation Data 106

A.6.1 Fraction of Functional Blood Vessels and Total Amount of Blood Vessels 106

A.6.2 Tumor Weight and Fraction of Functional Blood Vessels 107

A.6.3 CEUS Parameters and Vasculature Parameters 108

A.6.4 Pearl Data and CEUS Parameters 109

B IHC Staining Protocol **110**

C ImageJ Macro Scripts **112**

C.1 Nanoparticle Macro Script 112

C.2 Blood Vessel Macro Script 112

D Matlab Script for Extravasation Distance **113**

Chapter 1

Introduction

Cancer is the second leading cause of death worldwide after cardiovascular diseases [1], accounting for 10 million deaths globally in 2020 [2]. In the course of a human lifetime, the chance of developing cancer is 40% [3]. Common cancer treatments include chemotherapy, surgery, radiation therapy and immunotherapy. Although significant advancements have been made in the field of cancer therapy during recent years, efficient cancer treatment remains a challenge and is a highly active research area.

Chemotherapeutic drugs are often unspecific and accumulate in other organs than the tumor, inducing harmful side effects in healthy tissue. Encapsulating drugs in nanoparticles (NPs) has been proven to enhance delivery to the tumor. Using NPs as drug carriers enables drug-optimized design, entails high drug-load capacity, prolonged circulation time, reduction of cytotoxic side effects, and benefit from the tumor specific enhanced permeability and retention (EPR) effect. NPs can also be modified to target cancer-specific cells. Although using NPs as drug carriers has demonstrated improved delivery compared to free drugs, the fraction of drug accumulated in the tumor is still remarkably low, and has been suggested as low as 0.7 % [4]. Research has demonstrated that an even lower fraction of the injected drug, 0.0014 %, actually reaches the cancer cells [5].

Intravenously administered drugs or drug-loaded NPs encounter several biological barriers that impede efficient delivery to the cancer cells. A strategy to overcome these barriers is combining USMB and drug-loaded NPs. Ultrasound and microbubble (USMB) treatment has emerged as a promising approach to improve delivery of drug-loaded NPs to solid tumors. Promising results have been demonstrated pre-clinically [6][7] as well as in clinical trials [8][9].

It is well established that ultrasound (US) combined with microbubbles (MBs) induce var-

ious biophysical effects in biological tissue. MBs will oscillate upon US exposure, denoted as cavitation. Cavitation can cause effects that can be used for therapeutic applications. Among them is sonoporation, a collective term for creation of cavitation-induced pores in the endothelial cell membrane [10]. Endothelial cells are constituents of the blood vessel wall. Pore formation increases permeability of the blood vessel wall, and facilitates enhanced drug delivery. Additionally, cavitation can induce perfusion changes. Perfusion changes involve substantial effects such as vascular shutdown and re-opening of collapsed blood vessels [11].

The overall aim of this thesis was to evaluate the effect of USMB treatment on tumor perfusion and tumor uptake of NPs in murine tumor models, in order to assess whether USMB can be used to enhance delivery of drugs and NPs to tumors. Different cancer types possess different biological features and composition that are likely to affect how the tumor responds to USMB treatment. Such variables include various amount and composition of blood vessels, connective tissue and immune cells. Therefore, the experiments involved several murine tumor models to investigate which cancers might benefit from USMB. The employed tumor models were colorectal (CT26), breast (4T1) and pancreatic (KPC).

The first objective was to study the effect of USMB treatment on tumor perfusion in 4T1 and CT26 tumors. The motivation to investigate these two tumor models was the assumed different degree of vascularization. In particular, USMB treatment was performed using two different MBs - Sonovue® and ACT®. Sonovue is a commonly used contrast imaging agent, while ACT is a novel MB platform specifically designed for drug delivery applications. All tumor blood vessels and functional blood vessels were labelled with fluorescent dyes, and tumor sections were imaged by confocal laser scanning microscopy (CLSM). Tumor perfusion was assessed by image analysis, quantifying the fraction of functional tumor blood vessels.

The second objective was to determine whether USMB treatment improves uptake of NPs in CT26, 4T1 and KPC tumors. The utilized NPs were liposomes. Specifically, the average NP extravasation distance (ED) and NP distribution was calculated, and tumor uptake was assessed via whole animal optical imaging. NP ED and distribution was measured by analysing CLSM images of fluorescently labelled NPs and blood vessels.

Characterization of the different tumor models in terms of perfusion was also done by contrast-enhanced ultrasound imaging (CEUS). The purpose was to explore the potential of CEUS as a stratification tool to determine which patients that will benefit from USMB treatment. Additionally, CLSM and CEUS data were compared to assess whether these are comparable techniques for perfusion measurement.

Chapter 2

Theory[1]

2.1 Cancer

Cancer is a group of diseases arising as a result of uncontrolled growth of abnormal cells. These abnormal cells can form tumors that are either malignant (cancerous) or benign (not cancerous). Metastasis is the process where the cancer cells spread out and invade other parts of the body. Accumulation of gene mutations is what causes of cancer. Gene mutations are either hereditary, can occur during cell division or from external substances as radiation and chemicals [13]. Several hallmarks of cancer have been established, describing biological traits that characterize most cancers. That includes self-sufficiency in growth signals, insensitivity to anti-growth signals, sustained angiogenesis, avoiding immune destruction, evading apoptosis, limitless replicative potential and activating invasion and metastasis, and deregulating cellular energetics [14]. There are several different options for cancer treatment. Among them are surgery, chemotherapy, radiation therapy, immunotherapy and hormone therapy. Treatment can consist of one of the mentioned, or combining multiple of them. Improvement of cancer treatment remains a challenge for the scientific community and is a highly active research area.

[1] Parts of this section overlap with the authors project thesis[12].

2.2 Barriers to Cancer Treatment and Drug Delivery

Typically, a very small amount of chemotherapeutic drugs accumulates in the tumor, and an even smaller amount is delivered particularly to the cancer cells [15]. Instead the drugs are often found in off-target organs, causing cytotoxic side effects. Encapsulating drugs in nanoparticles (NPs) is a method suggested to enhance the delivery of drugs to solid tumors, and has shown promising results [16] [17]. Although drug loaded NPs have achieved better fractions of delivered drugs than conventional chemotherapy, still only a small amount of the drug accumulates in the tumor. Studies have demonstrated that 0.7% [4] of injected drug dose is delivered to the tumor, an that only 0.0014% is further delivered to the cancer cells [5].

For a drug to reach the tumor and the cancer cells, it must first navigate through the vascular network. Then it must extravasate over the capillary wall before penetration of the extracellular matrix (ECM). Finally, the drug must be taken up by the cancer cells [11]. These three barriers will be discussed in more detail in the following paragraphs.

The tumor vasculature has a hetereogenous and tortuous structure, where the blood vessels are leaky, of varying size and shape, and have an alternating blood flow. This may cause challenges during transport of the drug through the tumor vasculature. The circulation time of the drug must be sufficiently long for the drug to accumulate in the tumor. Also, the drug must not directly accumulate in other organs, such as the liver and kidneys.

Tumor capillaries often have a discontinuous blood vessel wall, where contact between the basement membrane, endothelial cells (ECs) and pericytes is lacking. This causes blood vessels with high permeability. Additionally, tumor tissue lacks functional lymphatic vessels and thus lymphatic drainage. This leads to retention of macromolecules, e.g. drugs and NPs. The enhanced permeability end retention (EPR) effect is a tumor specific effect causing macromolecules to retain in the tumor after extravasating. Hence, the EPR effect facilitates tumor accumulation of NPs.

Transport of NPs through the ECM is mainly driven by convection. Due to leaky vasculature, deficient lymphatic drainage and dense ECM, the interstial fluid pressure (IFP) is high in tumors. Elevated IFP impairs transcapillary transport via convection, since the high IFP does not allow macromolecules to be transported down a pressure gradient [18]. Hence, delivery of drugs and NPs to tumor cells is impaired of high IFP.

The ECM consists of several non-cellular macromolecules, such as collagens, fibronectin, elastin, proteoglycans and hyaluronan [19]. In order to reach the tumor cells, the drug

must penetrate through the ECM [20]. Tumors having a dense ECM impedes drug penetration and delivery. Hyaluronan and collagen provide the ECM with mechanical support. Elevated levels of hyaluronan and collagen are often present in tumors, resulting in a denser and stiffer ECM.

Finally, the drug must penetrate the plasma membrane of the cancer cell. Diffusion ensures this for small molecules, while larger molecules such as NPs require an active mechanism. Endocytosis is the main mechanism for NPs to cross the plasma membrane [21].

2.3 Nanoparticle Drug Delivery Systems

An emerging application of nanomedicine is using NPs as drug carriers, which offers considerable advantages compared to "free" drugs. Being encapsulated in a NP, the drug is protected from premature degradation and interaction, which improves the circulation time [22]. NPs provide a more controlled delivery and are more likely to accumulate in and penetrate into the target tissue (e.g. tumor tissue) than free flowing drugs [22]. Reduced accumulation of drugs in healthy tissue implies reduction of cytotoxic side effects. NP drug delivery systems can be designed to fit the target and drug load, since the size, shape and composition of the nanocarrier is adjustable. Examples of the multifunctionality of NPs are illustrated in Figure 2.1. The size of NPs can vary from 1 to 200 nm, and can be composed of different materials such as lipids, metal, polymers or dendrimers. Additionally, nanoparticles allow modification of their surface with molecules as for example targeting ligands or fluorescent dyes.

Passive targeting exploits solely the presence of the previously described enhanced permeability and retention (EPR) effect, which is specific for solid tumors. Active and triggered targeting has been suggested to improve the accumulation and retention of nanoparticles in tumor tissue [16][17]. Active targeting facilitates uptake of drug loaded nanoparticles by actively targeting them to receptors that are expressed on the target cells [23]. This is achieved by modifying the surface of the nanoparticles with ligands binding to these specific receptors. However, studies have found lower nanoparticle accumulation than expected, and suggests that the particles might bind to the first cancer cells they get in contact with after extravasating from the blood vessel. Thus, active targeting might hinder nanoparticle extravasation further through the tumor tissue [24] [25]. Triggered targeting exploits nanocarriers that are responsive to certain stimuli, e.g. temperature, pH or ultrasound [26].

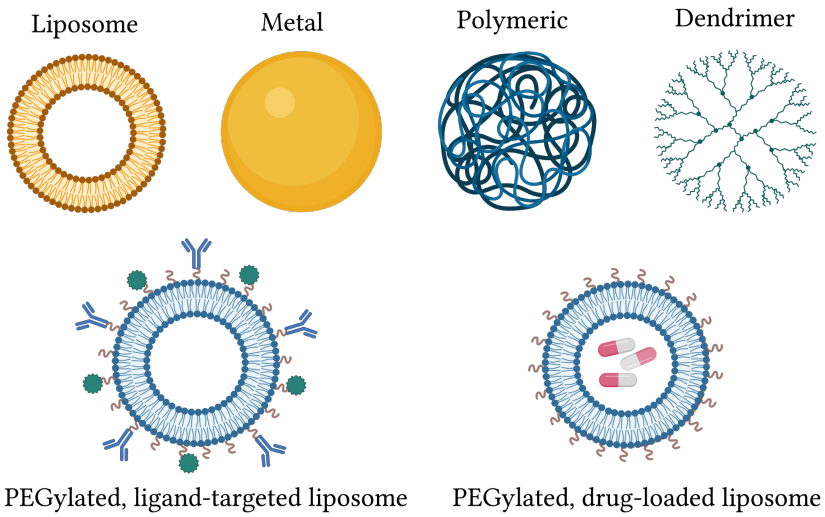

Figure 2.1: Illustration of different types of NPs and how they can be modified. NPs can be composed of different materials, and can have different payloads, e.g. drugs. The surface can be modified with targeting ligands. Figure created with BioRender.com.

.

2.4 Vasculature

2.4.1 Normal Vasculature

Normal blood vessels are structured in a hierarchically manner. Arteries branch into arterioles, and carry blood *from* the heart. Veins branch into venules, and carry blood *to* the heart. Capillaries are the smallest blood vessels, and connect the arterioles and venules. The blood vessel wall of capillaries consists of ECs, while for larger vessels it also consists of smooth muscle cells [27]. The structure and branching system of normal and tumor vasculature is illustrated in Figure 2.2 and Figure 2.3.

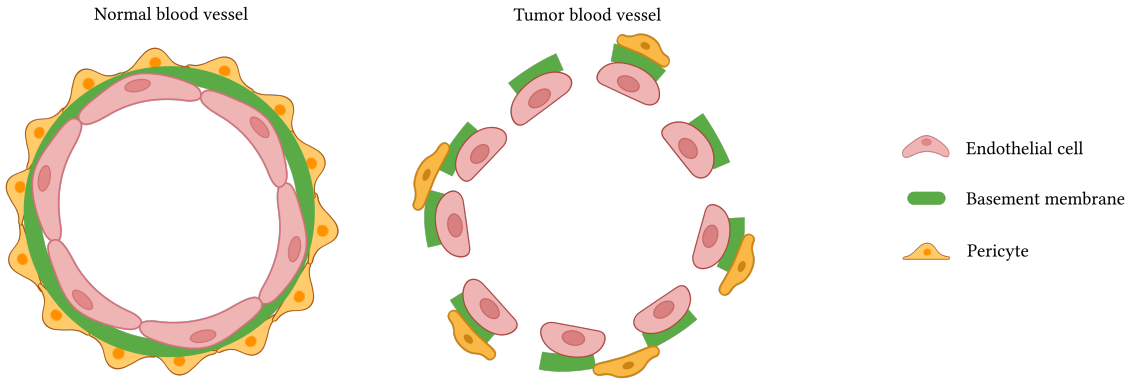

Figure 2.2: Illustration of the cross section of normal and tumor blood vessels, composed of endothelial cells, basement membrane and pericytes. Figure created with BioRender.com.

.

2.4.2 Tumor Vasculature

To grow beyond a diameter of approximately 1 to 2 mm, the tumor needs a blood supply [28]. As the tumor grows, it will at some point lack blood supply, which provides it with oxygen and nutrients, and also removes waste products. This causes hypoxia in the tumor. Hypoxia generates angiogenic signaling molecules such as hypoxia-inducible factors (HIFs). HIF up-regulates vascular endothelial growth factor (VEGF), which in turn activates the blood vessel formation processes angiogenesis, co-option and vasculogenesis [29]. Angiogenesis is the process where a tumor develops its own vascular network by creating branches from already existing blood vessels, and the most frequently occurring vessel formation process. Co-option of existing blood vessels exploits already existing vasculature. Vasculogenesis generates new vessels by recruitment of ECs, for instance from bone marrow [29].

Unlike normal blood vessels, the new tumor vessels are not organized hierarchically, but are heterogeneously distributed. Typically, they are unevenly shaped, and also have blind ends. Figure 2.3 illustrates the different branching trends between normal and tumor vasculature. Also, tumor vessels are leaky, meaning that the epithelial cells, basement membrane and pericytes are discontinuous and not properly connected. Figure 2.2 illustrates the difference between normal and tumor blood vessels.

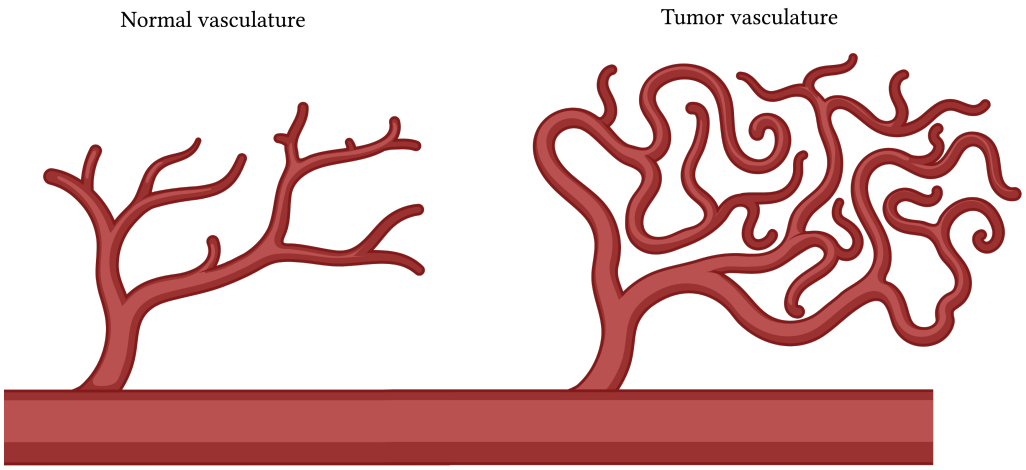

Figure 2.3: Illustration showing the branching of normal and tumor vasculature. Figure created with BioRender.com.

.

2.4.3 Tumor Perfusion

Blood perfusion denotes the flow of fluid through the vascular system, more precisely the blood volume passing through a unit volume of tissue per unit time. Perfused vessels are here denoted as functional vessels. In the previous sections, leaky and intricated capillaries, poor drainage and high IFP were introduced as characteristics of the tumor vasculature. These are also the reasons to why tumor tissue typically is less perfused than normal tissue. Elevated solid stress as a consequence of rapid tumor growth can cause collapse of blood vessels, and reduce perfusion [30]. High production of ECM components may also lead to vascular shutdown and reduced perfusion.

2.5 Tumor Models

Several kinds of murine tumor models are commonly used in cancer research. Some of these are syngeneic, xenograft, genetically engineered and spontaneous models. Syngeneic models involve implanting murine-derived tumor cell lines into immunocompetent mice with a similar genetic background [31]. These models allow researchers to study interactions between the immune system and the tumor, since both components are derived from the same species. In the experiments of this thesis, syngeneic tumor models were used. Xenograft models can be either cell line-derived or patient-derived. In cell line-derived models, cancer cell lines grown in vitro are implanted into immunodeficient mice [32]. This model is limited by lack of immune response. Patient-derived xenografts attempt to solve this limitation, by transplanting tumor tissue directly from a patient into immunodeficient mice. In genetically engineered tumor models (GEMMs), genetically modified mice spontaneously initiate and develope new tumors in a immunocompetent microenvironment [33]. Certain mouse strains have a predisposition to spontaneously develop tumors as a result of specific genetic mutations. Thus, such spontaneous tumor models occur naturally.

.

2.5.1 CT26 Murine Colorectal Cancer Model

One in 20 people will be diagnosed with colon cancer within their lifetime, making it one one of the most frequent cancer types. The most common treatment for colon cancer is surgery, but also chemotherapy and chemotherapy combined with radiation therapy is practiced [34]. The murine CT26 model is modelling human colorectal carcinoma cancer, and the cell line is derived from BALB/c mice. Genomic analysis has among other findings

demonstrated muations in the Kras gene and lack of Egfr expression [35].

CT26 tumors grow rapidly, hence they require great access of oxygen and nutrients, which again causes high production of angiogenic factors. In turn, high production of angiogenetic factors lead to quick and active formation of blood vessels [36]. CT26 tumors are characterized as well-vascularized and with a disorganized vascular network. Differences in vascularization between the periphery and center are also present. A higher rate of vessel growth in the periphery than the center has been demonstrated [36]. This implies a higher density of blood vessels in the periphery compared to the center. The density of functional vessels has also been found to be higher in the periphery than in the center [37].

2.5.2 4T1 Murine Breast Cancer Model

Breast cancer is the second most common cancer type among women [38], and the triple-negative breast cancer (TNBC) phenotype constitutes 17 % of the annually diagnosed breast cancers [39]. The 4T1 cell line is derived from BALB/c mice, sharing molecular features with metastatic human TNBC. It is an extensively used breast cancer mouse model [40]. The 4T1 cancer cells lack estrogen receptors (ER), progesteron receptors (PR) and epidermal growth factor receptor 2 (HER2), and is poorly immunogenic and metastatic, resembling the characteristics of human TNBC [40]. The microenvironment of 4T1 tumors is characterized by a chaotic vascular network with a heterogeneous blood vessel distribution, limited perfusion, and larger perfused vessels in the tumor periphery [41].

2.5.3 KPC Murine Pancreatic Ductal Adenocarcinoma Cancer Model

Pancreatic ductal adenocarcinoma (PDAC) is ranked as the fourth leading cause among cancer-related deaths [42]. Typically, the response to treatments such as chemotherapy and radiation therapy is limited, and tumors are often unresectable [43]. The murine KPC model is an established and clinically relevant model of pancreatic ductal adenocarcinoma [44]. Key mutations are found in the Kras and TP53 genes. The KPC model recapitulates many of the biological features of human PDAC [45]. Amongst them is hypovascularity and hypoxia, i.e. lack of sufficient vasculature and low levels of oxygen [46][47]. Another feature is a dense stroma, constituted by ECM components and mesenchymal cells. Resistance to chemotherapy can be attributed to these features.

2.6 Principles of Ultrasound

Ultrasound (US) includes the range of energies above 20 kHz, typically up to 20 MHz in clinical use, but theoretically up to 200 MHz. US is a commonly used imaging method for diagnostic purposes. However, US is also employed in therapeutic applications such as tumor ablating, physiotherapy, kidney stone comminution and drug delivery [48].

As the US beam enters and propagates through a medium, it encounters heterogeneities in the form of different tissue types, bones and organs with a characteristic acoustic impedance. Acoustic impedance describes the resistance the medium opposes to the US wave as it propagates, expressed as

$$Z = \rho c, \tag{2.1}$$

where ρ is the density and c is the speed of sound specific for the material. When the US wave encounters the interface between tissues, part of the wave will be reflected due to the difference in acoustic impedance, and this echo is the signal detected to form an image. The amplitude of the incidence US wave is reduced as a result of scattering, absorption, reflection, refraction and diffraction, which constitute the collective term *attenuation*. Attenuation of US waves in terms of pressure decrease is given by

$$p = p_0 e^{-\alpha z} \tag{2.2}$$

where p_0 is the pressure amplitude at $z = 0$, α is the attenuation coefficient and z is the distance from the transducer. The attenuation coefficient α is frequency dependent, in units of $\frac{dB}{cmMHz}$. Similarly, the acoustic intensity amplitude decreases exponentially as

$$I = I_0 e^{-2\alpha z}, \tag{2.3}$$

where I_0 is the intensity at $z = 0$. Water and US gel have low attenuation coefficients. Thus they are suitable mediums for conducting the US from probe to tissue. Mechanical index (MI) is a metric describing the relation between pressure, frequency and acoustic power, and is expressed as

$$MI = \frac{P}{\sqrt{f_c}}, \tag{2.4}$$

P being the pressure and f_c the center frequency of the US beam. To avoid unwanted bioeffects, MI = 1.9 is the maximum MI allowed for diagnostic imaging of humans [49].

The transducers on the US probe are responsible for both transmitting the US beam intro the medium and receiving the echoes to form an image. In transmit phase, the US beam is generated by transducers on the probe, which by the piezoelectric effect converts electric

energy to mechanical energy. When a voltage pulse is applied to the transducer, the piezo-element is distorted and emits an US pulse as it opposes the deformation and relaxes back to its initial state. In receive phase, the transducer exploits the inverse piezoelectric effect to receive and detect the echo. The incoming mechanical energy of the pressure wave is converted to an electric signal, and recorded. Further, an image forming process generates the resulting image.

2.7 Contrast-enhanced Ultrasound Imaging

Contrast-enhanced ultrasound imaging (CEUS) is a technique exploiting the mechanical properties of contrast agents when exposed to US. Perfusion and blood flow can not be imaged properly with B-mode US, since blood vessels are bad US scatterers. For this purpose, contrast agents of similar size as red blood cells can be utilized to visualize the movement of the blood. Typically, these are gas filled microbubbles (MBs) with a diameter of 3-6 µm, surrounded by a phospholipid shell. Before insonation, the MBs are injected to the organism. The most commonly used MB in clinic is Sonovue®. For small-animal CEUS, the MB MicroMarker™is the most commonly used contrast agent.

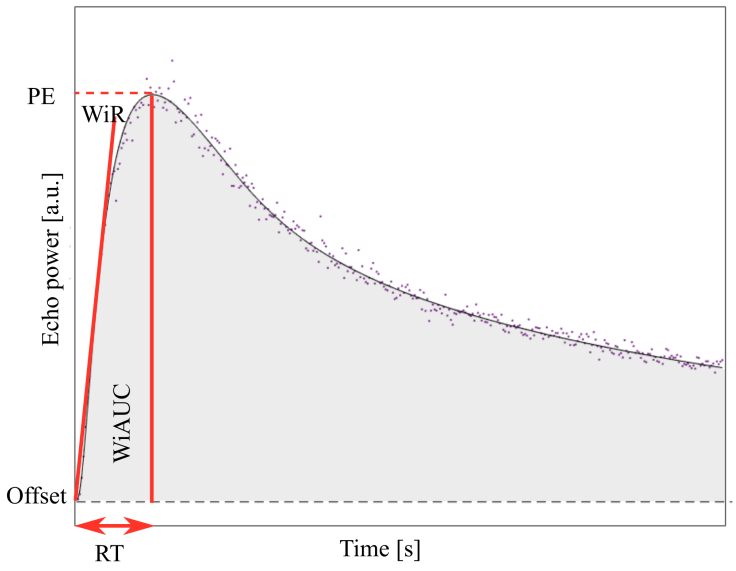

Figure 2.4: Linearized signal (dots) and curve fit (line) from one CEUS video as a function of time. Relevant CEUS parameters indicated are Peak enhancement (PE), rise time (RT), wash-in area under curve (WiAUC) and wash-in rate (WiR).

.

To visualize the MBs, their scattering properties are exploited. When exposed to ultrasound, the MBs will oscillate. Due to greater compression than expansion, a non-linear signal is generated. This non-linear signal from the MBs can be separated from signal from surrounding tissue, which mainly generates linear signal. One can distinguish between higher harmonic, ultra-harmonic and sub-harmonic components of the non-linear signal.

In order to quantify the perfusion, a curve is fitted to the linearized echo signal from the MBs. From the curve fit, several perfusion parameters can be calculated. The curve fit and linearized signal is displayed together with the perfusion parameters in Figure 2.4. Relevant parameters discussed in this thesis are peak enhancement (PE), rise time (RT), wash-in area under curve (WiAUC) and wash-in rate (WiR) [50]. Additionally, the wash-in perfusion index (WiPI) can be estimated, which is given by WiAUC/RT. PE is the maximum intensity of the curve, and is a marker of perfusion and blood volume. WiAUC is the area under the curve during wash-in of the contrast agent, and is also an indicator of blood volume. RT measures the time from when the first MBs enter the vasculature, until the maximum amount of MBs reside in the vasculature. WiR indicates the slope of the wash-in curve, and indicates the velocity of the blood flow.

2.8 Biophysical Effects of Ultrasound

The energy of US waves causes several biophysical effects in the insonated tissue. Upon US exposure, energy is transferred from the propagating wave to the tissue, causing two main biophysical effects to occur - thermal and mechanical effects. Thermal effects includes tissue heating from the absorbed energy. Mechanical effects include acoustic radiation forces (ARF) and cavitation. Figure 2.6 illustrates how cavitation and ARF can cause changes in the ECs and blood vessel wall, and thus increase vascular permeability.

Attenuation of US waves transfers energy to the exposed tissue. In turn, this creates a force in the propagation direction of the US wave. ARF affects all molecules in the blood vessel, and can push particles, fluids and tissue. MBs may be pushed towards or even through the cell membrane, as illustrated in Figure 2.6 (c). This creates shear stresses on the blood vessel wall, which in turn can cause the endothelial cells to detach from each other and thus increase permeability [51].

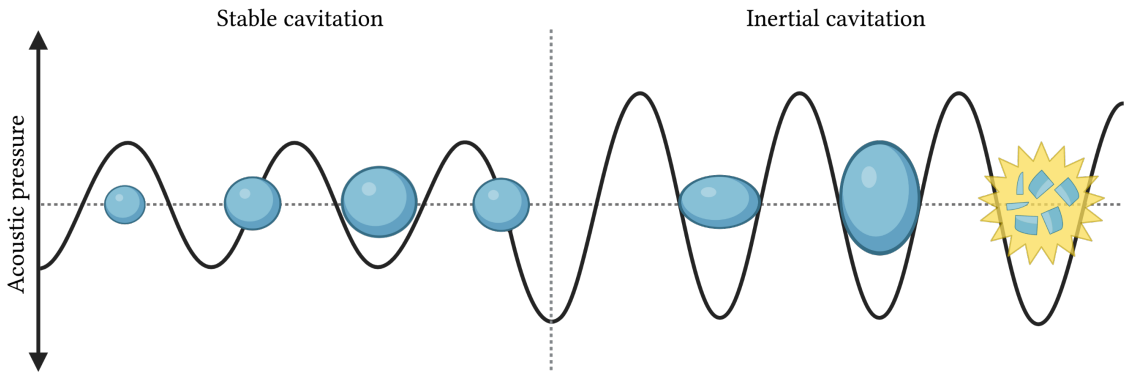

Figure 2.5: Illustration of MB oscillations in a US field, referred to as cavitation. Stable cavitation occurs at lower acoustic pressure, while inertial cavitation occurs at higher pressures and causes MB collapse. Figure created with BioRender.com.

.

Applications combining US and MBs, such as USMB treatment, exploit the effects caused by oscillating MBs. When MBs are insonated, they will oscillate in phase with the pressure field of the US waves [52], termed cavitation. The cavitation varies with the pressure of the US. Depending on the acoustic pressure, US can generate stable or inertial caviation, illustrated in Figure 2.5. Stable cavitation occurs at low pressures. The MBs will then expand and compress equally in all directions. As the MBs oscillate, they create shear stresses on the ECs that cause pore formation in the EC membrane, an thus potentially increase the permeability (Figure 2.6 (a)). Oscillating MBs create microstreams in the surrounding fluids, generating shear stresses that can lead to membrane ruptures (Figure 2.6 (b)). Inertial cavitation occurs at higher pressures. Here, the MB will expand more than it compresses. This will cause the MB to collapse due to greater inward forces than outward pressure of the MB gas. The collapse can generate a shock wave as a result of the sudden rise in pressure and temperature (Figure 2.6 (d)). If the MB collapse close to the blood vessel wall, a microjet can be created (Figure 2.6 (e)). A sufficiently large force generated by the microjet can disrupt the endothelial plasma membrane [52].

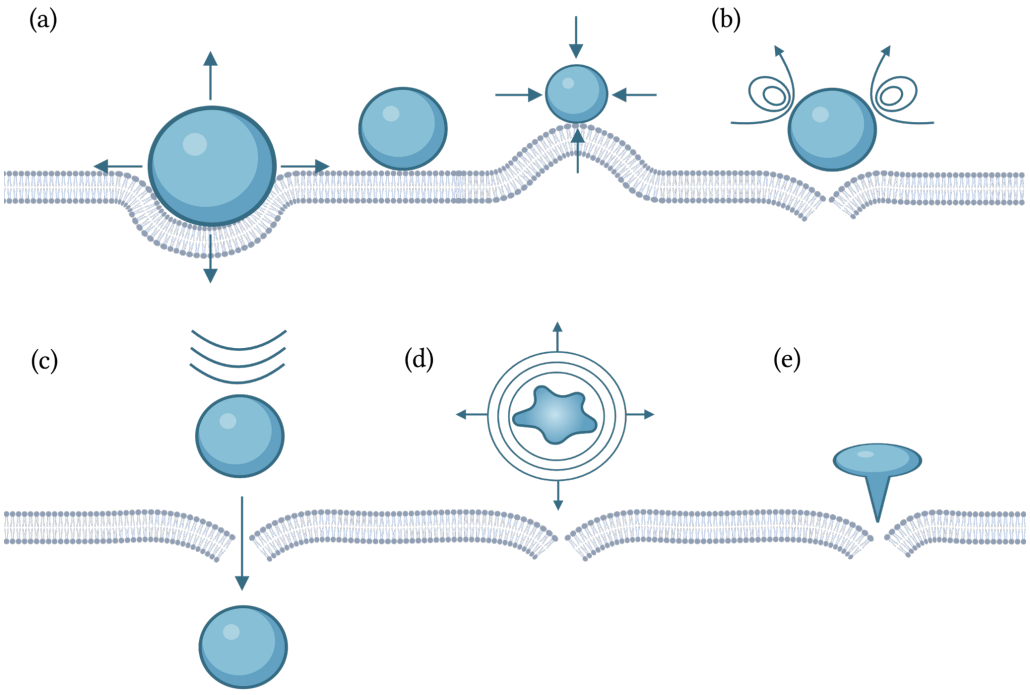

Figure 2.6: Biophysical effects of US. Stable cavitation can create pores in the EC membrane by MB oscillations pushing and pulling the membrane (a) or microstreams generated by the oscillations (b). ARF can push the MB towards or through the membrane (c). Inertial cavitation can cause collapsing MBs, creating a shock wave that in turn can rupture the membrane (d). If the collapse occurs close to the membrane, jet streams can create pores (e). Figure created with BioRender.com.

.

2.9 Ultrasound and Microbubble Treatment for Drug Delivery

Ultrasound and microbubble treatment combines US and microbubbles (MBs), and is a therapeutic application of US that has demonstrated promising results for improvement of drug delivery to tumors. Focusing of the US beam can deliver energy to delimited volumes, and induce mechanical and thermal biophysical effects, as described in the previous section. Typically, the US is pulsed to limit tissue heating and allow inflow of MBs. MI a relevant metric in USMB, as the acoustic pressure reflects the probability of cavitation. USMB employs different MB platforms. Among these is the commonly used contrast agent Sonovue®. Microbubble platforms can also be specifically designed for drug delivery, such as ACT® bubbles.

Sonopermeation denotes USMB induced effects in tissue and cells, including formation of pores in the cell membrane, opening of tight intracellular junctions, stimulated endocytosis, transcytosis and exocytosis, perfusion changes, and/or changes in the perivascular and extracellular space [53]. Studies have found various effects of USMB and sonopermeation, depending on the tissue model, the MI used, time after treatment and the type of MB used. Figure 2.6 illustrates how formation of pores in the endothelial membrane can be created as a result of US and MBs. Also, several studies have found that USMB causes macroscopic changes such as vascular shutdown, and hence decreased perfusion [54][11]. On the contrary, it has been demonstrated that USMB can cause mechanical reopening of disrupted blood vessels, and thus increase blood perfusion [55] [56].

USMB treatment has also exhibited enhanced delivery of drugs and NPs to tumors [57][58][59].

2.10 Acoustic Cluster Therapy®

Acoustic cluster therapy® (ACT) is a novel MB platform, specifically designed for US mediated drug delivery. The ACT formulation is composed of free flowing clusters of negatively charged, gas-filled MBs, and positively charged oil microdroplets [60]. Due to opposite charge, electrostatic attraction causes the the microbubbless and microdroplets to form clusters. US insonation activates the clusters, which undergo a phase shift from liquid to gas, and form larger bubbles. A low mechanical index is required for the activation to happen, typically MI$<$0.4 and frequency 1-10 MHz. The transformation occurs because the microbubble transfers energy to the microdroplet, inducing instant vaporisation of the oil. This causes formation of bubbles with a diameter of $20-30\,\mu m$,

After activation, low frequency (0.1-1 MHz) and low MI US is applied, referred to as enhancement US. The insonation induces oscillations of the activated bubbles. The working principle of ACT and US treatment is illustrated in Figure 2.7. Regular MBs used for USMB treatment are small and have correspondingly limited contact with the blood vessel wall. Since the ACT bubbles are larger than MBs as Sonovue, they have a significantly larger contact area with the blood vessel wall. The absolute volume displacement from the ACT bubble oscillations is three orders of magnitude larger than that of regular MBs [60].

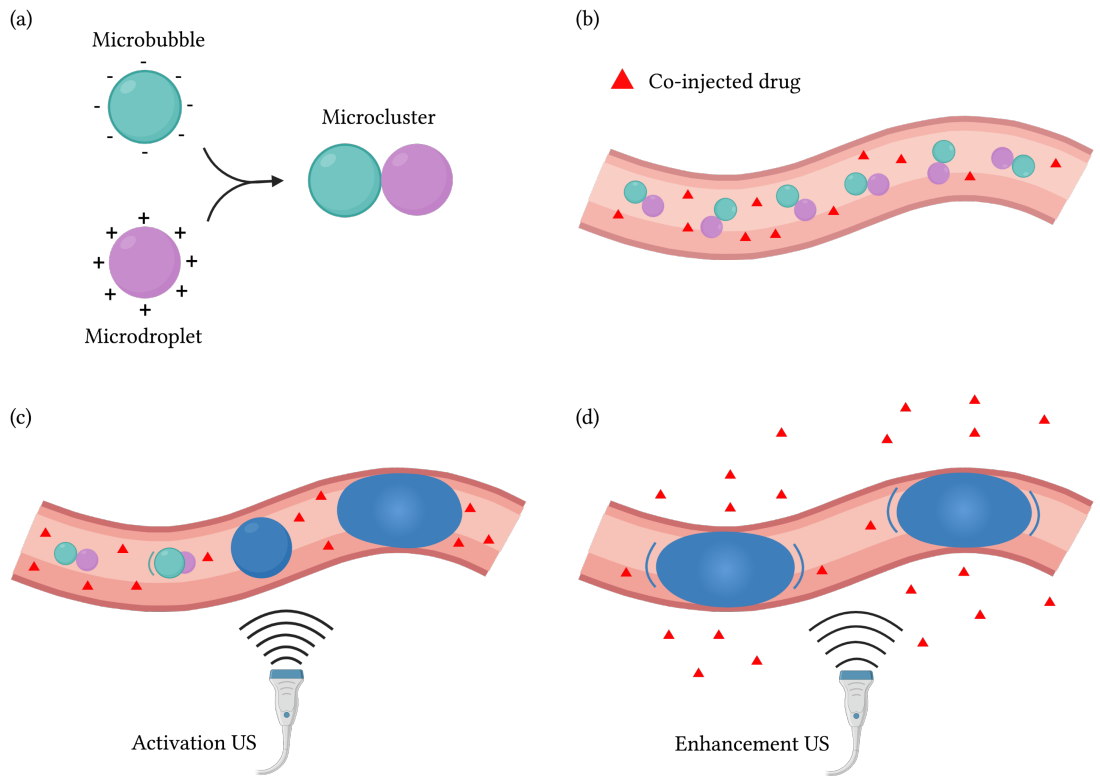

Figure 2.7: Illustration of the working principle of ACT and US treatment for drug delivery. Microbubbles and microdroplets form microclusters (a), that are injected to the vasculature along with a drug (b). Upon activation US the clusters form large bubbles (c). Enhancement US causes bubble oscillations (d), and might improve drug delivery. Figure created with BioRender.com.

.

Co-injection of drugs along with the ACT formulation has been demonstrated to enhance drug delivery to tumors [61]. Since the bubbles stay in the vasculature and hinder blood flow for 5-10 min post activation, wash out of the drug is also prevented. Hence, high concentration of the drug is maintained over a longer period of time, meaning longer time available for the drug to extravasate and penetrate through the tumor tissue.

2.11 Immunohistochemical Staining

Immunohistochemistry is a staining technique that uses immunofluorescence to visualize cellular components. It exploits that specific antibodies recognize and bind to specific antigens on specific cells. A fluorophore can be conjugated to the antibody, and in such a manner cellular components of interest can be imaged with fluorescence microscopy. The principle of fluorescence microscopy is described in more detail in the next section.

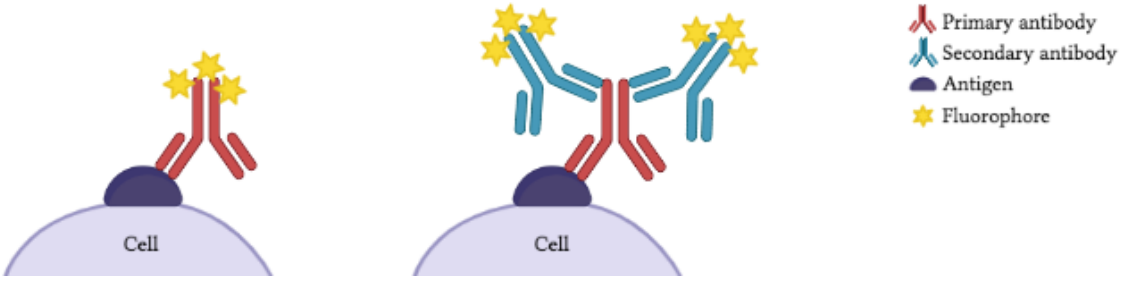

Figure 2.8: Direct (left) and indirect immunofluorescence. Direct immunofluorescence involves an fluorescent antibody binding to an antigen. In indirect immunofluorescence, a primary antibody binds to the cell, to which several fluorescent secondary antibodies can bind. Figure created with BioRender.com.

.

2.11.1 Direct and Indirect Immunofluorescence

There are two different approaches to IHC staining, illustrated in Figure 2.8. In direct immunofluorescence, an fluorescent labelled antibody binds directly to the antigen on the target cell. On the other hand, indirect immunofluorescence exploits a non-fluorescent labelled primary antibody that binds to the antigen [62]. The primary antibody has several binding sites to which fluorescent labelled secondary antibodies can attach. In other words, several fluorescent antibodies attach per antigen on the target molecule, whereas only one fluorescent antibody binds per antigen in direct immunofluorescence. Hence, indirect immunofluorescence is beneficial in terms of fluorescent signal intensity.

2.12 Fluorescence Microscopy

Fluorescence is the where absorption of light energy (a photon) by a molecule is followed by emission of part of the absorbed energy (another photon) [63]. The energy is not conserved, meaning that the emitted photon has lower energy than the absorbed photon, and hence longer wavelength, since photon energy is given by

$$E = hf = hc\lambda, \tag{2.5}$$

where h is Planck's constant, f the frequency, c the speed of light and λ the wavelength of the photon.

The energy change is termed Stokes shift, and involves several molecular transitions [63]. A Jablonski energy diagram describes these changes of electron states in a molecule. Figure

2.9 illustrates a simplified Jablonski diagram, showing the excitation from the ground state S0 to excited state S2. The electron then loses its energy by internal conversion and vibrational relaxation. Then, the reverse transition from S1 to S0 emits a photon, which in turn can be detected.

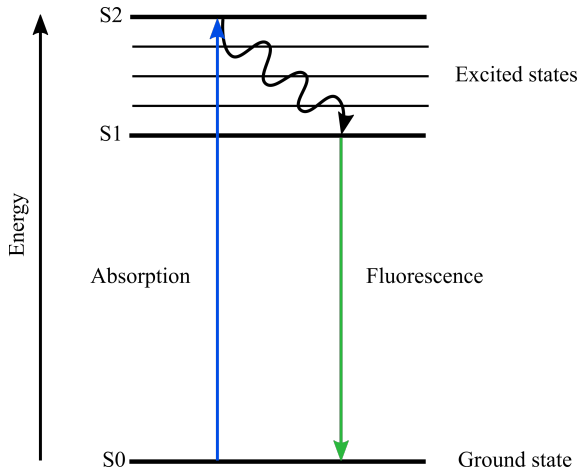

Figure 2.9: Jablonski diagram.

.

2.13 Confocal Laser Scanning Microscopy

Confocal laser scanning microscopy (CLSM) is a powerful technique for imaging fluorescently labeled specimens. The key feature of CLSM is the pinhole [64]. The pinhole ensures that only light from the focal plane will be detected. This provides a considerably improved resolution compared to that of epifluorescence microscopy, where light from the entire thickness of the specimen is detected. Hence, CLSM enables a detailed visualization of cellular structures and components [65].

The working principle of confocal laser scanning microscopy is illustrated in Figure 2.10. Light from a light source, usually a laser, passes through a illumination pinhole that focuses the laser light. A dichroic mirror reflects the light, which is then focused into the specimen by an objective lens. Emitted fluorescence from the specimen passes through the dichroic mirror. Further, the light passes through the confocal pinhole, and reaches the detector, typically a photomultiplier tube (PMT). Light from below or above the focal plane is eliminated by the confocal pinhole, which works as a spatial filter. Essentially, the illumination pinhole, the focused point in the specimen, and the confocal pinhole in front of the detector are confocal with one another [64]. The light reaching the detector produces a voltage signal that is proportional to the intensity of the incoming photons. The pinhole

diameter can be adjusted. Decreasing the pinhole size means that the resolution improves, but also means less detected light since more light is rejected by the pinhole. To create an image, the focus spot of the laser light moves point by point, scanning across the entire section of the specimen to be imaged.

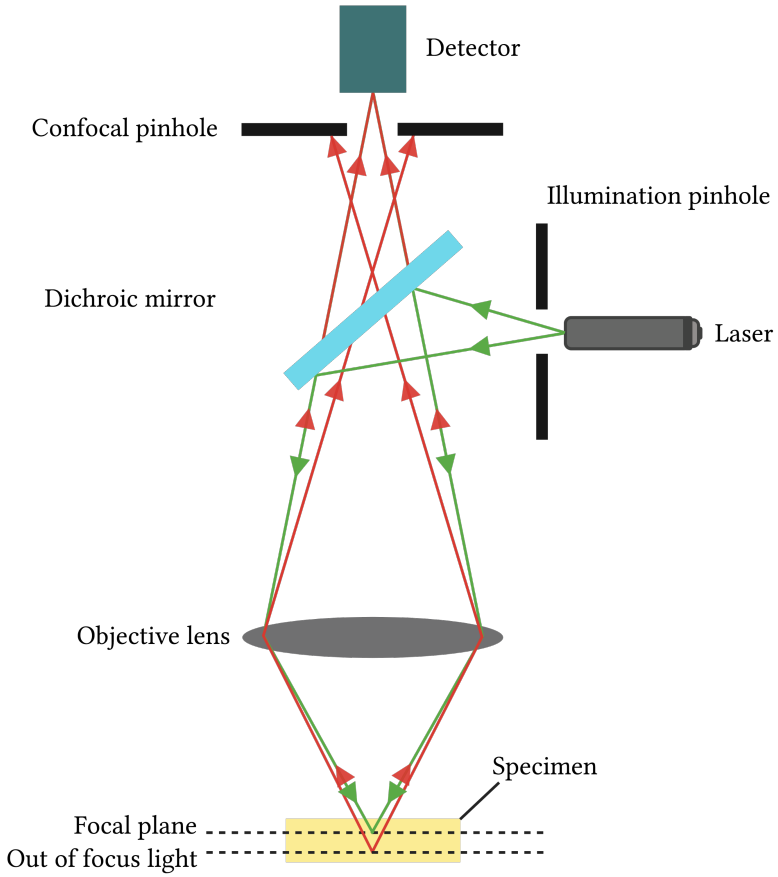

Figure 2.10: Schematic illustration of confocal laser scanning microscopy (CLSM), with a laser source, illumination pinhole, dichroic mirror and confocal pinhole. Light from the focal plane reaches the detector, while out of focus light is blocked by the confocal pinhole.

Chapter 3

Materials[1]

3.1 MicroMarker™

MicroMarker™(VS-11913, Fujifilm VisualSonics) is a gas-filled, non-targeted contrast agent used for small-animal CEUS. The mean MB diameter is 2.3 µm to 2.9 µm, and the bubbles are composed of an outer phospholipid shell encapsulating a gas core of nitrogen and perfluorobutane [66]. The MB solution is reconstituted in 0.9% sodium chloride w/v in water. MicroMarker has a clearance time of 10-20 min after injection.

3.2 Sonovue®

Sonovue ® (Bracco) are MBs with a phospholipid shell filled with sulfur hexafluoride gas, and is the most commonly used contrast agent in clinic. The average diameter is 2.5 µm, thus it is an intravascular contrast agent. Its half-life is around one minute [67]. Sonovue MBs are reconstituted in 0.9% sodium chloride w/v in water. After reconstitution, the concentration of MBs is 8 µL/mL.

3.3 ACT® formulation

The ACT® formulation (EXACT Therapeutics, Oslo, Norway) is composed of a MB and microdroplet dispersion. The MB is Sonazoid™, which is a contrast agent with an average diameter of 2.6 µm. Sonazoid MBs comprise hydrogenated egg phosphateidylser-

[1] Parts of this section overlap with the authors project thesis[12].

ine–sodium phospholipid shell filled with perfluorobutane gas, and are embedded in a lyophilized sucrose matrix [68]. The microdroplets consists of perfluoromethylcyclopentane (PFMCP), and have a diameter of 2-4 µm. According to the protocol, a vial of Sonazoid MBs (8 µL/mL) is mixed with 2 mL of the microdroplets with concentration 4 µL/mL [60], and form microbubble/microdroplet clusters.

3.4 Liposomes

The experiment on uptake and microdistribution of nanoparticles utilized liposomes, kindly provided by Sjoerd Hak (SINTEF Industries). Liposomes are spherical lipid vesicles, consisting of one or more lipid bilayers [69]. To enable imaging of the liposomes, the lipids were labelled with the fluorescent dyes Atto 680 and Atto 633 for Pearl-imaging and and CLSM, respectively. Average diameter of the liposomes is 110 nm. The polydispersity index (PDI) is 0.132, which is a measure of the heterogeneity of a sample based on size. The liposome solution has a lipid concentration of 18 mM.

3.5 Fluorescently Labeled Lectin

Fluorescein isothiocyanate labeled *Lycopersicon esculentum* (Tomato) Lectin (FITC-LEL) (FL-1171-1, Vector Laboratories) is an effective marker of the vasculature in rodents. Lectin binds to polysaccharides attached to glycoproteins on the ECs of the blood vessel wall. FITC has a emission excitation maxima at 498 nm, and emission maxima at 517 nm. Before euthanasia, FITC-LEL was injected in the animals and allowed to circulate for 5 min to mark functional blood vessels.

3.6 Anti-CD31

Staining of all blood vessels in the tumor sections was done by IHC, where the primary antibody used was Purified Rat Anti-mouse CD31 (Anti-CD31) (clone MEC13.3) (550274, BD Biosciences). Anti-CD31 binds to the protein cluster of differentiation (CD31), expressed by the ECs on the blood vessel lining.

3.7 IgG-AF647

The secondary antibody used for IHC staining was Alexa Fluor 647-conjugated Anti-rat AffiniPure donkey-rat IgG (IgG-AF647) (JIM-712-605-153, Dianova). The fluorescent dye AF647 has a excitation maxima og 651 nm, and emission maxima at 667 nm. Such long wavelength dyes has the advantage of low auto-fluorescence in biological specimens.

Chapter 4

Methods[1]

Cell cultures and implantation of cancer cells was performed by Caroline Einen. Animal experiments were performed by Sofie Snipstad, Caroline Einen, Jessica Lage and Veronica Nordlund.

4.1 Cell Cultures

CT26 (CRL-2638, American Type Culture Collection (ATCC)) and 4T1 (CRL-2539, American Type Culture Collection (ATCC)) cancer cells were cultured in RPMI 1640 Medium (30-2001, ATCC) in 10% fetal bovine serum (FBS) (F7524, Sigma Aldrich) supplemented with 1% penicillin streptomycin (P0781, Sigma Aldrich). The KPC cancer cells originate from the Department of Radiation Oncology at the Massachusetts General Hospital, where they were isolated from pancreatic ductal adenocarcinoma (PDAC) tumors in transgenic KPC mice. KPC cells were cultured in Dulbecco's Modified Eagle Medium (DMEM) (Gibco™ 11960-044, Thermo Fisher Scientific) with 10% FBS, 1% penicillin streptomycin and 0.5% L-Glutamine (G7513, Sigma Aldrich). CT26 and 4T1 cells were seeded at a ratio of 1:20-1:30, while the seeding ratio for KPC was 1:10-1:20.

During subculturing, the old cell medium was removed before washing the cells twice with 5 mL Dulbecco's Phosphate Buffered Saline (DPBS) (D8537, Sigma-Aldrich). 1 mL 0.25% Trypsin-EDTA (Gibco™ 25200-072, Thermo Fisher Scientific) was added, followed by incubation at 37°C for 3 minutes to detach the cells. Subsequently, the trypsin was neutralized by adding 9 mL fresh cell medium and the cells were pipetted to ensure a homogeneous cell suspension. A certain volume of cell suspension was transferred to new

[1] Parts of this section overlap with the authors project thesis[12].

75 cm^2 flasks with 14 mL cell medium to obtain an appropriate seeding ratio.

4.2 Implantation of Cancer Cells

Prior to implantation of cancer cells in mice, the cells were washed, trypsinzed and resuspended as described above. The cells were then centrifuged for 5 minutes at 1500 RPM, the supernatant was removed and cell medium was added to the desired cell concentration. Cells were kept on ice until implantation. For CT26 and 4T1, 100 000 and 10 000 cells, respectively, in 50 µL cell medium was injected subcutaneous in the right hind leg of a BALB/c mouse. For KPC, 200 000 cells in 20 µL cell medium was injected subcutaneous in the right hind leg of a B6/albino mouse. Around 14 days post cell implantation, the tumors were large enough for animal experiments. All animal experiments were approved by the Norwegian Food and Safety Authority.

4.3 CEUS

A general description of CEUS imaging and analysis is given in the following subsections, whereas it is indicated in the description of each of the USMB animal experiments which tumors that were CEUS imaged. CEUS was performed to characterize the perfusion of different tumor models in vivo, to compare CLSM and CEUS as methods for perfusion measurement, and to explore the potential of CEUS as a stratification tool for USMB treatment.

4.3.1 CEUS Imaging

The contrast agent used for CEUS imaging, MicroMarker™, was reconstituted according to the preparation protocol. The animal was anesthetized using isofluorane gas, followed by placement of a tail-vein catheter for injection of MicroMarker™MBs. To improve contact between the gel and tumor, the fur was removed from the animal leg using hair removal cream.

Vevo 3100 LAZR-X Ultrasound Imager was used together with the MX250 probe. A frame rate of 1 frames per second was used. Centrifuged US gel was used to ensure acoustic contact between the probe and animal. Pre- and post injection of MicroMarker, a 3D scan of the tumor was performed. However, these data were not analyzed in this thesis.

The probe was placed on the tumor center where the diameter is the largest. Injection of MBs and recording was started simultaneously. Through the tail-vein catheter, 50 µL MicroMarker was injected over 5 s. Recording proceeded for 6 min, which resulted in a total of approximately 360 frames.

4.3.2 CEUS Analysis

Analysis of the CEUS 2D bolus videos was performed with the software VevoCQ (FUJIFILM VisualSonics, Toronto, Canada). If necessary, the "motion correction" tool was used to correct for tumor displacement during imaging. For each tumor, three ROIs were drawn manually with the ROI function - the whole tumor, center and periphery. As VevoCQ does not provide a measuring tool, the periphery ROI had to be selected by using an approximate 10% margin of the maximum tumor diameter. An example is shown in Figure 4.1. Raw data and perfusion parameters for each ROI were acquired with the "quantify" tool. The raw data was exported to a .csv-file, and Matlab was used to plot the data for each ROI.

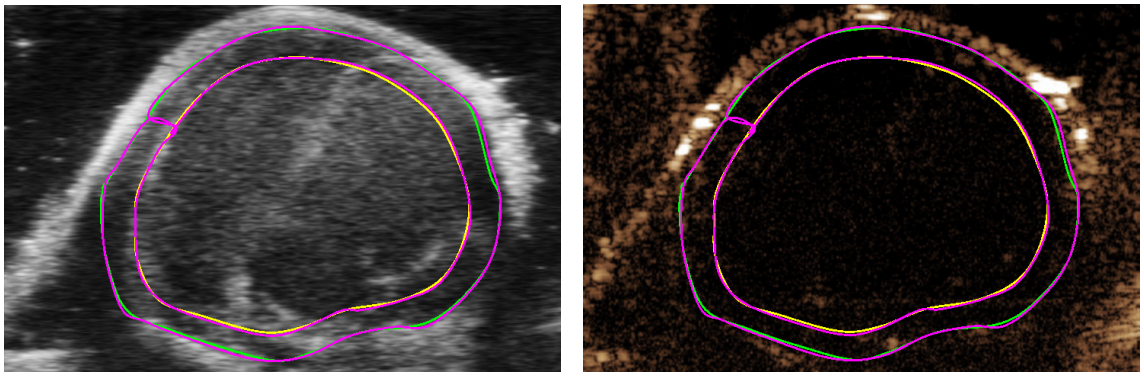

(a) (b)

Figure 4.1: Example of ROIs for a CT26 tumor from a CEUS bolus video. The total tumor is green, the center yellow and the periphery pink. B-mode is shown in a) and non-linear contrast mode in b).

4.4 Effect of USMB on Fraction of Functional Tumor Blood Vessels

4.4.1 US and Sonovue Treatment of CT26 and 4T1 Animals

Experimental groups for the perfusion study was one control and one treated group. For CT26 animals, the control group consisted of 7 animals, while the treated group had 8 animals. For 4T1 animals, both groups consisted of 6 animals. Prior to USMB treatment, the 13 CT26 animals that had large enough tumors, were CEUS imaged according to section 4.3.1. This animal experiment is continuation of the author's specialization project carried out in 2022, where 4 control and 3 treated CT26 tumors were analyzed. Remaining CT26 tumors and all 4T1 tumors are included in this thesis.

To effectively transmit the US from the transducer to the tumor, a water tank was filled and the water heated to 34 °C. A 1 MHz Imasonic Transducer was placed in the water tank. A signal generator (33500 B, Keysight Technologies) and 50dB power amplifier (2100 L, Electronics and Innovations Ltd) generated the US. Using a 4 s burst period, 10000 cycles and 185 mVpp, giving a MI of 0.5 and 80 Vpp to the transducer. The input voltage to the transducer was controlled using the Wavesurfer 44Xs Oscilloscope with a 1:10 probe. The USMB setup is shown in Figure 4.2.

SonoVue® MBs were reconstituted according to the preparation protocol. The animal was prepared for USMB treatment. During the treatment process, the animal was anesthetized using isofluorane (2.5%, 1 $Lmin^{-1}$ medical air). A tail-vein catheter was placed for injection of Sonovue and FITC-LEL.

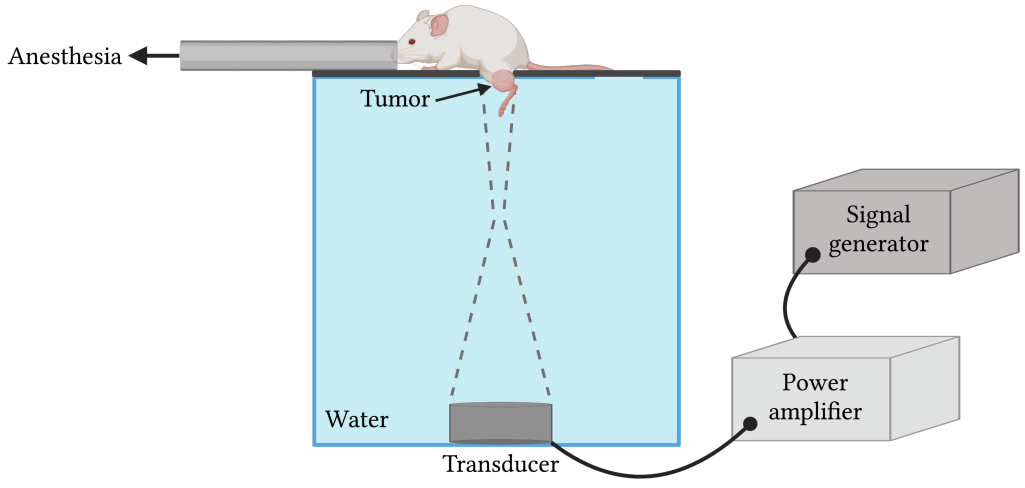

Figure 4.2: Illustration of the experimental setup for the USMB treatment. Figure created with BioRender.com.

The animal was moved to the US treatment rig, and the leg and tumor were placed in the water tank. The group of treated animals were sonicated for 9 min. A 50 µL Sonovue injection was given, and the US was turned on. Injection of 50 µL Sonovue was repeated after 3 min and 6 min. The control group received a 50 µL Sonovue injection every 3 minutes for 9 minutes, without sonication. Directly after treatment, 50 µL FITC-LEL (2 $\mathrm{mgmL^{-1}}$) was injected through the tail-vein catheter, in order to label functional blood vessels. The FITC-LEL circulated for 5 min, before the animal was euthanized by cervical dislocation. The timeline in Figure 4.3 shows the workflow of the USMB treatment.

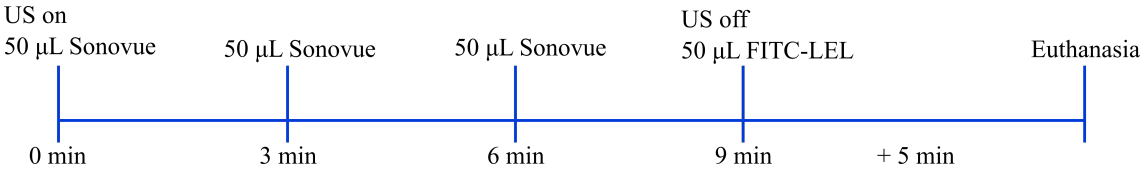

Figure 4.3: Timeline for the USMB treatment. US was not turned on for control animals.

4.4.2 US and ACT Treatment of CT26 Animals

Experimental groups for the ACT experiment were 5 control animals and 6 treated animals. The setup for ACT treatment was identical to that of the USMB treatment, as described in section 4.4.1. and shown in Figure 4.2.

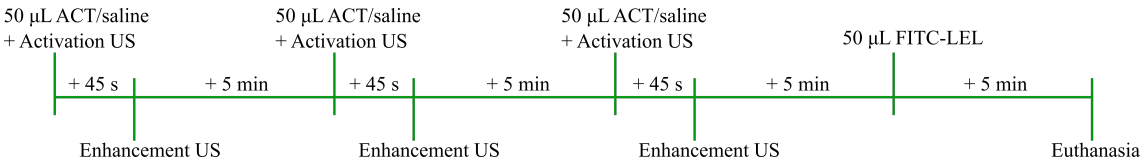

Figure 4.4: Timeline for the ACT treatment. The leg of control animals was not placed in the water tank and were thus not insonated.

Prior to treatment, the hair was removed from the leg of the animal. The animal was anesthetized using isofluorane (2.5%, 1 $\mathrm{Lmin^{-1}}$ medical air) during placement of the tail vein catheter and during treatment. The ACT clusters were prepared according to the protocol. When placed on the US setup, the leg of treated animals was placed into the water tank, while the control animals' leg was not. Controls were injected with 50 µL saline, and treated animals with 50 µL ACT formulation. Subsequently, US was turned on. The duration of the ACT activation was 45 s, using US settings of 2.7 MHz, 8 cycles, a PRF of 1 kHz, giving a MI of 0.2. Post activation, the enhancement proceeded for 5 min. The US settings during enhancement were 0.5 MHz, 2 cycles, PRF 1 kHz and MI 0.2. Injection of ACT/saline, activation US and enhancement US was repeated in total three times per

animal. Directly after treatment, 50 µL FITC-lectin (2 µg/mL) was injected. After 5 min, the animal was euthanized.

4.4.3 Tumor Sectioning

Tumors were removed from the animal leg immediately after euthanasia. Accordingly, the tumor was weighted and measured, before it was mounted on a cork plate and frozen in liquid nitrogen. The tumors were kept at −80 °C until sectioning. When mounted on the cork plate, the tumour was orientated such that the part orientated towards where the animal leg pointed was placed towards the frosted end of the cork plate. The same applies for the orientation of the section on the glass slide, where the side towards the leg of the animal corresponds to the frosted end.

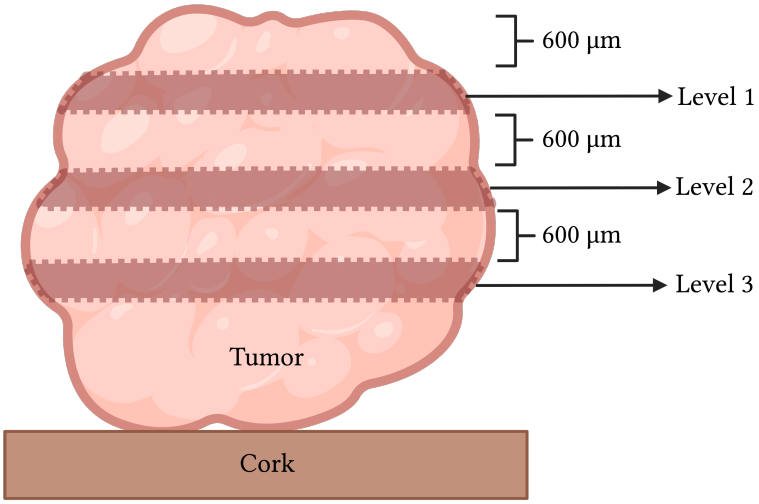

Figure 4.5: Illustration of how tumors involved in the USMB and perfusion experiments were sectioned. Three levels were sectioned. From the top of the tumor and in between sections, 600 µm were removed. Figure created with BioRender.com.

The cryostat sectioning was performed by the Cellular and Molecular Imaging Core Facility (CMIC). For each tumor, three levels in different regions of the tumor were sectioned. From the top of the tumor to the first level, 600 µm were removed. Similarly, between the first and second level, and between the second and third level, 600 µm were removed. From the USMB experiment with Sonovue, 10 CT26 and 5 4T1 sections with a thickness of 8 µm were obtained from each of the three levels. From the ACT experiment, 10 CT26 sections were obtained from each level. The sections were stored at −80 °C.

Additionally, one section from each of the three levels was stained with hematoxylin, erythrosine and saffron (HES). HES-staining enables imaging of cell nuclei (blue), cytoplasm (red), muscle and elastic fibers (pink), and collagen (orange), of which the two former are of interest in order to distinguish between tumor tissue, muscle tissue and edema.

4.4.4 Immunohistochemical Staining of Blood Vessels

Immunohistochemical (IHC) staining of blood vessels was performed to enable imaging of all tumor blood vessels by CLSM, in order to study the effect of Sonovue and ACT bubbles and US on perfusion. For this purpose, sections from the second tumor level were selected. All of the tumor blood vessels, also the functional ones, were stained with Anti-CD31 as primary antibody, and IgG-AF647 as secondary antibody. Two to four sections were stained per lab day.

Initially, the sections were defrosted for 5 min in room temperature. Further, sections were washed in PBS (Sigma-Aldrich, MO, USA) for 5 min, before fixation of tissue in acetone (Sigma Aldrich, MO, USA) for 5 min. Again, sections were washed with PBS for 5 min. To ensure the liquid to stay in place when applied, the tumor tissue was marked with a Pap Pen, which has hydrophobic properties. Next, blocking of unspecific binding of antibodies was done by incubating the section in 100 µL of 12 % BSA (Sigma-Aldrich, MO, USA) + PBS blocking solution, applied with a pipette, for 50 min, before it was washed with PBS for 10 min. The primary antibody solution was prepared according to Table 4.1, where the presented quantities are enough for two sections. Anti-CD31 was diluted 1 : 50 with 12% BSA + PBS. This results in a final concentrations of 0.01mg/mL of Anti-CD31. After incubation, sections were washed with PBS for 3x5 min. The secondary antibody solution was prepared according to Table 4.1. IgG-AF647 was diluted 1 : 50 with 12% BSA + PBS, giving a concentration of 0.03mg/mL. Each section was incubated with 100 µL of the antibody solution for 1 h in room temperature in a light proof box lined with aluminum foil, to avoid loss of signal fading. Subsequently, the sections were washed with PBS for 3x5 min. To mount the sections, 8-12 µL of the mounting medium VectaShield Vibrance (REF H-1800, Vector Laboratories, CA, USA) was applied, followed by application of the cover glass. VectaShield Vibrance ensures proper mounting of the section, and reduces loss of fluorescence. The mounted sections with VectaShield were allowed to set for 1 hour at 4 °C.

Table 4.1: Preparation of primary and secondary antibody solutions for IHC staining of blood vessels. Quantities for staining of two sections. Both antibodies were diluted 1 : 50.

Primary antibody solution		**Secondary antibody solution**	
Anti-CD31	4 µL	IgG-AF647	4 µL
12% BSA+PBS	196 µL	12% BSA+PBS	196 µL

Additionally, some sections were only stained with the secondary antibody, IgG-AF647. The purpose of these control sections was to detect unspecific binding of the secondary antibody in the tumor sections. Except for skipping the primary antibody step, the protocol used was the same as previously described.

4.4.5 CLSM of Blood Vessels and HES-stained sections

A confocal laser scanning microscope (LS 800 Airyscan Confocal Microscope, Carl Zeiss AG, Germany) was used to image the tumor blood vessels in the IHC stained sections. Imaging was performed within the same day as or the morning after IHC, to avoid fading of the fluorescent signal.

The detector was a gallium arsenide phosphide PMT (GaAsP PMT). Acquisition settings and microscope configurations were set in the Zeiss ZEN Blue software (Carl Zeiss AG, Germany).

For imaging of sections from the Sonovue experiment, a plan apochromat air objecive with $20x$ magnification and numerical aperture 0.8 was used. The laser wavelengths were 640 nm for AF647 and 488 nm for FITC-LEL. Emission filters of 656−700 nm and 410−560 nm were applied, respectively. A filter blocks the particular wavelength of the laser from being detected. The laser intensity for the 640 nm laser was 0.14%, and 0.75% for the 488 nm laser. The detector gain for AF647 was set to 705 V , and 650 V for FITC-LEL, both with an offset of 0. Finally, the pinhole diameter was set to 1AU. Acquisition parameters for AF647 and FITC-LEL are presented in Table 4.2.

Table 4.2: Acquisition settings for CLSM imaging of blood vessels for Sonovue treated CT26 and 4T1 tumors.

Fluorophore	**FITC-LEL**	**AF647**
Laser wavelength	488 nm	640 nm
Excitation wavelength	498 nm	651 nm
Emission wavelength	400-560 nm	650-700 nm
Pinhole diameter	1 AU	1 AU
Laser intensity	0.75	0.14
Detector gain	650 V	705 V
Detector offset	0	0

For imaging of sections from the ACT experiment, A plan neofluar air objecive with $20x$ magnification and numerical aperture 0.5 was used. The laser wavelengths were 640 nm for AF647 and 488 nm for FITC-LEL. The laser intensity for the 640 nm laser was 0.2%, and 0.75% for the 488 nm laser. The detector gain for AF647 was set to 730 V , and 675 V for FITC-LEL, both with an offset of 0. Acquisition parameters for AF647 and FITC-LEL are presented in Table 4.3.

Tile scans of tumor sections were acquired in order to visualize the entire cross section. Tile scans were acquired using a scan speed of 8, zoom factor 0.6, and line averaging 2. Depending on the tumor size, between 200 and 500 tiles were used, and 25-64 focus points were manually adjusted. The tile overlap was set to 20%. A parabolic saddle function was chosen to interpolate between the focus points. Single images of selected areas of interest were acquired using a scan speed of 5 and zoom factor 1. The control sections, only stained with IgG-AF647, were imaged with the 640 nm laser to reveal the amount of unspecific binding of IgG-AF647 and autofluorescence.

Table 4.3: Acquisition settings for CLSM imaging of blood vessels for ACT treated CT26 tumors.

Fluorophore	**FITC-LEL**	**AF647**
Laser wavelength	488 nm	640 nm
Excitation wavelength	498 nm	651 nm
Emission wavelength	400-560 nm	650-700 nm
Pinhole diameter	1 AU	1 AU
Laser intensity	0.75	0.2
Detector gain	675 V	730 V
Detector offset	0	0

For both Sonovue treated and ACT treated tumors, tile scans of the HES-stained sections were acquired using the ZEN Blue software and the Zeiss LSM 800 microscope in brightfield mode. Sections from the second tumor level were imaged. For the USMB sections, plan apochromat 20x 0.8 NA objective and lamp intensity 11 V was used, while the ACT sections were imaged using a plan apochromat 10x 0.45 NA water objective and lamp intensity 6.5V. The 20x objective was changed to the 10x objective since it provided faster acquisition of tile scans and yet sufficient resolution. Here, 16 to 25 focus points were manually adjusted, depending on the tumor size. Post imaging, brightness and contrast was adjusted to display the different tissue types properly.

4.4.6 Processing and Analysis of Blood Vessel Images

To quantify the amount of functional and all blood vessels, the CLSM tile scans were processed and analyzed in the software Fiji (Fiji Is Just ImageJ, version 2.9.0/1.53t). The tile scans were saved as .czi-files in the ZEN software, and opened in the largest format in ImageJ.

Initially, the blood vessel tile scan was compared to the tile scan of the corresponding HES-stained section to be able to exclude muscle tissue, edema and air bubbles from further analysis. These regions are not relevant to quantify the amount of blood vessels, as only tumor tissue is of interest. This step was done in composite gray mode, and thus applied to both channels. Brightness and contrast was temporarily adjusted to better reveal the tumor boundaries. The areas to be removed were selected using the "polygon selection" tool and deleted with the "clear" tool.

The AF647-channel (red channel) and the FITC-LEL-channel (green channel) were split, and then duplicated. Each channel was processed separately, as the signal intensity, background noise and autofluorescence varied. All steps of the image processing are demonstrated on a 20x magnified single image in Figure 4.6. The red channel was processed first, and used as a mask for the green channel. Based on the amount of signal in the autofluorescence control sections, subtraction and filtering was performed to remove background noise. Pixels with gray values below 10 were subtracted using the "subtract" tool. The value 10 was decided to be appropriate to remove background noise. A median filter of 2 pixels was applied to the image. Gray morphology with a closing diamond structure of radius 3 pixels was used to remove dark spots in bright areas. This compensated for the disruption of blood vessels created by the median filter. Then, a duplicate of the red channel was created and used for comparison when choosing the thresholding algorithm. Several thresholding algorithms were tested to make the image binary, and the Li algorithm

appeared most suitable. However, the minimum threshold value had to be set manually as the automatically set value was not satisfactory. The minimum value for the thresholding was set to between 18-22, as the signal intensity varied. Accordingly, this threshold was applied to the red channel. The processed and thresholded red channel was then converted to a mask. The "image calculator" was used to subtract the mask from the green channel, resulting in an image containing green pixels not colocalized with red pixels. Then, this resulting image was subtracted from the original green channel. In this way, it was ensured that only green pixels overlapping with red pixels were remaining. This subtracted green channel image was processed using the same method as for the red channel. Pixels with gray values below 5 were subtracted using the "subtract" tool, and a median filter of 2 pixels was applied. The Li thresholding was applied, and here, the minimum value for the thresholding was between 8 and 14.

For tumors included in the ACT experiment, the threshold values used were different due to other microscope settings and to improve the processing procedure. Otherwise, the image processing was done similarly as for the tumors treated with Sonovue. Background noise was removed by subtracting intensity values of 10 and 7 for the red and green channel, respectively, and the threshold values applied were 10 and 5.

Next, the tumor was divided into three different regions of interest (ROIs) - the entire tumor (total), the center and the periphery. The following procedure is adapted from the recipe from Årseth's master thesis [70] on how to divide CLSM tile scan images into tumor regions in Fiji. These regions were selected using the "polygon selection" tool. Initially, the entire tumor was outlined. It was then added and saved to the ROI manager (Edit - Selection - Add to Manager). To create the center region, the total tumor ROI was shrunk (Edit - Selection - Enlarge) with 10% of the maximum tumor diameter, and saved to the ROI manager. Lastly, the periphery ROI was created by selecting both the entire tumor and center ROI in the ROI manager, and then selecting the XOR option appearing when right clicking. The ROI was saved to the ROI manager. Figure 4.7 presents an example of processed and thresholded images, as well as the ROIs are presented. To quantify the amount of blood vessels in the red and green channel, the area fraction was calculated for each of the tumor ROIs. This counts all pixels corresponding to 1 in the binary image, and outputs the fraction of counted pixels in the area of the ROI. "Area fraction" measurement was selected (Analyze - Set measurements). In the ROI manager, the area fraction was measured for each ROI using the "Measure" tool. The total amount of blood vessels was found by measuring the area fraction in the red channel, and the amount of functional blood vessels by measuring the area fraction in the green channel. This procedure was repeated for each ROI and for both channels.

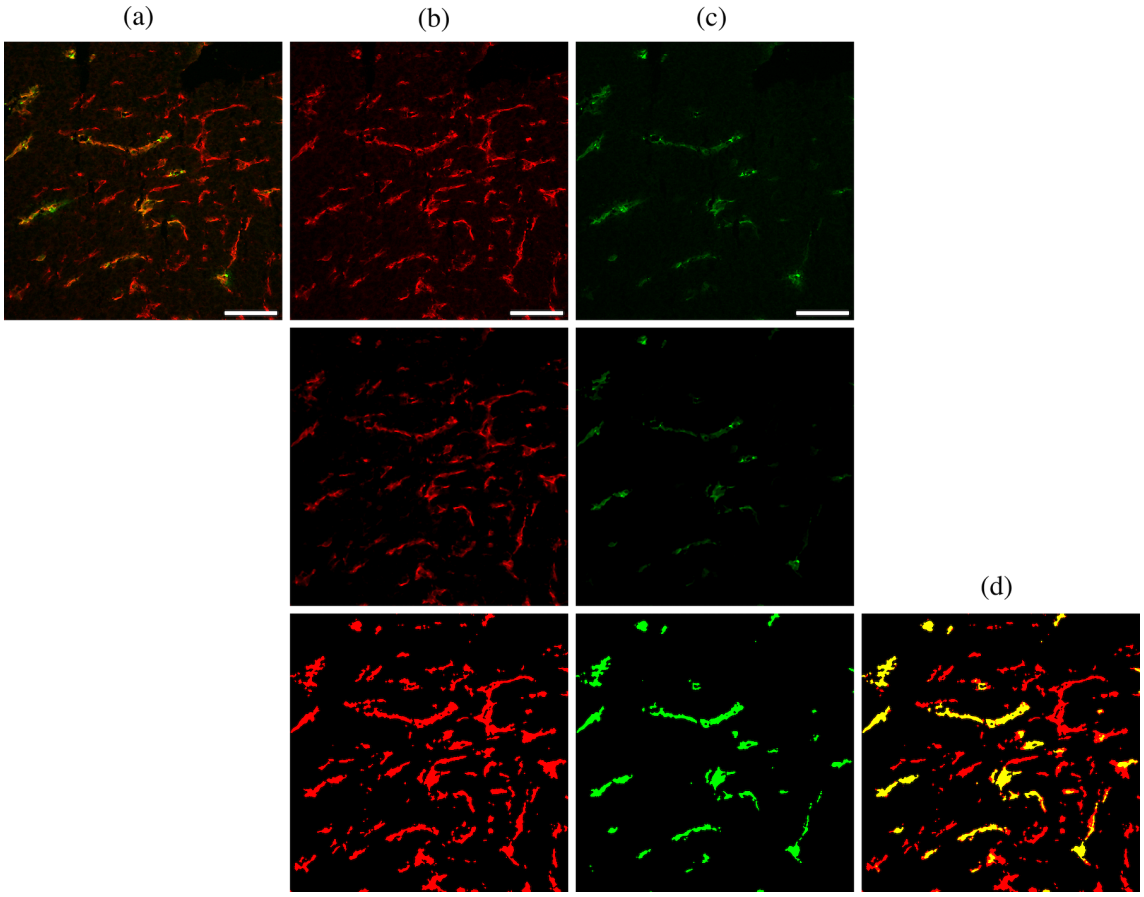

Figure 4.6: Steps of the image processing for the perfusion analysis demonstrated on a single image. (a) shows the unprocessed composite image of the red and green channel. (b) and (c) shows the processing of the red and green channel, respectively. The first row shows the unprocessed images, while the second row of (b) and (c) shows the images after subtraction, filtering, and application of gray morphology. The green channel was also masked. The third row shows the thresholded images, where (d) is the composite of the thresholded green and red channel. Scale bars are 100 µm and applies to all images.

Sectioning of ACT-treated CT26 tumors was challenging due to the soft consistency of the tumor tissue. In some tumors the tissue was displaced. For two tumors, parts of the disrupted tissue regions needed to be excluded from the image analysis. The area of preserved tumor tissue still provided sufficient data.

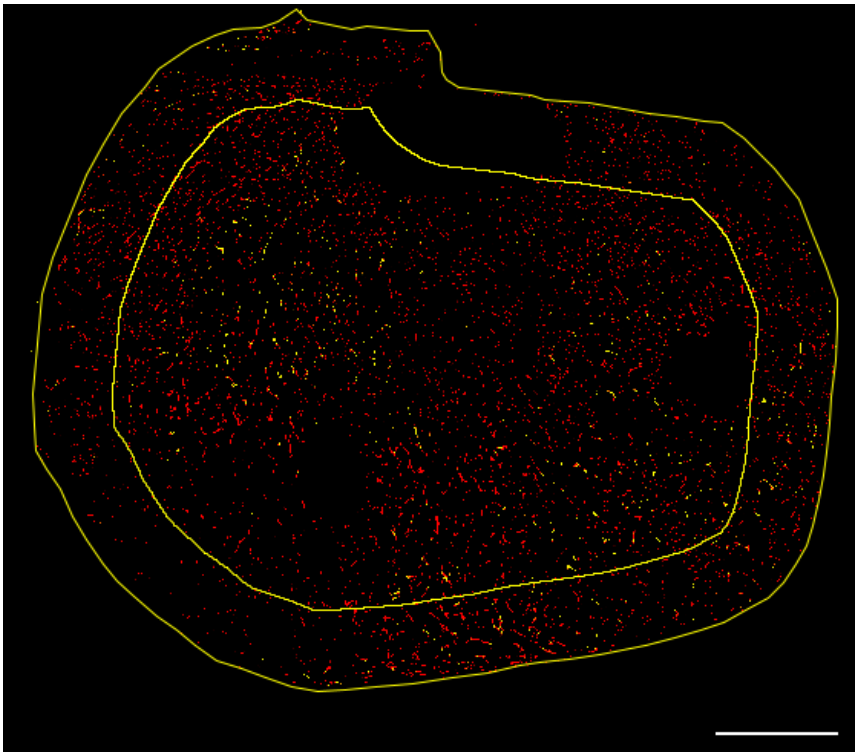

Figure 4.7: Example of processed and thresholded tilescan, and the total, center and periphery ROIs. Composite of the red and green channel, where red pixels are AF647, showing all blood vessels. Green or yellow pixels are FITC-LEL, hence functional blood vessels. Scale bar is 1000 µm.

4.5 Effect of USMB on Uptake and Microdistribution of Liposomes

4.5.1 Animal Experiment

The effect of USMB on uptake and microdistribution of liposomes was evaluated in animals with CT26, 4T1 and KPC tumors. The experiment used 14 animals with each tumor type, and the experimental groups were 7 control and 7 USMB treated. The day before USMB treatment, all animals were CEUS imaged according to section 4.3.1, in order to characterize the tumor models, and to correlate NP uptake and CEUS to explore the potential of CEUS for patient stratification.

Throughout the animal experiment, the uptake of liposomes was followed using the Pearl® Impulse Small Animal Imaging System (LI-COR Biosciences, Lincoln, NE, USA), referred to as Pearl. Pearl is an imaging system enabling imaging of entire animals. The liposomes labelled with Atto680 (exitation 680 nm, emission 695 nm) were imaged using the 700-

channel on the Pearl scanner.

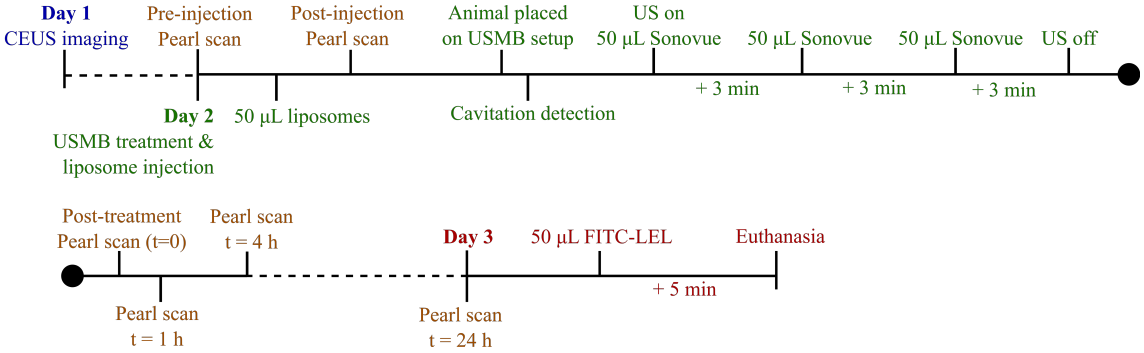

Figure 4.8: Timeline for the liposome and USMB experiment. US was not turned on for control animals.

The experiment lasted for three days. Tumors were CEUS imaged on the first day. On the second day, the USMB treatment and liposome injection was performed, and the animals were imaged with Pearl. Prior to treatment, the animal was anesthetized and the tail vein catheter was placed, before it was imaged in the Pearl scanner to assess the background. Then, 50 µL liposomes was injected, directly followed by a Pearl scan. Next, the animal was moved to the US rig, and the leg placed in the water tank. Initially, a cavitation detection was performed with the intention to verify cavitation from Sonovue microbubbles. For this, a 5 MHz transducer (V307-SU, Olympus) was placed in a container in the water tank and connected to the Wavesurfer 44Xs oscilloscope. A Matlab script was used to read the signal from the oscillocope to a computer. Cavitation detection was run until the signal from the transducer stabilized at -130 to -140 dB. USMB treatment was then performed in the same manner as described in section 4.4.1, yielding the same setup, US settings and workflow. Animals in the treated group received liposome injection, followed by USMB treatment with Sonovue MBs. Similarly, the control group received liposomes and Sonovue, but without US. To follow the uptake of liposomes, the Pearl® scanner was used to image the entire animal and visualize the fluorescently labelled liposomes immediately after (t = 0), 1 hour and 4 hours after USMB treatment. On the third day, animals were once again Pearl scanned 24 h post treatment. Perfused tumor blood vessels were stained by injecting 50 µL FITC-LEL (2 µg/mL), allowing it to circulate for 5 min before euthanazing the animal by cervical dislocation. Tumor, heart, lung, liver, spleen and kidneys were resected from the animal and imaged with the Pearl scanner.

4.5.2 Tumor Sectioning

After resection of tumors from the animal leg, tumors were weighted and measured, mounted on a cork plate (O.C.T. Tissue Tek) and then frozen in liquid nitrogen. The tumors were kept at −80 °C until sectioning. When mounted on the cork plate, the tumour was orientated such that the part orientated towards where the animal leg pointed was placed towards the frosted end of the cork plate. The same applies for the orientation of the section on the glass slide, where the side towards the leg of the animal corresponds to the frosted end.

Cryostat sectioning was performed by the Cellular and Molecular Imaging Core Facility (CMIC). For each tumor, three levels of the tumor were sectioned, with specifications for each tumor type. From the top of the tumor to the first level, 1.5 mm, 1 mm and 0.5 mm was removed for CT26, 4T1 and KPC tumors, respectively. Similarly, between the first and second level, and between the second and third level, the same length was removed. In each level, 11 sections of 8 µm were acquired. The sections were stored at −80 °C. The first section from each of the three levels was stained with HES-stained.

4.5.3 Analysis of Pearl Data

Analysis of Pearl dataimages was performed by Caroline Einen. The analysis was done in ImageJ, where a ROI was drawn around the tumor, and the mean and total intensity was measured for the different time points - 0h, 1h, 4h and 24h post treatment, and ex vivo. The measured fluorescence reflects the tumor uptake of NPs.

4.5.4 CLSM of NPs and Blood Vessels

CT26 tumors were CLSM imaged to assess the extravasation distance (ED) of the NPs, i.e. how far the NPs have extravasated from the closest blood vessel. Section 2.7 was chosen for CLSM imaging and analysis, i.e. the seventh section from the second tumor level. Prior to imaging, the sections were mounted with Vectashield Vibrance® with DAPI (REF H-1800, Vector Laboratories, CA, USA) and a cover glass, and allowed to set at 4 °C for 1 h. CLSM of liposomes and blood vessels was performed using the LSM 800 Confocal Airyscan Microscope (Carl Zeiss AG, Germany). A Plan Neofluar 20x 0.5NA air objective was used. The detector was a gallium arsenide phosphide PMT (GaAsP PMT). Acquisition settings and microscope configurations were adjusted in the Zeiss ZEN Blue software (Carl Zeiss AG, Germany). Images were acquired using scan speed 5 and line averaging 2.

Table 4.4: Acquisition settings for CLSM imaging of liposomes (ATTO633), blood vessels (FITC-LEL) and cell nuclei (DAPI).

Fluorophore	**FITC-LEL**	**ATTO633**	**DAPI**
Laser wavelength	488 nm	640 nm	405 nm
Excitation wavelength	498 nm	633 nm	359 nm
Emission wavelength	400-560 nm	650-700 nm	410-546 nm
Pinhole diameter	1 AU	1 AU	1.41 AU
Laser intensity	1.2	0.4	1.0
Detector gain	675 V	570 V	740 V
Detector offset	−15	−50	0

Microscope settings are presented in Table 4.4. Functional blood vessels labelled with FITC-LEL were imaged using a laser with wavelength 488 nm and intensity 1.2%. The pinhole diameter was set to 1 AU, the detector gain to 650V and detector offset to -15V. Liposomes labelled with ATTO633 were imaged using a 640 nm laser with intensity 0.4%. The pinhole diameter was 1 AU, detector gain 570V and detector offset -50V due to a strong background signal. As ZEN did not provide as a fluorophore/chrome ATTO633, ATTO635 was used instead. Cell nuclei labelled with DAPI were imaged to better be able to distinguish between tumor tissue and muscle and connective tissue. The DAPI channel was imaged with a 405 nm laser, at intensity 1.0%. The pinhole diameter was set to 1.41 AU, detector gain 740 V, and detector offset 0.

Minimum eight images were acquired for each section - four in the center and four in the 10% periphery of the tumor. Tumor edges where marked using "Positions" under the tile setup in Zen Blue. In this manner, one could search for blood vessels and LPs while following the location in the specimen from "Tiles Advanced Setup". The maximum diameter of the tumor was measured in order to find the 10% periphery. Control sections without liposomes labelled with Atto633 were imaged in order to ensure that the observed fluorescence actually were liposomes.

4.5.5 NP Extravasation Distance

Processing of the liposome and blood vessel images was performed in Fiji (Fiji Is Just ImageJ, version 2.9.0/1.53t). Based on the processed images, the extravasation distance (ED), i.e. the distance from the liposomes to the closest blood vessel, was then measured utilizing a custom made Matlab script. The script was kindly provided by Astrid Bjørkøy, and is attached in Appendix D.

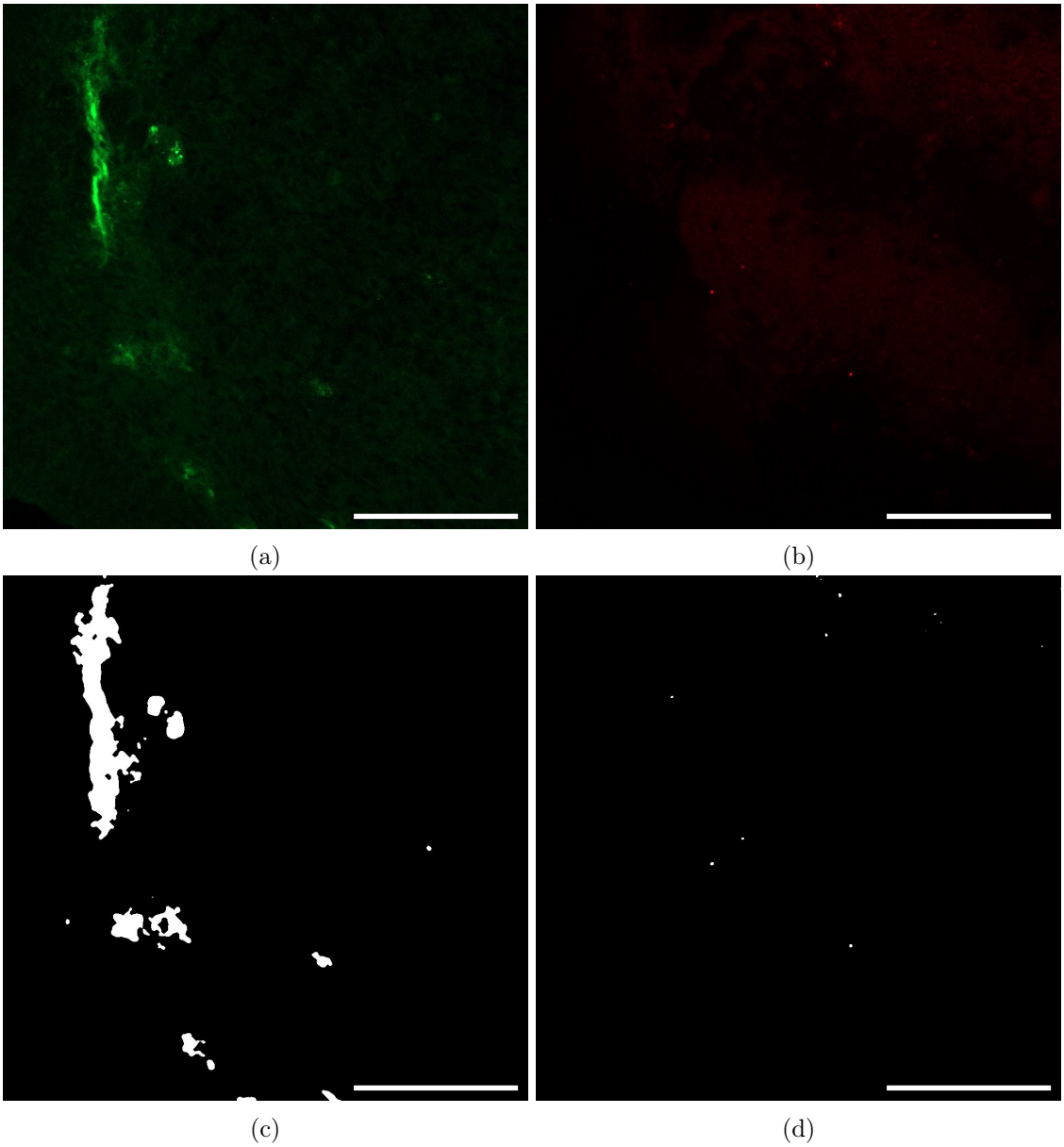

Figure 4.9: Processing of CLSM images of NPs and BVs. Unprocessed images of blood vessels and NPs are shown in (a) and (b), while the processed images of the respective channels are shown in (b) and (c). Scale bars are 100 µm.

Images were saved as czi-files were opened in ImageJ, where the three channels were split. The red channel (ATTO633/liposomes) and green channel (FITC/blood vessels) were processed separately, while the blue channel (DAPI) was used to distinguish tumor tissue from muscle tissue. For the red channel, containing liposomes, a constant of value 20 was subtracted from each pixel using "Process-Math-Subtract" to remove autofluorescence. A Gaussian blur filter with sigma = 0.5 was applied. Then, the image was made binary by thresholding using the RenyiEntropy algorithm. Noise assumed to not be particles was

removed using "Process - Noise - Remove Outliers" with radius below 1px. For the green channel containing blood vessels, values below 5 were subtracted. A Gaussian blur filter with sigma = 2 was applied, and blood vessels were made more continous by Gray Morphology with a closing diamond structure of radius 3. To transform the the image into binary, thresholding was applied using the Triangle algorithm. Finally, noise was removed by applying "Processing - Noise - Remove" Outliers below 5 px. The image processing of both channels is presented in Figure 4.9. Macro scripts for processing of both channels are attached in Appendix C. Scripts were run separately for each image, to control correct classification of blood vessels and NPs. For some images, the scripts had to be adjusted, mainly by changing the background subtraction due to varying background signal.

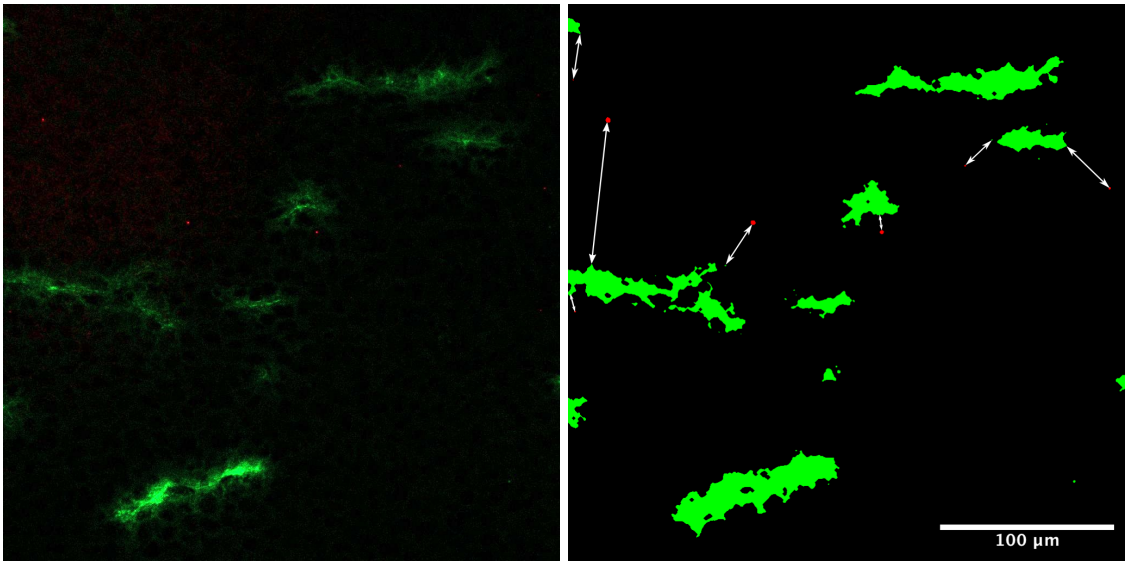

(a) (b)

Figure 4.10: Illustration of how the NP extravasation distance was calculated. An unprocessed composite image of green blood vessels and red NPs is presented in (a). In (b), a composite of the processed and thresholded binary images are shown. The arrows indicate how the Matlab script would calculate the distance between NP lumps and the nearest blood vessels. Scale bar is 100 µm.

NP ED was assessed using a Matlab script calculating the distance between the border of each lump of NPs and the border of the closest blood vessel. Figure 4.10 illustrates how the calculation is performed. One NP lump may contain many NPs, the script does not calculate distance between each pixel containing NPs. The script was provided by Astrid Bjørkøy, and is attached in Appendix D. The script required binary images of the BV and NP channel, generated by the former described image processing. The code also calculated colocalized, i.e. NPs overlapping with blood vessels, and non-colocalized particles, i.e. extravasated NPs. Results were saved to text files and exported to excel for

further analysis. Only extravasated particles were included in the extravasation distance analysis.

To create microdistibution plots, the data were organized by binning in Excel. Colocalized, e.g. extravasated NPs were excluded from further analysis, as only extravasated NPs were of interest. The area (μm^2) of each NP lump is connected to a certain extravasation distance. The extravasation distances were divided into bins of 10 µm. This was done for all images and all animals in each group and tumor region (total, core, periphery). To enable comparison of the different groups, the NP lump area in each bin was converted to percentage of the total area of all NP lumps.

4.6 Statistical Analysis and Plotting

Statistical analysis and plotting of the obtained results was performed in Prism (Version 9.5.0 (525), GraphPad Software, LLC). To compare whether the control and treated animal groups were significantly different, unpaired t-tests were performed. This test requires normal distribution, which was tested using a Shapiro-Wilk normality test. In order to compare more than two groups, e.g. CT26, 4T1 and KPC, a one-way ANOVA test was given normal distribution. If the data did not pass the normality test, a Kruskal-Wallis test was performed.

Correlation between different parameters was also investigated. The variables R^2 of the linear regression line, and the correlation significance level of the correlation, p were obtained, and an α-value of 0.5 was used. If $p \leq 0.05$, the correlation was considered significant. Pearson's correlation coefficient, r, was calculated. The correlation was negligible if $0 \leq |r| \leq 0.1$, weak if $0.1 \leq |r| \leq 0.3$, medium if $0.3 \leq |r| \leq 0.5$ and strong if $0.5 \leq |r| \leq 1$. Depending on the sign of p, the correlation was determined to be either positive or negative.

Chapter 5

Results

5.1 CEUS

5.1.1 CEUS Curves

Plots of the CEUS perfusion data were generated in Matlab, displaying the linearized signal from the MBs along with the curve fit generated by the VevoCQ bolus function. Examples CEUS curves and fit for two tumors are presented in Figure 5.1, including the quality of fit (QOF). The plots show a rapid inflow of the contrast agent, followed by a slow exponential wash-out.

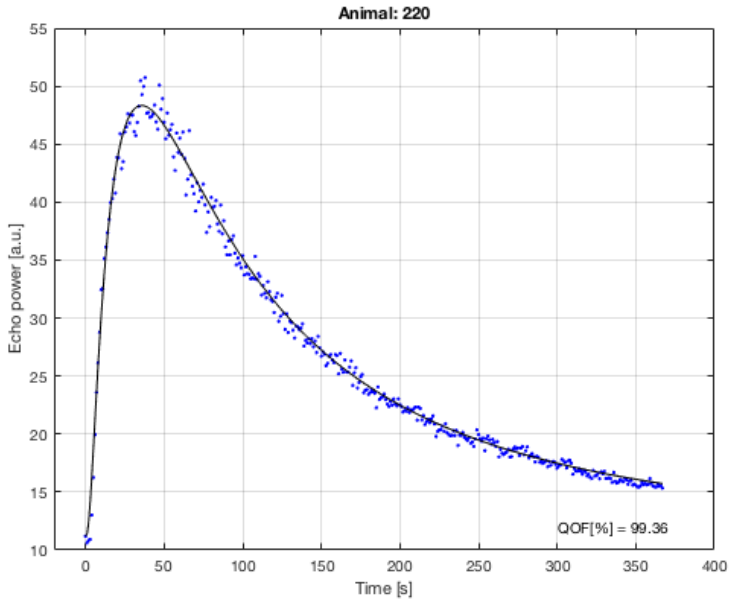

(a)

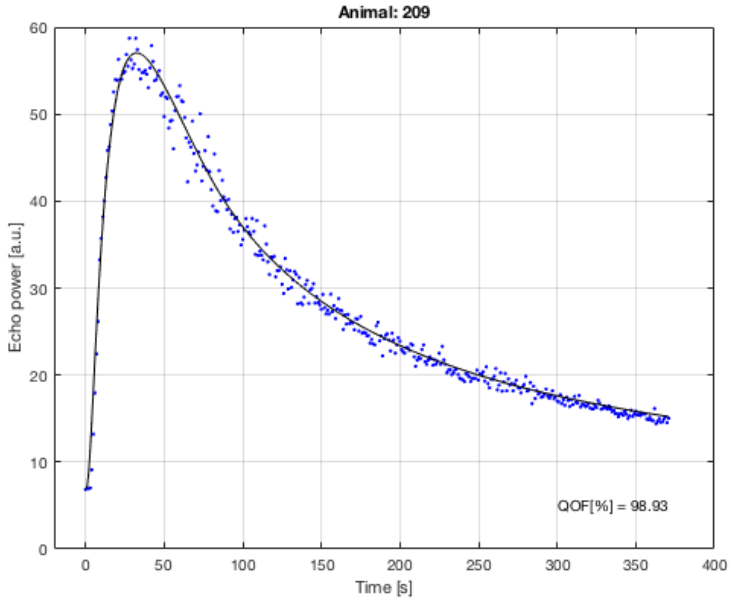

(b)

Figure 5.1: Examples of CEUS curve for the total tumor of (a) one CT26 and (b) one 4T1 tumor. The dots are the linearized signal, while the solid line is the curve fit. The quality of the curve fit (QOF[%]) is displayed in the lower right corner.

5.1.2 CEUS Parameters

CEUS parameters for CT26 tumors are presented in Figure 5.2 and 5.3, for 4T1 tumors in Figure 5.4 and for KPC tumors in Figure 5.5. Parameters displayed are peak enhancement, wash-in area under the curve, rise time and wash-in rate. Parameters are described previously in Figure 2.4. Every parameter is shown for each tumor ROI. Values for each animal is represented by a dot. The means and standard deviations (SD) are also included. Raw data for all CEUS parameters, means and SDs are given in Appendix A. Table A.1, A.2 and A.3 and Table A.4, A.5 and A.6 presents values for CT26 animals, Table A.7, A.8 and A.9 presents values for 4T1 animals, while Table A.10, A.11 and A.12 presents values for KPC. VevoCQ failed to generate sufficient curve fits for two tumors. Data from these tumors was excluded.

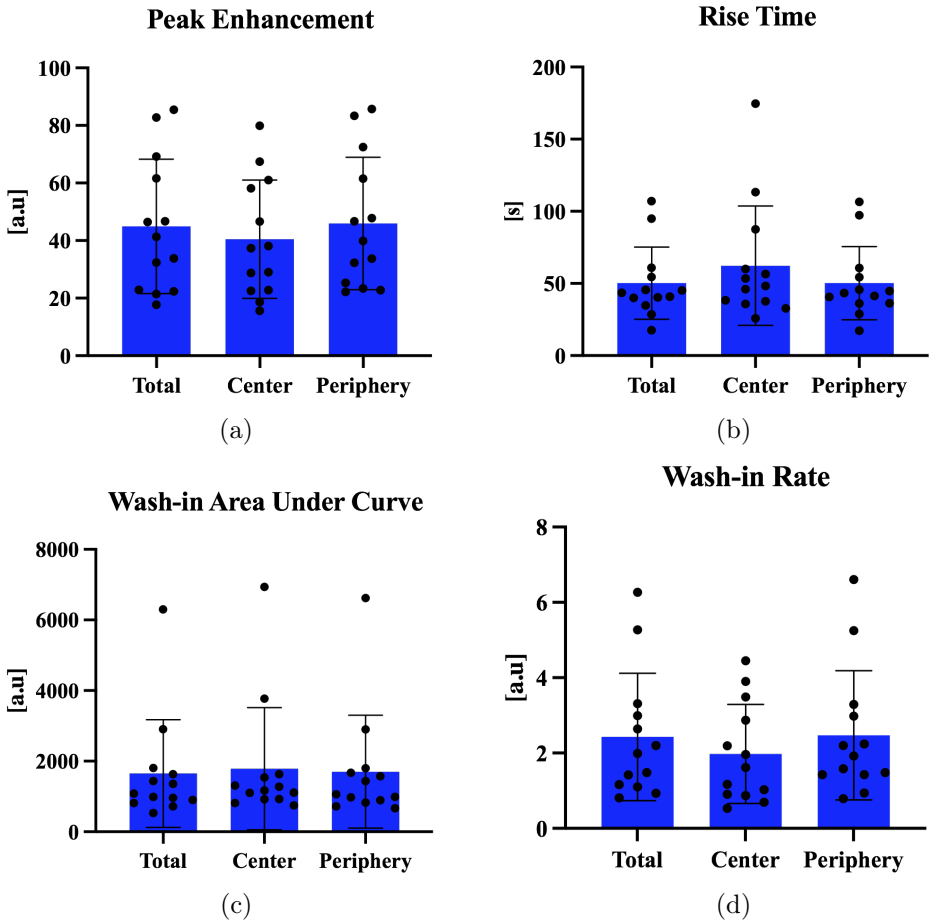

Figure 5.2: CEUS parameters for the total tumor, center and periphery of CT26-1 tumors. Every dot represents an animal. The bar indicates the mean, while the error bar indicates the standard deviation. Figure (a) shows Peak Enhancement (PE), (b) Rise Time (RT), (c) Wash-in Area Under Curve (WiAUC) and (d) Wash-in Rate (WiR).

Two different sets of CT26 CEUS data are presented. The animals presented in Figure 5.2 were part of the USMB perfusion study, while the animals in Figure 5.3 are the ones that were part of the liposomal uptake study. The two CT26 groups will be referred to as CT26-1 and CT26-2, respectively.

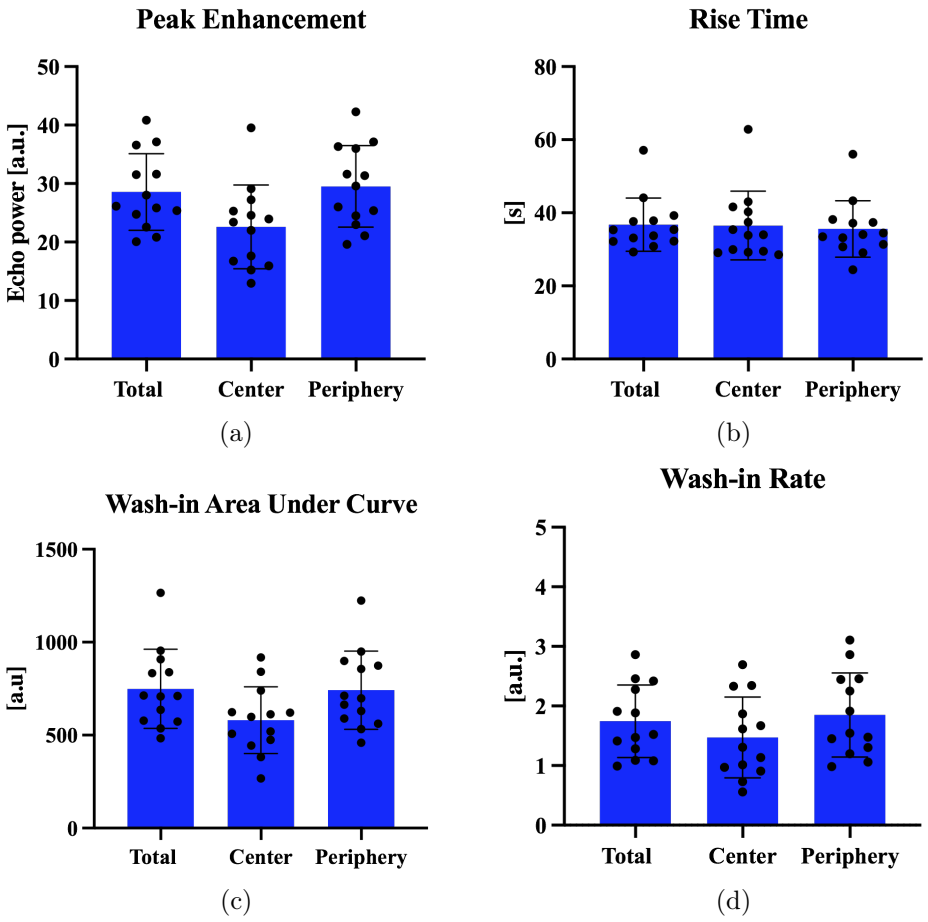

Figure 5.3: CEUS parameters for the total tumor, center and periphery of CT26-2 tumors. Every dot represents an animal. The bar indicates the mean, while the error bar indicates the standard deviation. Figure (a) shows Peak Enhancement (PE), (b) Rise Time (RT), (c) Wash-in Area Under Curve (WiAUC) and (d) Wash-in Rate (WiR).

Mean peak enhancement in the total tumor was 45.0 ± 23.3 and 28.6 ± 6.5 for the two CT26 groups, 34.4 ± 13.3 for 4T1 and 37.0 ± 13.9 for KPC tumors. The mean rise time was 50.3 ± 25.0s and 36.8 ± 7.3s for CT26, 27.6 ± 5.4s for 4T1 and 20.3 ± 5.0s for KPC. Mean wash-in area under the curve was 1650 ± 1526 and 749 ± 212 for CT26, 642 ± 233 for 4T1 and 497 ± 160 for KPC tumors. Finally, the mean wash-in rate was 2.4 ± 1.7 and 1.7 ± 0.6 for CT26, 2.7 ± 1.3 for 4T1 and 3.9 ± 2.2 for KPC. A large variance was observed for all tumor models. ANOVA or Kruskal-Wallis tests, depending on whether the data sets were normally distributed, was used to test for significance between the CEUS parameters for

the total tumor of all tumor models. For PE, the test showed no significant differences. In the case of WiAUC, values for both groups of CT26 tumors were significantly higher than KPC ($p < 0.001$ and $p = 0.04$), and CT26-1 significantly higher than 4T1 ($p = 0.005$). The same applies for RT ($p < 0.0001$, $p = 0.01$ and $p = 0.005$) When it comes to WiR, values for KPC were significantly higher than CT26-2 ($p = 0.02$). Statistical analysis was also performed to compare the tumor regions. PE was significantly lower in the center than periphery for CT26-2 ($p = 0.04$). WiAUC, RT and WiR was not significantly different between regions for any of the tumor types. However, a trend of lower values in the tumor center than periphery was observed for PE, WiAUC and WiR for all models.

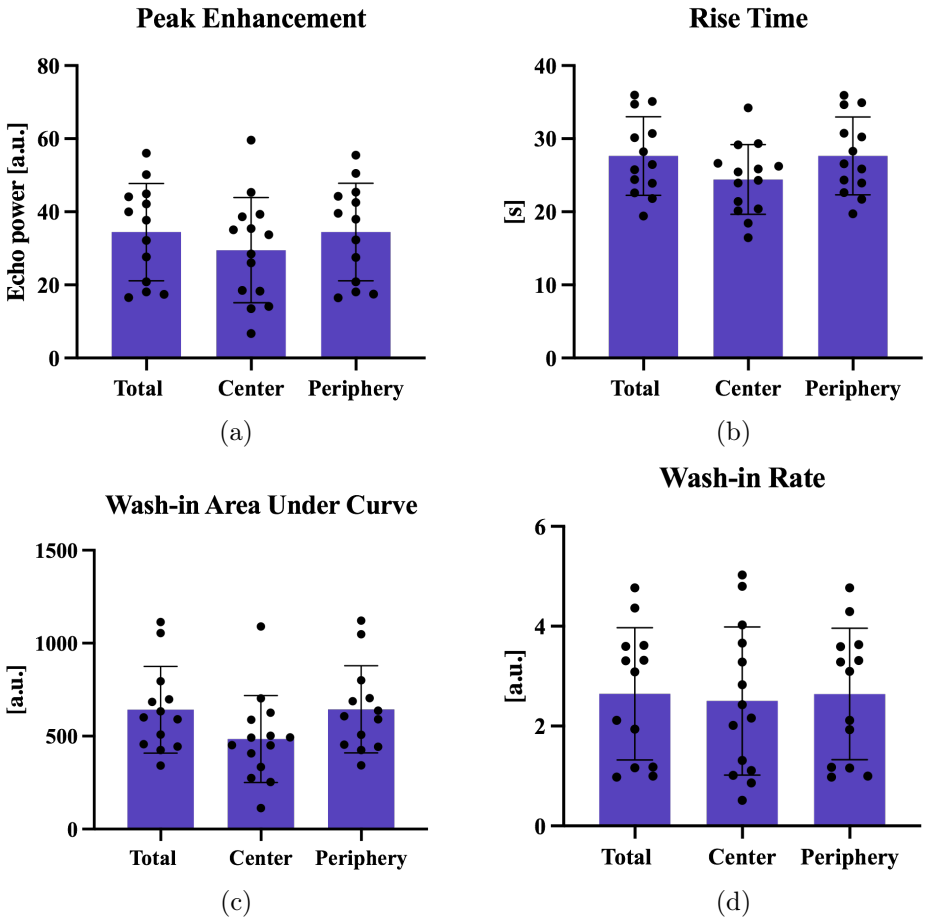

Figure 5.4: CEUS parameters for the total tumor, center and periphery of 4T1 tumors. Every dot represents an animal. The bar indicates the mean, while the error bar indicates the standard deviation. Figure (a) shows Peak Enhancement (PE), (b) Rise Time (RT), (c) Wash-in Area Under Curve (WiAUC) and (d) Wash-in Rate (WiR).

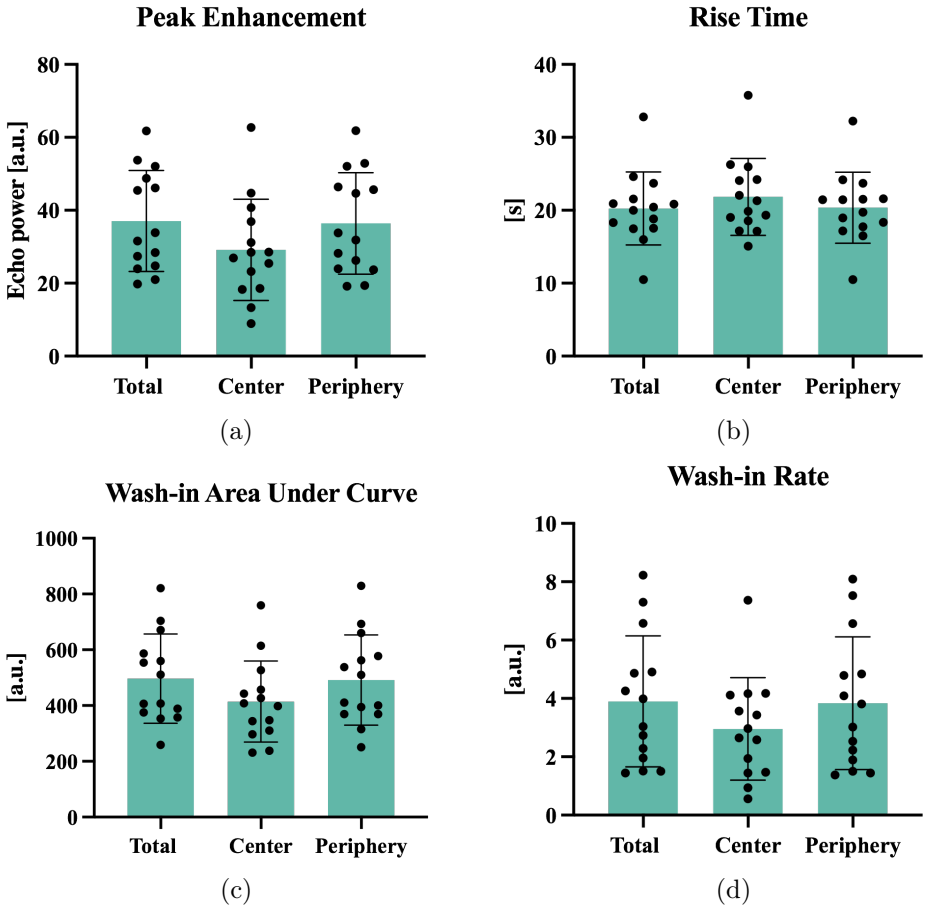

Figure 5.5: CEUS parameters for the total tumor, center and periphery of KPC tumors. Every dot represents an animal. The bar indicates the mean, while the error bar indicates the standard deviation. Figure (a) shows Peak Enhancement (PE), (b) Rise Time (RT), (c) Wash-in Area Under Curve (WiAUC) and (d) Wash-in Rate (WiR).

5.1.3 Relationship between CEUS Parameters and Tumor Weight

The relationship between CEUS parameters and tumor weight was evaluated for CT26-1 tumors included in the perfusion study. Results are presented in Figure 5.6. PE and WiR had a significant strong and negative correlation, demonstrating that PE and WiR decrease with increasing tumor weight. WiAUC had a insignificant moderate and negative correlation. For RT, the correlation was weakl, insignificant and positive. Correlation parameters (r, R^2 and p) are presented in Table A.31 in Appendix A.

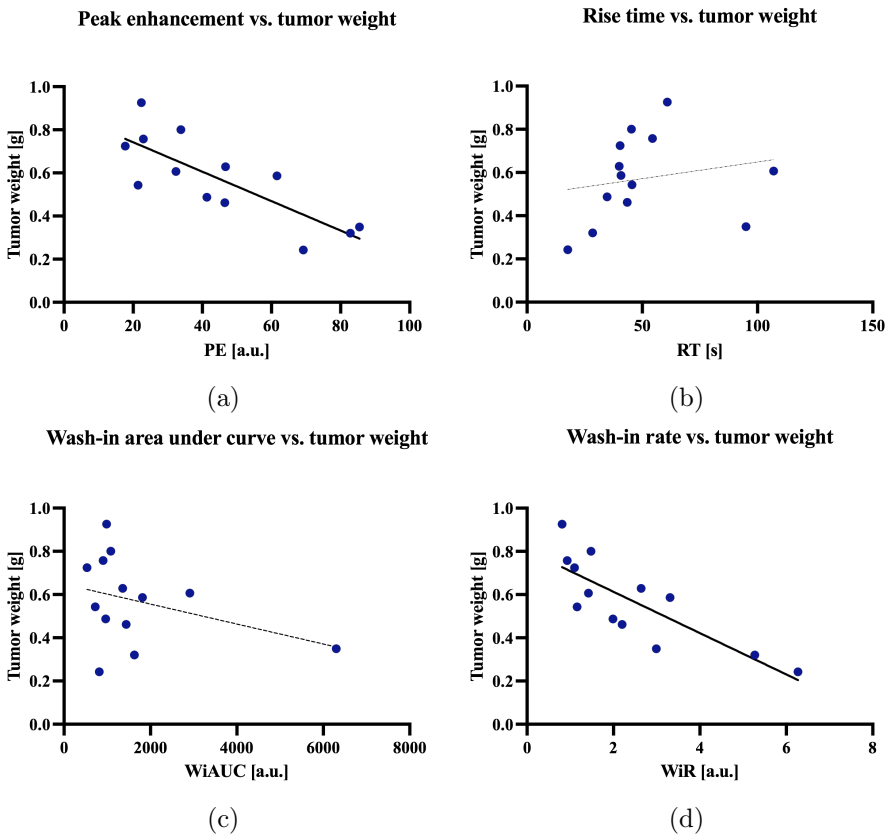

Figure 5.6: Correlation between CEUS parameters and tumor weight for CT26-1 animals. The correlation for peak enhancement is shown in (a), rise time in (b), wash-in area under the curve in (c) and wash-in rate in (d). Dots represent individual animals in the control and treated group. Dashed lines represent moderate (medium line) and weak (thin line) insignificant correlations. A solid line represents a strong significant correlation.

5.2 Effect of US and Sonovue on Fraction of Functional Tumor Blood Vessels

To study the effect of USMB treatment with Sonovue® MBs on the tumor vasculature and perfusion in CT26 and 4T1 tumors, CLSM tile scans were processed and analyzed in order to quantify the total amount of blood vessels and fraction of functional blood vessels, i.e. perfused blood vessels. HES-stained sections provided supplementary support in the analysis. Tumor vasculature parameters were correlated to CEUS parameters for CT26 tumors.

5.2.1 HES Images

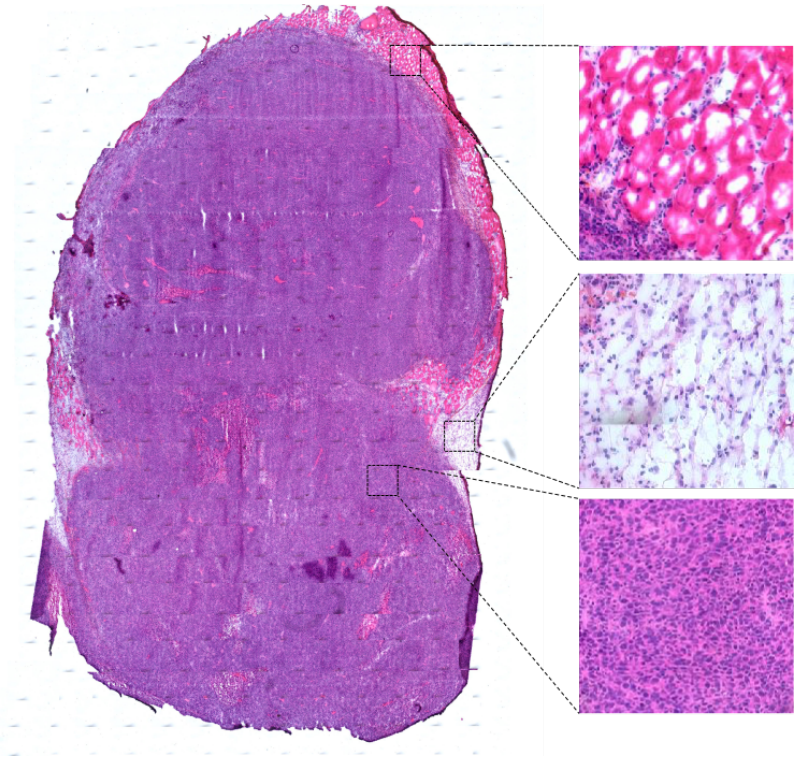

Figure 5.7: Brightfield tile scan image of a HES-stained CT26 tumor section from the treated group, and lose-up of of muscle tissue (upper image), edema/necrosis and tumor tissue.

HES stained sections enabled identification of other tissue than tumor tissue, which was excluded from quantification of tumor blood vessels in the USMB and ACT experiments. Figure 5.7 demonstrates how different tissue types appear in the HES-stained sections. Tumor tissue appears as purple, where the tumor cells are dark violet and tightly spaced.

Muscle tissue appears as bright pink, while edema and necrosis is white and light purple. Distinguishing between edema end necrosis turned out to be a challenge. Connective tissue or ECM appears as orange, however this was only vaguely visible in most tumor sections.

5.2.2 CLSM Blood Vessel Single Images

To have a closer look at the blood vessels, single images with 20x magnification were acquired from different regions of the tumors. In order to demonstrate how the signal from AF647/CD31 (red) and FITC-LEL (green) appears, Figure 5.8 (a) and (b) presents unprocessed CLSM arbitrary single images from two tumors. Both the red and the green channel are shown separately, as well as the composite. Images of the control sections only stained with the secondary antibody, revealed only a small amount of autofluorescence and unspecific binding of the IgG-AF647 in the tumor tissue, which is vaguely visible in the background of both channels in Figure 5.8. Due to the weak signal, these images are not presented.

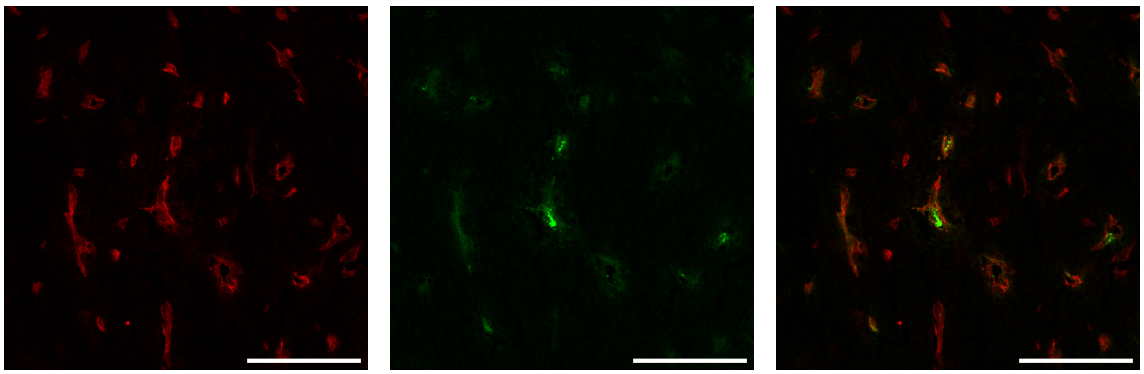

(a) Animal 79

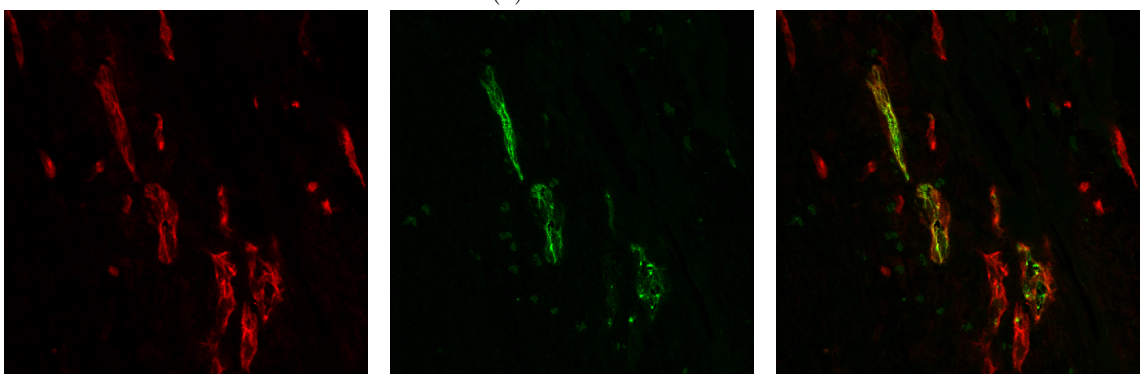

(b) Animal 87

Figure 5.8: Unprocessed blood vessel CLSM single images from two CT26 animals from the (a) control and (b) Sonovue and US treated group. The first column shows the red channel (AF647), the second column is the green channel (FITC-LEL) and the third column the composite of both channels. The scale bar is 100 µm and applies to all images.

5.2.3 CLSM Tile Scans of CT26 and 4T1 Tumors

CLSM tile scans of blood vessels and the respective HES-stained section of one treated CT26 and one control 4T1 tumor are presented in Figure 5.9 and Figure 5.10, respectively. The images are composites of the red and green channel after image processing and thresholding (binary). Red pixels are CD31, showing all blood vessels, while green pixels are FITC-LEL, showing functional blood vessels. The fraction of functional blood vessels for the CT26 tumor was 0.11, and displays few functional vessels. This low fraction is representative for treated animals. The control 4T1 had a fraction of functional vessels of 0.32, and was the tumor with the highest fraction among 4T1 tumors.

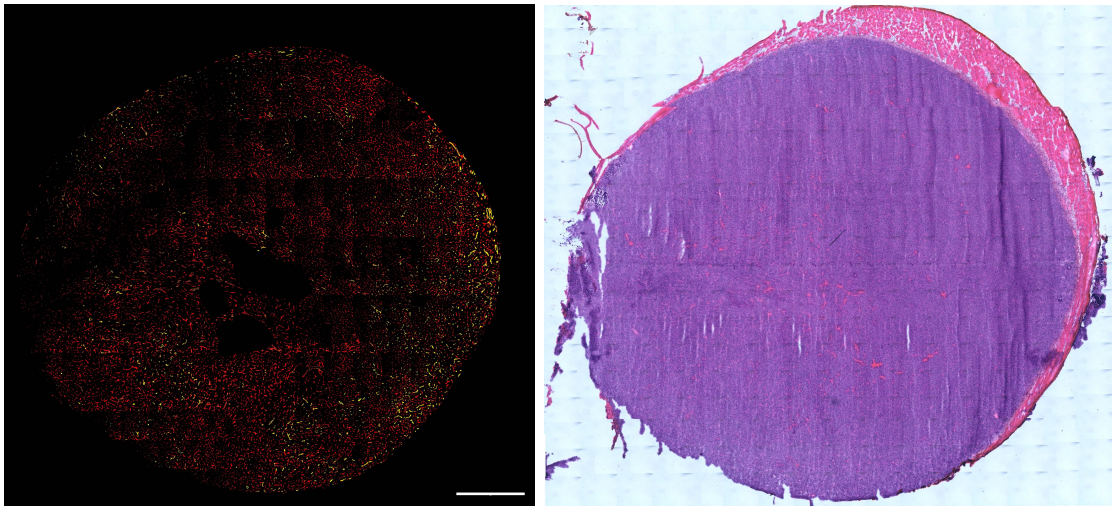

(a) (b)

Figure 5.9: CLSM tile scans of a CT26 tumor section from the Sonovue and US treated group. Figure (a) shows blood vessels. Red pixels in the blood vessel image are CD31 (all blood vessels), while green pixels are FITC (functional blood vessels). The image are processed and thresholded, and thus binary. Figure (b) shows the HES-stained section. Scale bar is 1000 µm.

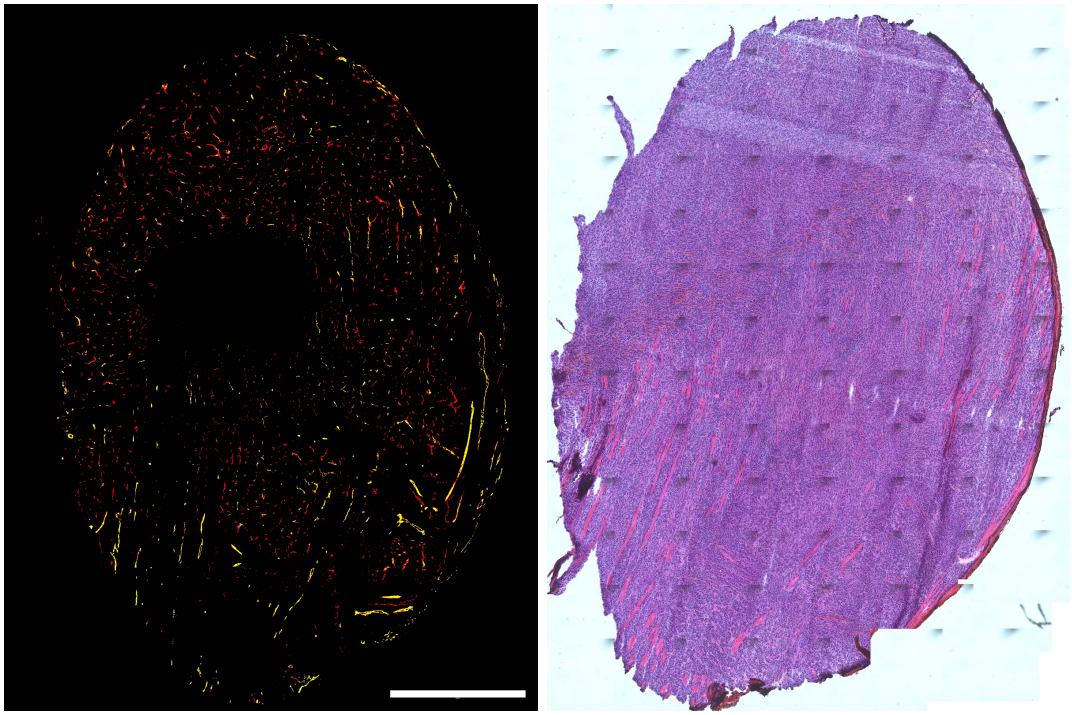

(a) (b)

Figure 5.10: CLSM tile scans of a 4T1 tumor section from the control group. Figure (a) shows blood vessels. Red pixels in the blood vessel image are CD31 (all blood vessels), while green pixels are FITC (functional blood vessels). The image are processed and thresholded, and thus binary. Figure (b) shows the HES-stained section. Scale bar is 1000 µm.

5.2.4 Total Amount of Blood Vessels and Fraction of Functional Blood Vessels for CT26 Tumors

Quantification of the total amount of blood vessels and the amount of functional blood vessels was performed in ImageJ. From this, the fraction of functional blood vessels of the tumor sections was calculated. In figure 5.11 and 5.12, the total amount of blood vessels and fraction of functional blood vessels for CT26 tumors are presented together with the mean and standard deviation. Individual animals are indicated by dots in the control group, and triangles in the treated group. Table A.13 in Appendix A presents results from both groups and all tumor regions. Means, standard deviations, relative change and significance levels for the control and treated group and all regions are given in Table A.16.

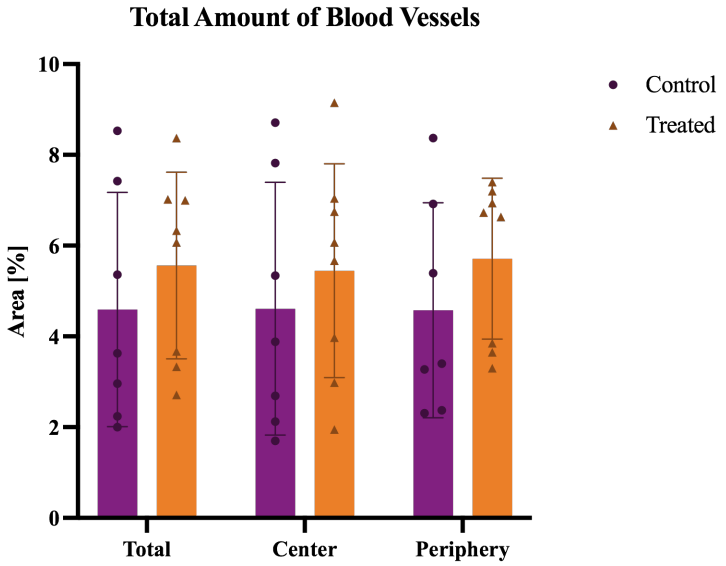

Figure 5.11: Total amount of blood vessels of one tumor section of individual CT26 animals in the control group (purple) and the treated group (orange). The bar indicates the mean, and the error bars the standard deviation.

No significant difference was observed between the control and treated group for the total amount of blood vessels. The mean for each region is also very similar. The control group had means of 4.59±2.58%, 4.61±2.79% and 4.58±2.4% for the total, center and periphery, while for the treated group the means were $5.56 \pm 2.06\%$, $5.45 \pm 2.34\%$ and $5.71 \pm 1.77\%$. On the contrary, the fraction of functional blood vessels was significantly lower in the treated versus control animals in all tumor regions ($p = 0.011$, $p = 0.013$, $p = 0.015$). This implies that USMB with Sonovue reduced the fraction of perfused tumor blood vessels significantly. The control group had means of 0.24 ± 0.15, 0.21 ± 0.15 and 0.27 ± 0.16 for the total, center and periphery, respectively. For the treated group the means were 0.07 ± 0.04, 0.05 ± 0.04 and 0.1 ± 0.06. The relative reduction (%) between control and treated was 71% in the total tumor, 76% in the center and 63% in the periphery.

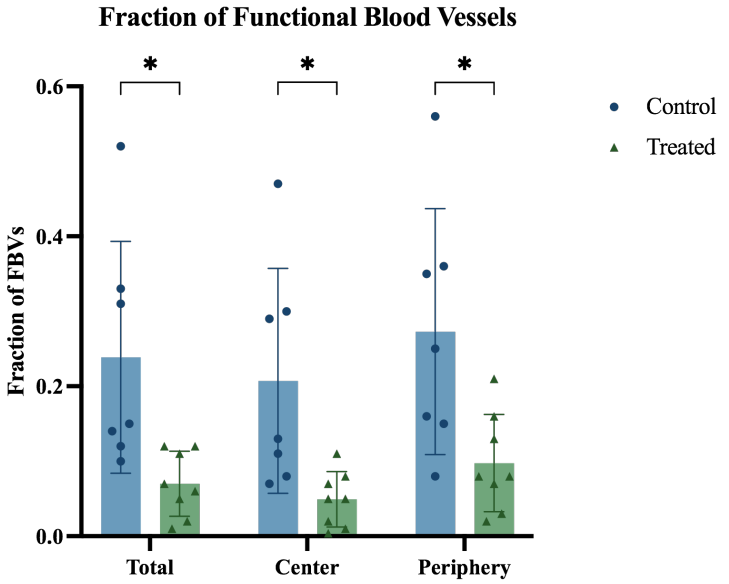

Figure 5.12: Fraction of functional blood vessels of one tumor section of individual CT26 animals in the control group (blue) and the treated group (green). The bar indicates the mean, and the error bars the standard deviation. Significant difference ($p < 0.05$) is indicated by *.

5.2.5 Total Amount of Blood Vessels and Fraction of Functional Blood Vessels for 4T1 Tumors

Quantification of the total amount of blood vessels and the amount of functional blood vessels was performed in ImageJ. From this, the fraction of functional blood vessels of the tumor sections was calculated. In figure 5.13 and 5.14, the total amount of blood vessels and fraction of functional blood vessels for 4T1 tumors are presented together with the mean and standard deviation. Individual animals are indicated by dots in the control group, and triangles in the treated group. Table A.14 in Appendix A presents results from both groups and all tumor regions. Means, standard deviations, relative change and significance levels for the control and treated group and all regions are given in Table A.17.

No significant difference was observed between the control and treated group for the total amount of blood vessels. The mean for each region was also very similar. The control group had means of 3.28%, 3.32% and 3.23% for the total, center and periphery, while for the treated group the means were 4.15%, 4.48% and 3.82%. On the contrary, the fraction of functional blood vessels was significantly lower for treated than control animals in the total tumor and periphery ($p = 0.026$ and $p = 0.028$). A trend was also observed in the center, where the $p = 0.057$, slightly above the significance limit ($p<0.05$). The control group had means of 0.14, 0.09 and 0.19 for the total, center and periphery, respectively. For the

treated group, means were 0.04, 0.02 and 0.07. The relative reduction (%) between control and treated was 71% in the total tumor, 78% in the center and 63% in the periphery.

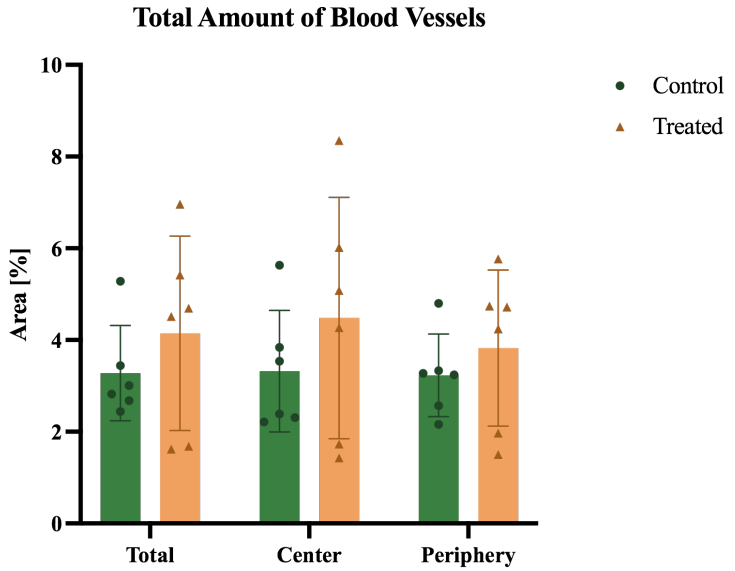

Figure 5.13: Total amount of blood vessels of one tumor section of individual 4T1 animals in the control group (green) and the treated group (yellow). The bar indicates the mean, and the error bars the standard deviation.

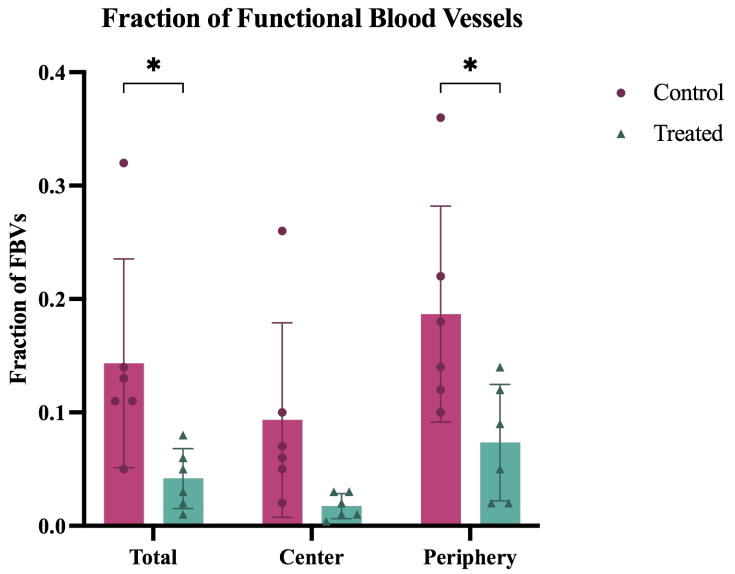

Figure 5.14: Fraction of functional blood vessels of one tumor section of individual 4T1 animals in the control group (pink) and the treated group (cyan). The bar indicates the mean, and the error bars the standard deviation. Significant difference ($p < 0.05$) is indicated by *.

5.2.6 Relationship between Fraction of Functional Blood Vessels and Total Amount of Blood Vessels

Correlation plots of the total amount of blood vessels against the fraction of functional blood vessels are presented in Figure 5.15 for CT26 and Figure 5.16 for 4T1. For CT26, individual animals in the control group are represented by blue dots, while the treated group is represented by green triangles. In all tumor regions, the correlation between total amount of blood vessels and fraction of functional blood vessels was insignificant and positive for both groups. In the total tumor and periphery the correlation was weak for controls and strong for treated animals, whereas it was weak and moderate in the center.

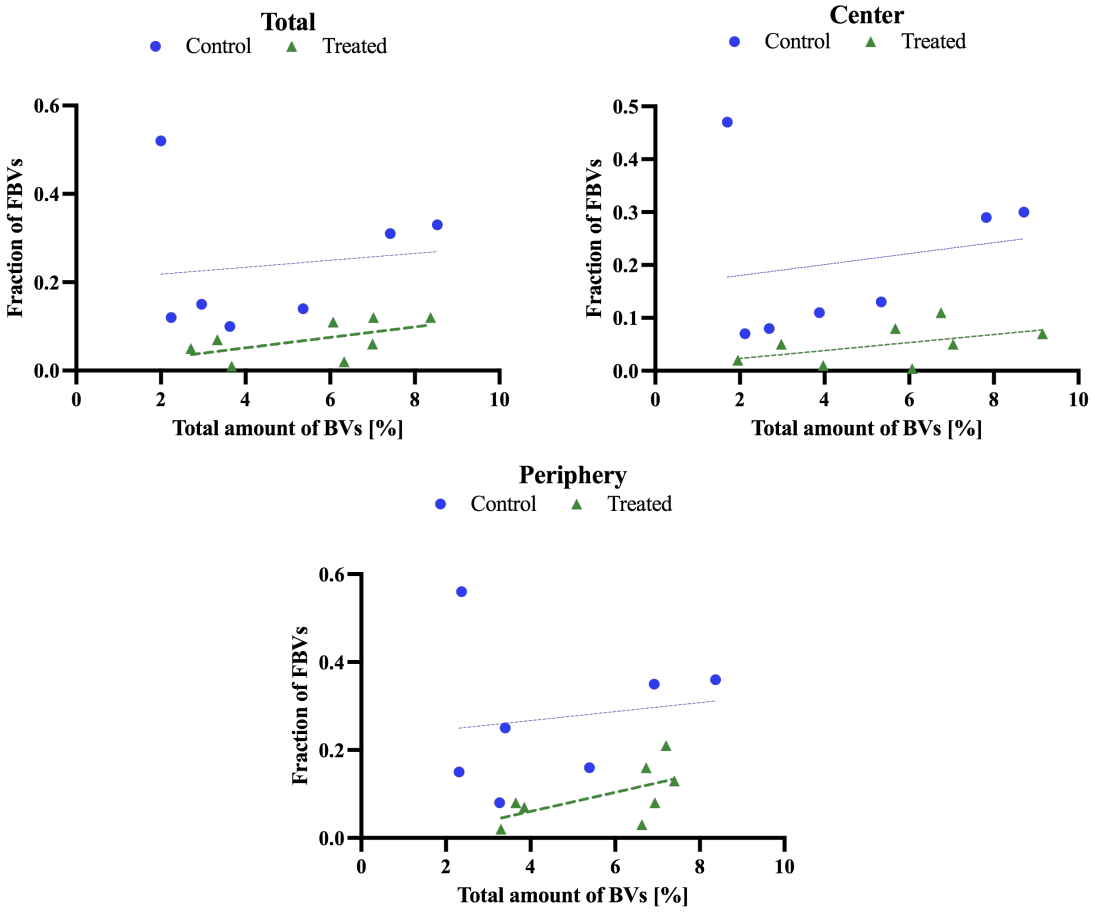

Figure 5.15: Correlation plots for fraction of functional blood vessels and total amount of blood vessels for CT26, a) in the total tumor, (b) in the center and (c) in the periphery of the tumor. Control animals are represented by blue dots, while treated animals are represented by green triangles. The correlation is given by the lines, where a dashed line represents a weak (thin line), moderate (medium thick line) or strong (thick line) insignificant correlation. A solid line would indicate a significant correlation.

For 4T1, controls and treated animals are represented by red and blue, respectively. Statistical analysis of total amount of blood vessels versus fraction of functional blood vessels for 4T1 tumors demonstrated a strong insignificant negative correlation for controls in the total and center, and weak correlation in the periphery. Treated animals animals had a weak insignificant negative correlation in the total and periphery of the tumor. Correlation parameters (r, R^2 and p) for CT26 and 4T1 are presented in Table A.23 and Table A.24 in Appendix A.

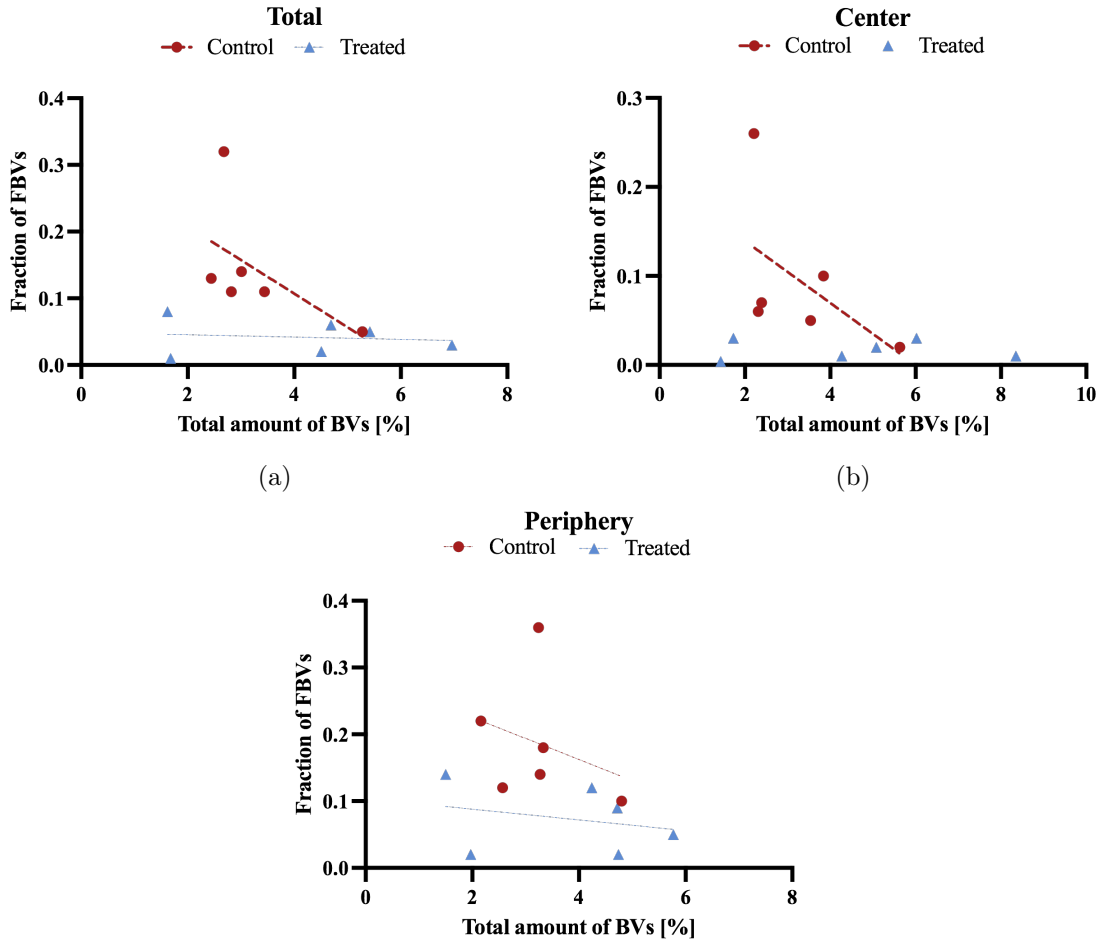

Figure 5.16: Correlation plots for fraction of functional blood vessels and total amount of blood vessels for 4T1, a) in the total tumor, (b) in the center and (c) in the periphery of the tumor. Control animals are represented by red dots, while treated animals are represented by blue triangles. The correlation is given by the lines, where a dashed line represents a weak (thin line), moderate (medium thick line) or strong (thick line) insignificant correlation. A solid line would indicate a significant correlation.

5.2.7 Relationship between Fraction of Functional Blood Vessels and Tumor Weight

Correlation between tumor weight and fraction of functional blood vessels was also investigated. Correlation plots for all tumor regions are presented in Figure 5.17 for CT26 and Figure 5.18 for 4T1. Correlation parameters (r, R^2 and p) for CT26 and 4T1 are presented in Table A.26 and Table A.27 in Appendix A.

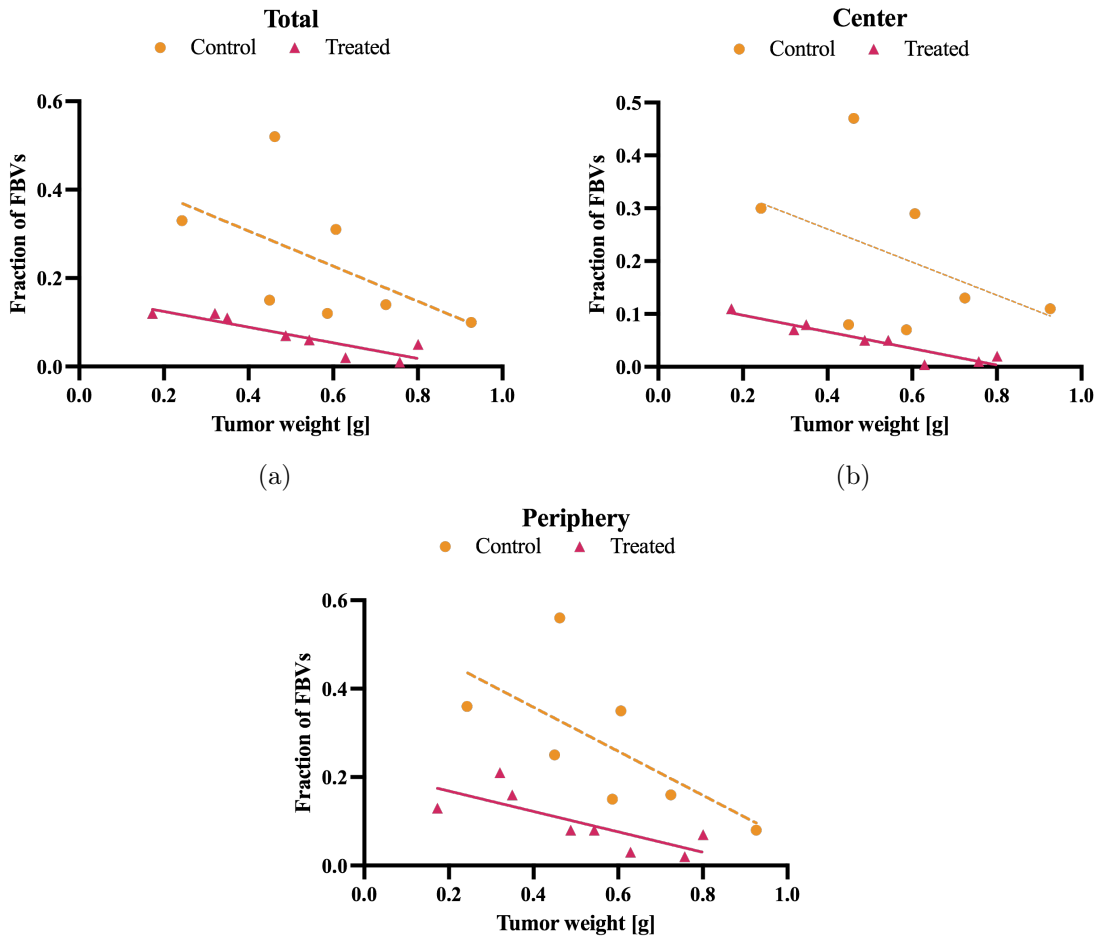

Figure 5.17: Correlation plots for tumor weight and fraction of functional blood vessels for CT26, a) in the total tumor, (b) in the center and (c) in the periphery of the tumor. Control animals are represented by yellow dots, while treated animals are represented by pink triangles. A dashed line indicates a insignificant correlation, while a solid line indicates significant correlation. Depending on the thickness of the line, the correlation is weak (thin line), moderate (medium line) or strong (thick line).

Individual animals in the control group are represented by orange dots, while the treated group is represented by pink triangles. For CT26, the correlation between tumor weight and fraction of functional blood vessels was strong significant and negative for treated animals in all tumor regions. The control group had a negative insignificant correlation in all regions, strong for the total and periphery, and moderate in the center. 4T1 control animals had a strong insignificant negative correlation. Treated animals had a weak insignificant correlation in the total tumor, whereas the correlation was negligible in the center and periphery.

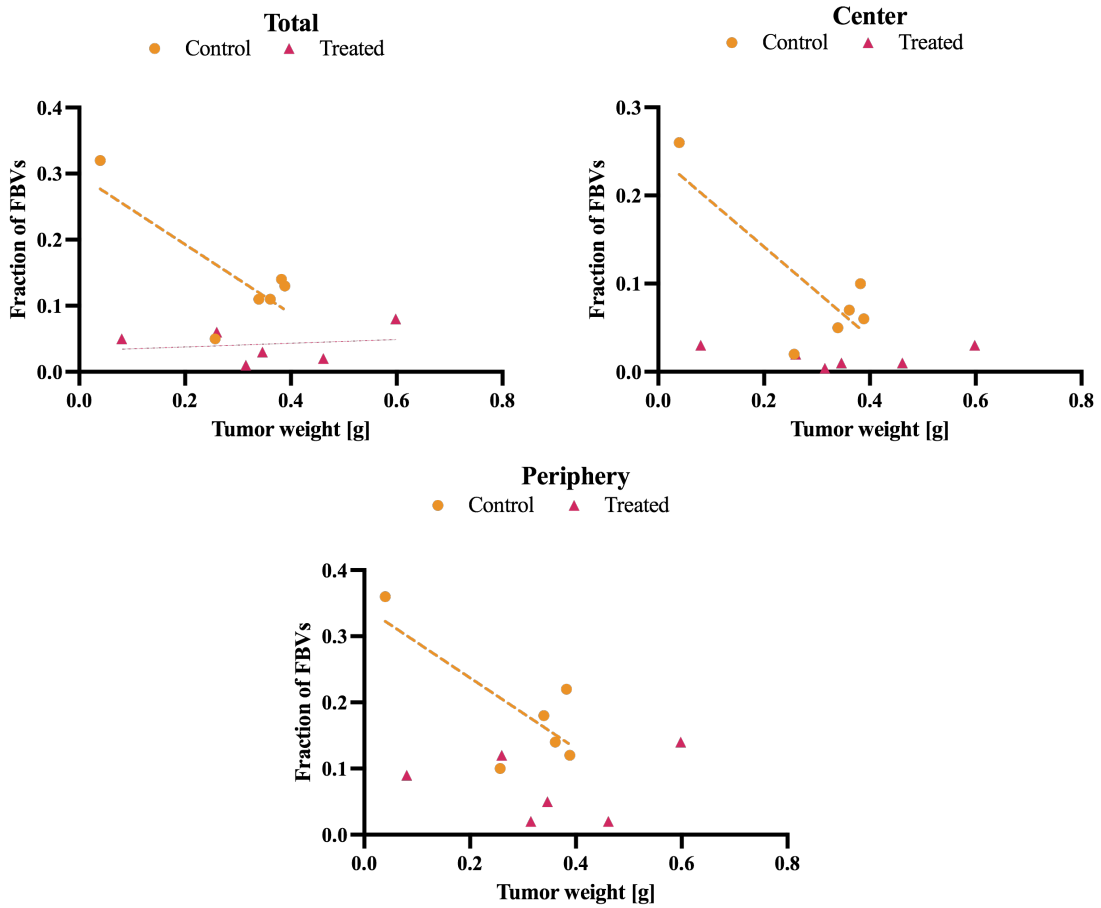

Figure 5.18: Correlation plots for tumor weight and fraction of functional blood vessels for 4T1, a) in the total tumor, (b) in the center and (c) in the periphery of the tumor. Control animals are represented by yellow dots, while treated animals are represented by pink triangles. A dashed line indicates a insignificant correlation. Depending on the thickness of the line, the correlation is weak (thin line), moderate (medium line) or strong (thick line). A solid line would indicate a significant correlation.

5.2.8 Relationship between CEUS Parameters and Fraction of Functional Blood Vessels

Correlation between CEUS perfusion parameters and fraction of functional blood vessels was investigated to explore the compability of two methods of measuring perfusion. Only control animals were included in the correlation analysis, since CEUS was done prior to USMB treatment. Results for the PE, RT, WiAUC and WiR versus fraction of functional blood vessels in the total tumor are presented in Figure 5.19. PE had moderate insignificant and positive correlation with fraction of FBVs. WiAUC and WiR had a weak positive insignificant correlation. For RT, the correlation was negligible. Correlation parameters (r, R^2 and p) are presented in Table A.29 in Appendix A.

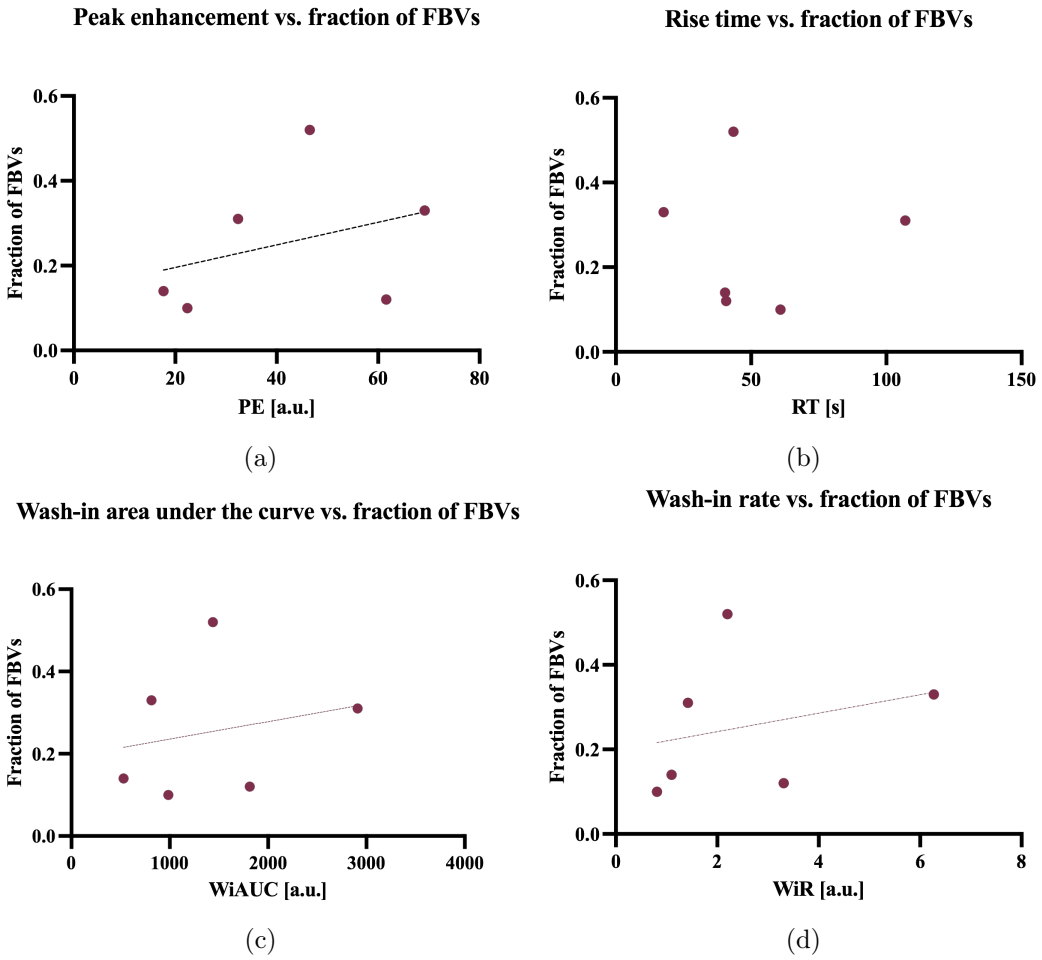

Figure 5.19: Correlation between CEUS parameters and fraction of functional blood vessels for CT26 animals. The correlation for peak enhancement is shown in (a), rise time in (b), wash-in area under the curve in (c) and wash-in rate in (d). Dots represent individual animals in the control group. Dashed lines represent moderate (medium line) and weak (thin line) insignificant correlations. A solid line would indicate a significant correlation.

5.2.9 Relationship between CEUS Parameters and Total Amount of Blood Vessels

CEUS paramteres for CT26 animals were also correlated with the total amount of blood vessels, to assess if there was a difference to the correlation with fraction of functional blood vessels. Here, all animals are included, as USMB treatment did not affect the total amount of blood vessels. Results are presented in Figure 5.20. PE and WiAUC had a insignificant positive correlation, moderate and weak, respectively. WiR had a strong positive and significant correlation. For RT, the correlation was negligible. Correlation parameters (r, R^2 and p) are presented in Table A.30 in Appendix A.

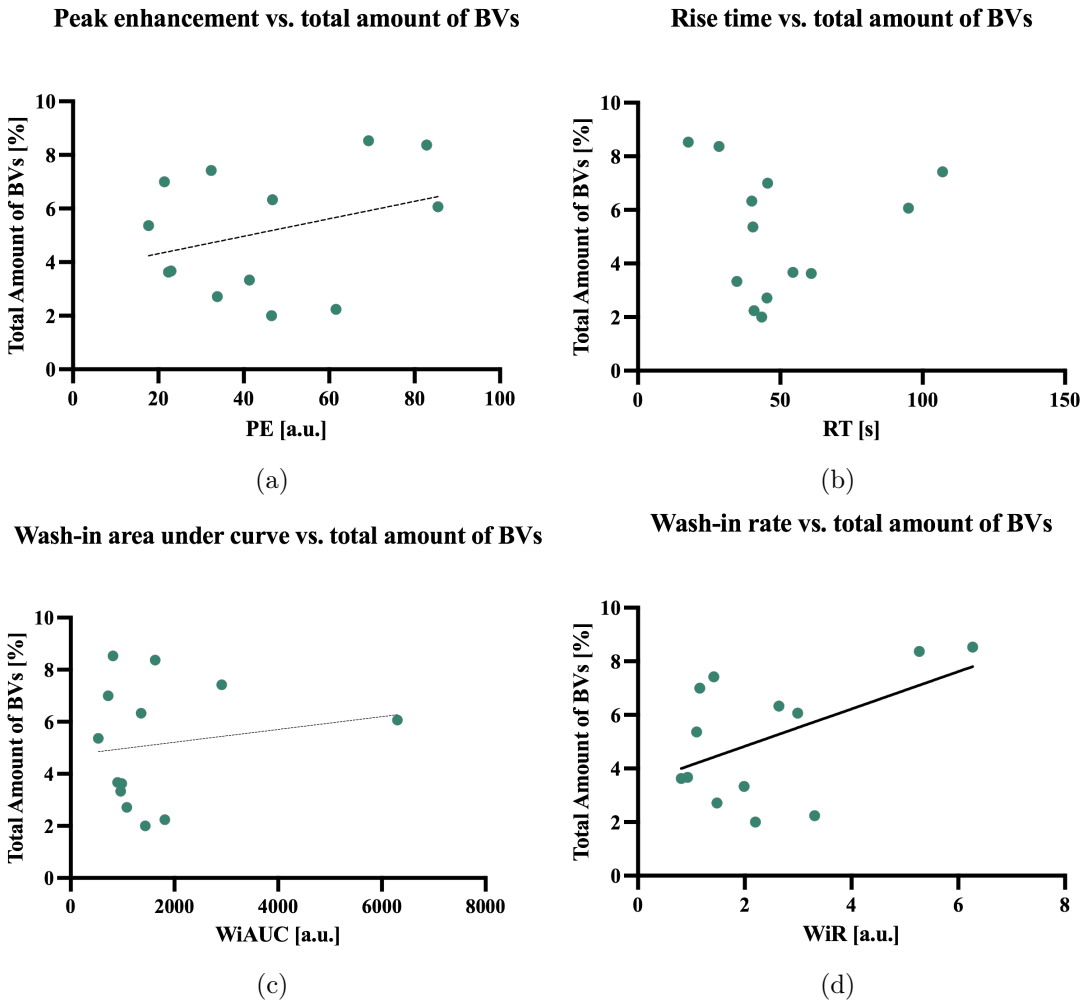

Figure 5.20: Correlation between CEUS parameters and total amount of blood vessels for CT26 animals. The correlation for peak enhancement is shown in (a), rise time in (b), wash-in area under the curve in (c) and wash-in rate in (d). Dots represent individual animals in the control and treated group. Dashed lines represent moderate (medium line) and weak (thin line) insignificant correlations. A solid line represents a strong significant correlation.

5.3 Effect of US and ACT on Fraction of Functional Tumor Blood Vessels

To study the effect of US and ACT treatment on the tumor vasculature and perfusion in CT26 tumors, CLSM tile scans were processed and analyzed in order to quantify the total amount of blood vessels and fraction of functional blood vessels in the tumors. HES-stained sections provided supplementary support in the analysis.

5.3.1 CLSM Tile Scans

CLSM tile scans of blood vessels and the respective HES-stained section of one CT26 tumor are presented in Figure 5.21 (a) and (b). Blood vessels are shown in (a), were the composite of the red and green channel after image processing and thresholding is displayed. Red pixels are CD31, showing all blood vessels, while green pixels are FITC-LEL, showing functional blood vessels. The fraction of functional blood vessels for tumor was 0.31. Comparing to the blood vessel image to the HES image, one can observe the muscle tissue that is excluded from the binary image, an thus excluded from blood vessel quantification.

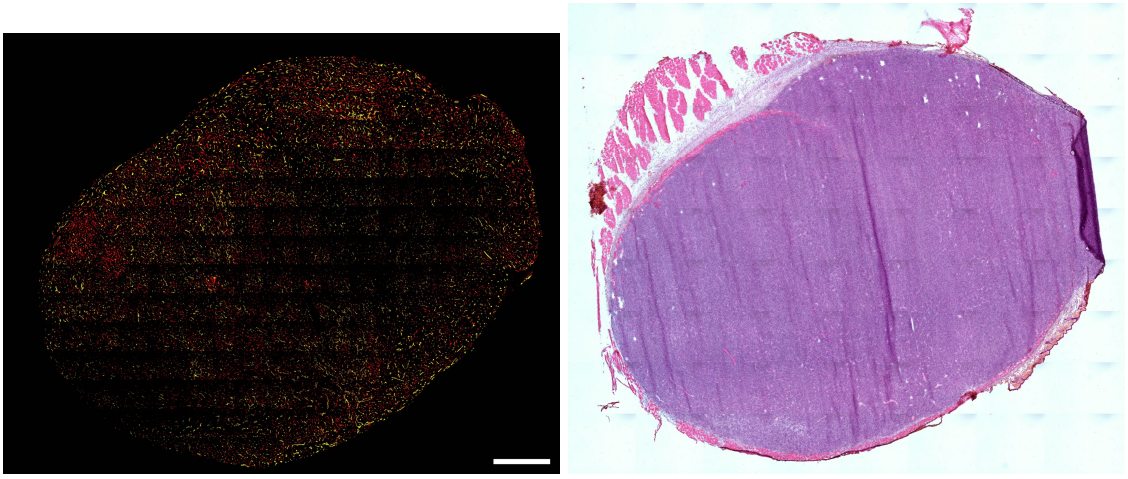

(a) (b)

Figure 5.21: CLSM tile scans of a CT26 tumor section from the control group. Figure (a) shows blood vessels. Red pixels in the blood vessel image are CD31 (all blood vessels), while green pixels are FITC (functional blood vessels). The image are processed and thresholded, and thus binary. Figure (b) shows the HES-stained section. Scale bar is 1000 µm.

5.3.2 Total Amount of Blood Vessels and Fraction of Functional Blood Vessels

Quantification of the total amount of blood vessels and the amount of functional blood vessels was performed in ImageJ, followed by calculation of fraction of functional blood vessels of the tumor sections. In figure 5.22 and 5.23, the total amount of blood vessels and fraction of functional blood vessels for CT26 tumors are presented together with the mean and standard deviation. Individual animals in the control group are indicated by dots, and the treated group by triangles. Table A.15 in Appendix A presents results from both groups and all tumor regions. Means, standard deviations, relative change and significance levels for the control and treated group and all regions are given in Table A.18.

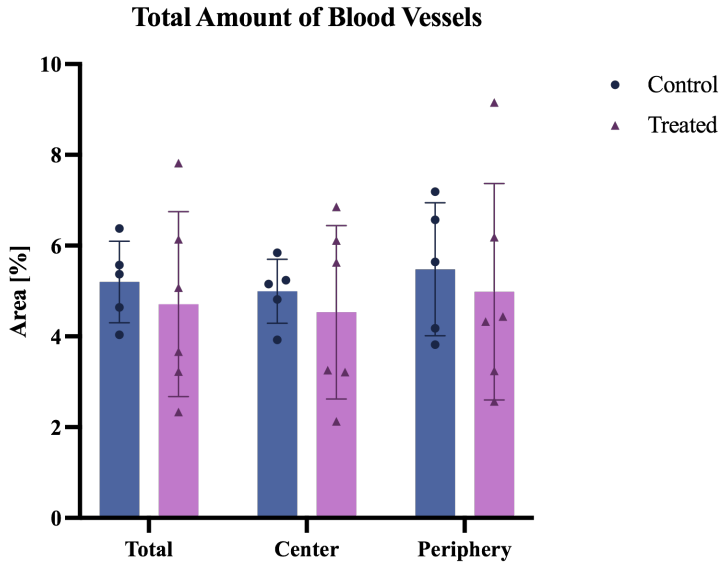

Figure 5.22: Plot of fraction of functional blood vessels of individual CT26 animals in the control group (dots) and the ACT treated group (triangles). The bar indicates the mean, and the error bars the standard deviation.

No significant difference was observed between the control and treated group for the total amount of blood vessels. The mean of all regions was also very similar. The control group had means of 5.2±0.9%, 5.0±0.7% and 5.5±1.5% for the total, center and periphery, while for the treated group the means were $4.7 \pm 2.0\%$, $4.5 \pm 1.9\%$ and $5.0 \pm 2.4\%$. Neither did the fraction of functional blood vessels show significant difference between the control and treated animals in any tumor regions. However, there is a weak trend of reduced perfusion for the treated group. P-values for the total, center and periphery were $p = 0.24$, $p = 0.30$ and $p = 0.28$, respectively. The control group had means of 0.20 ± 0.08, 0.19 ± 0.09 and 0.23 ± 0.08 for the total, center and periphery, respectively. For the treated group the

means were 0.15 ± 0.03, 0.13 ± 0.05 and 0.18 ± 0.05. The relative reduction between control and treated was 25% in the total tumor, 28% in the center and 22% in the periphery.

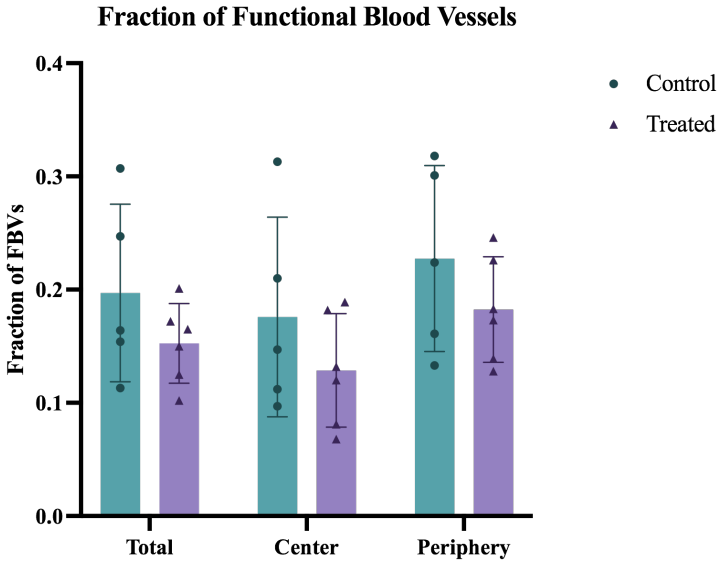

Figure 5.23: Plot of fraction of functional blood vessels of individual CT26 animals in the control group (dots) and the ACT treated group (triangles). The bar indicates the mean, and the error bars the standard deviation.

5.3.3 Relationship between Fraction of Functional Blood Vessels and Total Amount of Blood Vessels

Correlation plots of the total amount of blood vessels against the fraction of functional blood vessels are presented in Figure 5.24. Individual animals in the control group are represented by red dots, while the treated group is represented by blue triangles. The correlation between total amount of blood vessels and fraction of functional blood vessels in the total tumor was insignificant and positive for treated animals, and weak negative for controls. In the center, treated animals had a significant positive correlation, while he correlation was negligible for controls. In the periphery there was a moderate and weak negative and insignificant correlation for control and treated animals, respectively. Correlation parameters (r, R^2 and p) are presented in Table A.25 in Appendix A.

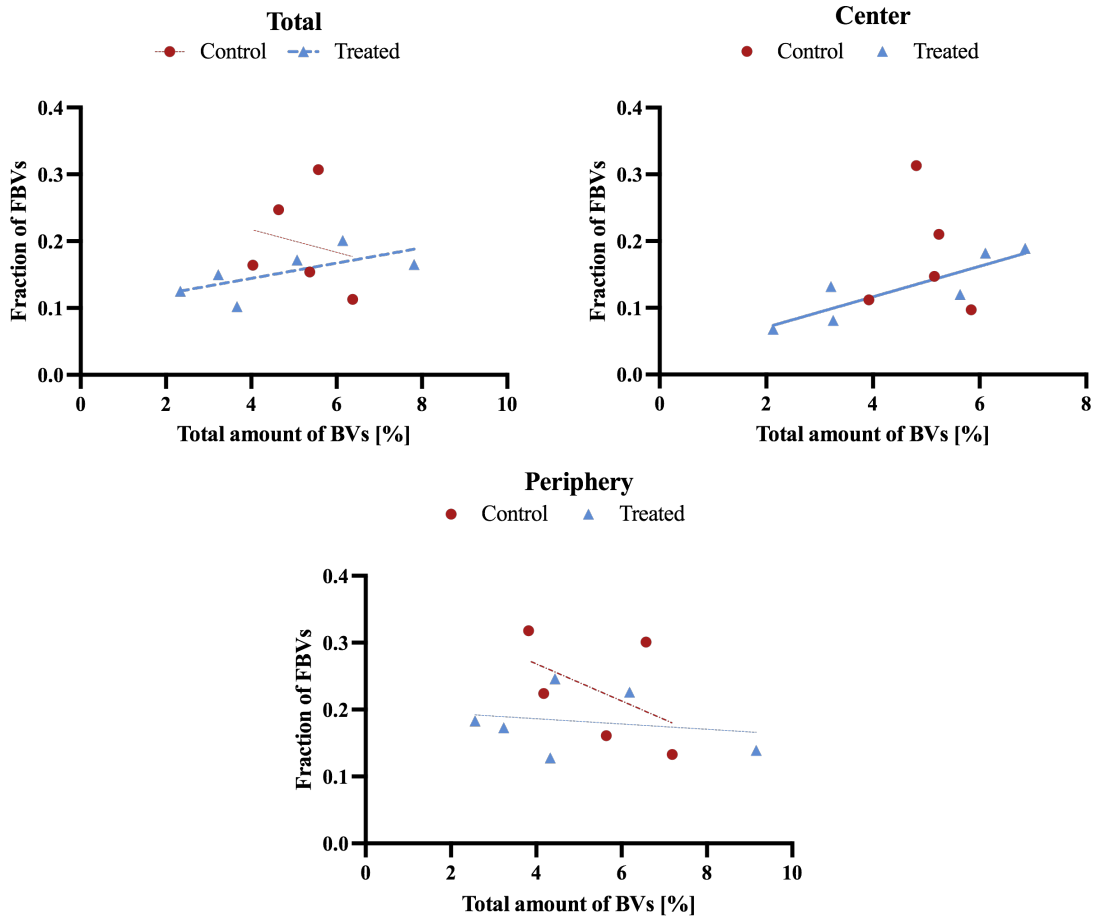

Figure 5.24: Correlation plots for fraction of functional blood vessels and total amount of blood vessels for CT26 included in the ACT experiment, a) in the total tumor, (b) the tumor center and (c) tumor periphery. Control animals are represented by blue dots, while treated animals are represented by green triangles. The correlation is given by the lines, where a dashed line represents a weak (thin line), moderate (medium thick line) or strong (thick line) insignificant correlation. A solid line would indicate a significant correlation

5.3.4 Relationship between Fraction of Functional Blood Vessels and Tumor Weight

Correlation between tumor weight and fraction of functional blood vessels was evaluated. Results for all tumor regions are presented in Figure 5.25. Individual animals in the control group are represented by orange dots, while the treated group is represented by blue triangles. The correlation between tumor weight and fraction of functional blood vessels was insignificant, strong and negative for treated animals in the total tumor and center. In the periphery, the correlation for treated animals had a weak negative and insignificant. Control animals had a negative insignificant correlation in the total and periphery, which was weak and moderate, respectively. Correlation parameters (r, R^2 and p) are presented in Table A.28 in Appendix A.

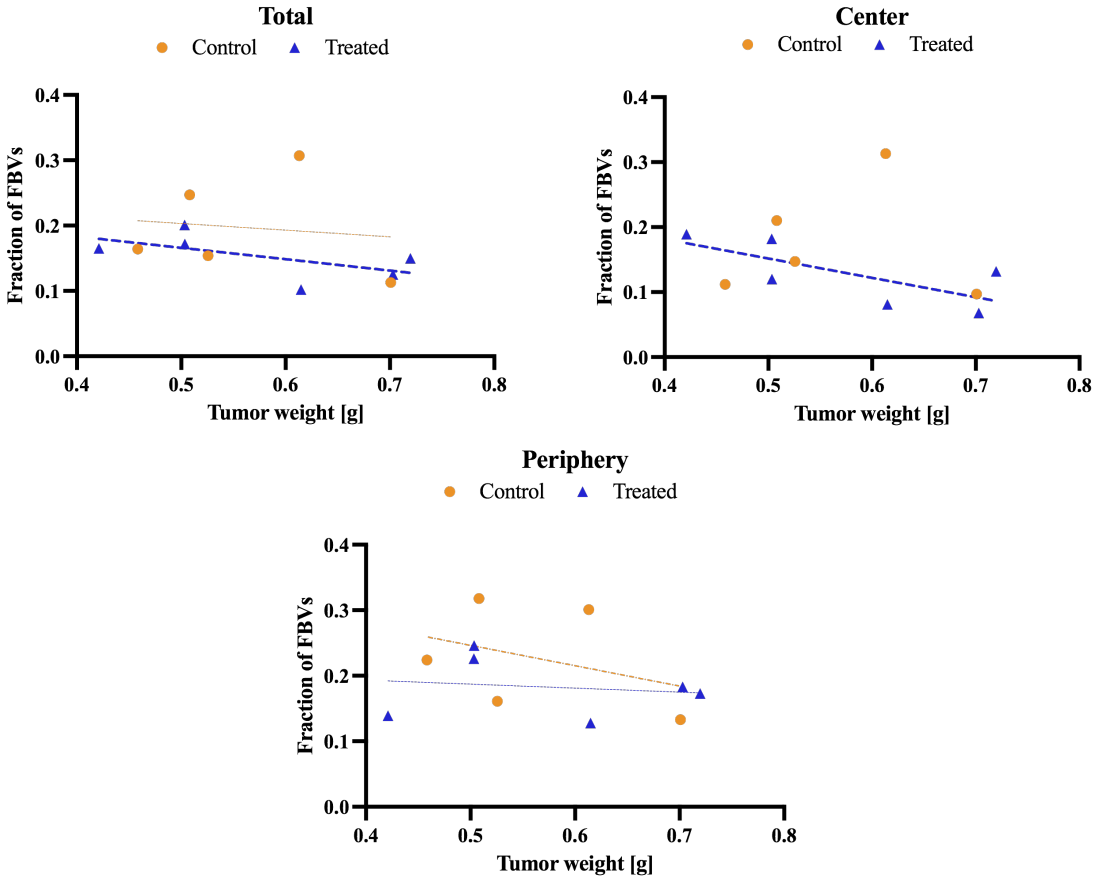

Figure 5.25: Correlation between tumor weight and fraction of functional blood vessels for CT26 tumors in the ACT experiment, a) in the total tumor, (b) the tumor center and (c) tumor periphery. Control animals are represented by yellow dots, while treated animals are represented by pink triangles. A dashed line indicates a insignificant correlation, while a solid line indicates significant correlation. Depending on the thickness of the line, the correlation is weak (thin line), moderate (medium line) or strong (thick line).

5.4 Effect of USMB on Uptake and Microdistribution of Nanoparticles in Tumors

Evaluation of the effect of USMB on the uptake and microdistribution of nanoparticles in CT26, 4T1 and KPC tumors employed two methods of analysis. First of all, Pearl images were analyzed to measure fluorescence from the liposomes, in order to quantify NP uptake in the entire tumor volume. Secondly, CLSM images were analyzed to assess the nanoparticle extravasation distance. Correlation between uptake data and CEUS parameters was investigated to reveal possible biomarkers relevant for patient stratification.

5.4.1 Nanoparticle Uptake in Tumors

Analysis of Pearl images to obtain NP uptake data was performed by Caroline Einen. Mean fluorescence was chosen as the parameter to present and correlate with extravasation and CEUS data, and describes the measured mean fluorescence intensity ex vivo of the tumor 24h post treatment. The mean fluorescence is a measure of NP uptake in the tumor. Instead of using uptake data from an earlier point, e.g. right after treatment, ex vivo uptake data are displayed here for the reason that CLSM images were acquired from ex vivo tumors. Mean fluorescence for control and USMB treated groups for CT26, 4T1 and KPC tumors are presented in Figure 5.26. Raw data are attached in Table A.19 in Appendix A.

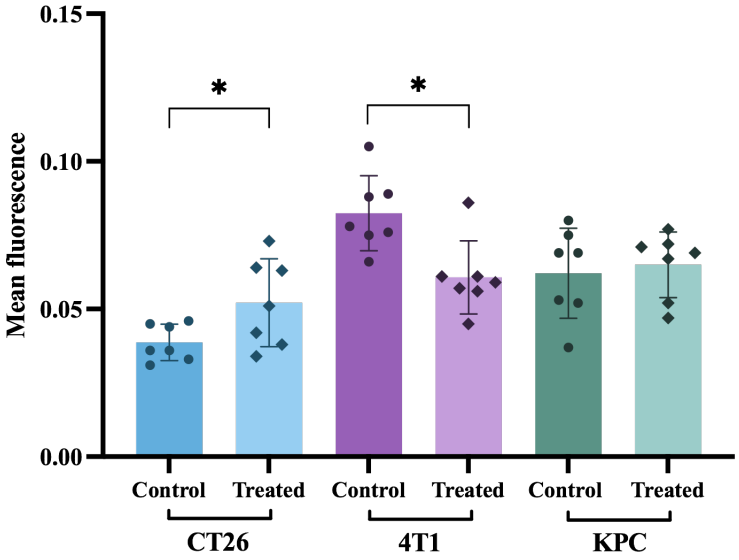

Figure 5.26: Tumor uptake of NPs measured by mean fluorescence for control and USMB treated CT26, 4T1 and KPC animals. Individual animals are represented by dots (control) and squares (treated). Bars indicate the mean, while the error bars indicate the standard deviation. Statistical significance is highlighted with *.

Within each tumor model, statistical significance was observed between control and treated animals for CT26 and 4T1. For CT26, tumor uptake was significantly higher ($p = 0.048$) in USMB treated 0.05 ± 0.015 than in control animals (0.04 ± 0.006), a relative increase of 25%. For 4T1, the opposite occurred, with significantly ($p = 0.007$) higher tumor uptake in controls (0.08 ± 0.013) versus treated animals (0.06 ± 0.012), a relative decrease of -25%. USMB did not change the uptake in KPC tumors. Differences in tumor uptake in controls was different between the tumor models. CT26 controls had a mean of 0.04 ± 0.006, while the mean of 4T1 controls was 0.08 ± 0.013, meaning that the NP uptake in 4T1 was twice the uptake in CT26 without treatment. KPC controls had a mean of 0.06 ± 0.015.

5.4.2 CLSM Images of Blood Vessels and NPs

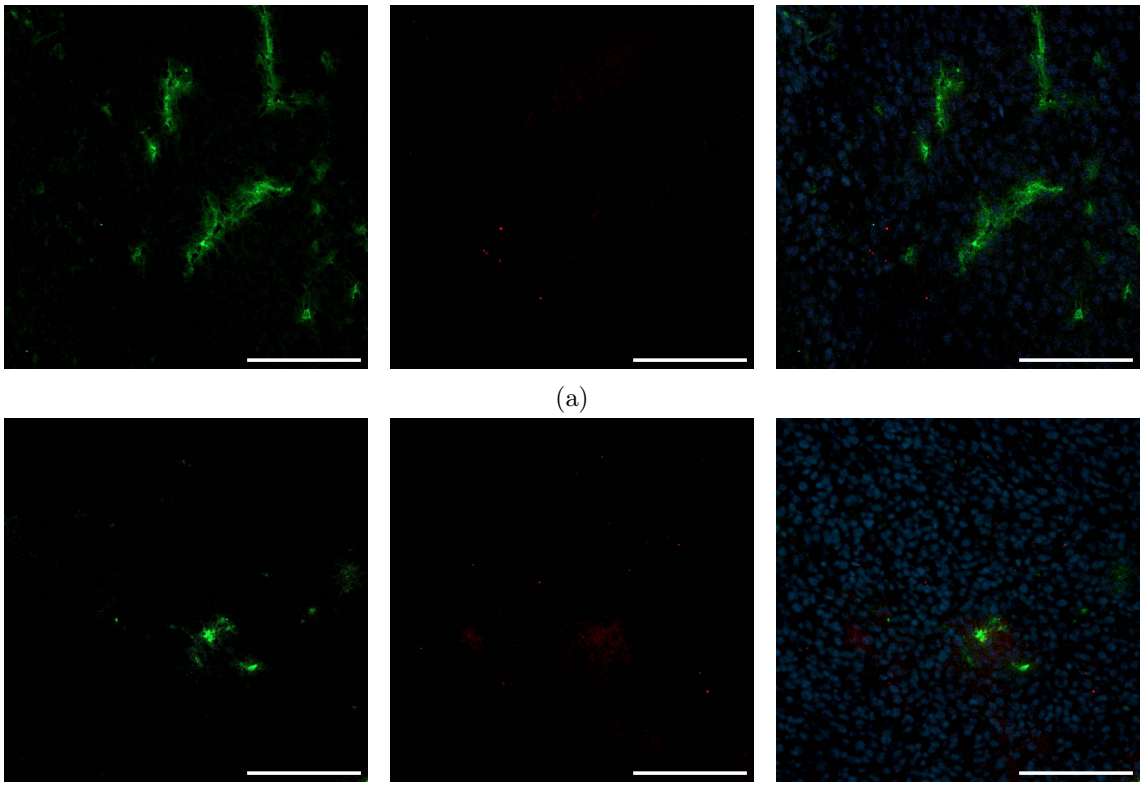

(a)

(b)

Figure 5.27: Two single images of blood vessels and NPs in a CT26 section. Blood vessels (green) and NPs (red) are shown separately, and a composite of the two channels where also the cell nuclei (blue) channel is added. Scale bars are 100 µm.

Examples of CLSM images of NPs, blood vessels and cell nuclei are presented in Figure 5.27. Nanoparticles labelled with Atto633 are red, blood vessels labelled with FITC-LEL are green, and cell nuclei labelled with DAPI are blue. The background, as well as brightness and contrast was adjusted to present the images to the reader. The displayed images are representatives of how most acquired images looked like. Visible NPs lumps are very few and small. Mostly, around 1-15 small NP lumps were detected per image.

5.4.3 Nanoparticle Extravasation Distance

The average NP extravasation distance (ED) in CT26 tumors are presented in Figure 5.28. Every point indicates the average ED for all images from one tumor, while the bar indicates the mean of all tumors in the experimental group. Error bars indicate the standard deviation. Control animals are green, while USMB treated animals are pink. Average ED is

presented for the total tumor, the core and the periphery of the tumor. Statistical analysis revealed no significant differences between the control and treated groups in the total, core or periphery. The average ED for each group in each tumor region varied between 41.8 and 63.4 µm. There was no significant difference detected between the regions within each animal group, for example between the core and periphery among control animals. There are several outliers, especially one animal from the treated group is far outside in the total tumor and core. Average NP ED distances are given in Table A.20 in Appendix A.

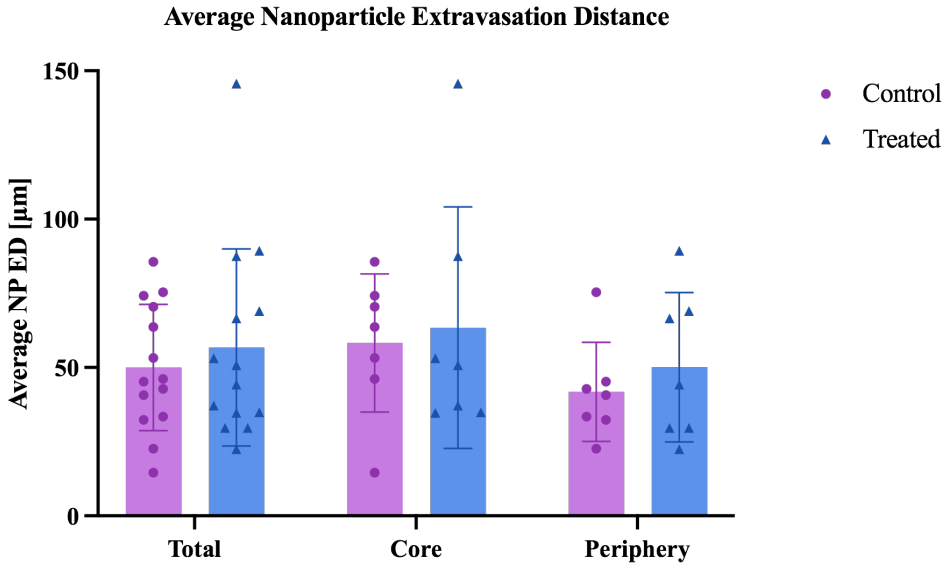

Figure 5.28: Average NP extravasation distance (NP ED) in control (green) and USMB treated (pink) CT26 tumors. The average NP ED for individual animals are represented by dots (control) and squares (treated). Bars indicate the mean of all animals, while the error bars indicate the standard deviation.

Microdistributions of extravasated NPs for the total, core and periphery are presented in Figure 5.29 (a), (b) and (c), respectively. Control and USMB treated animals are indicated by a pink and blue line. As described in Section 4.5.5, the extravasation distances on the x-axis were divided into bins of 10 µm. The y-axis displays the percentage of extravasated NPs. Raw values are presented in Table A.21 in Appendix A. For the total and periphery, the percentage of extravasated NPs decreases as ED increases. However, the variations are large and the curve is not consistently decreasing. In the core, the trend is weaker and the variations even larger. There were no significant differences between how far the NPs in the control and treated group had extravasated.

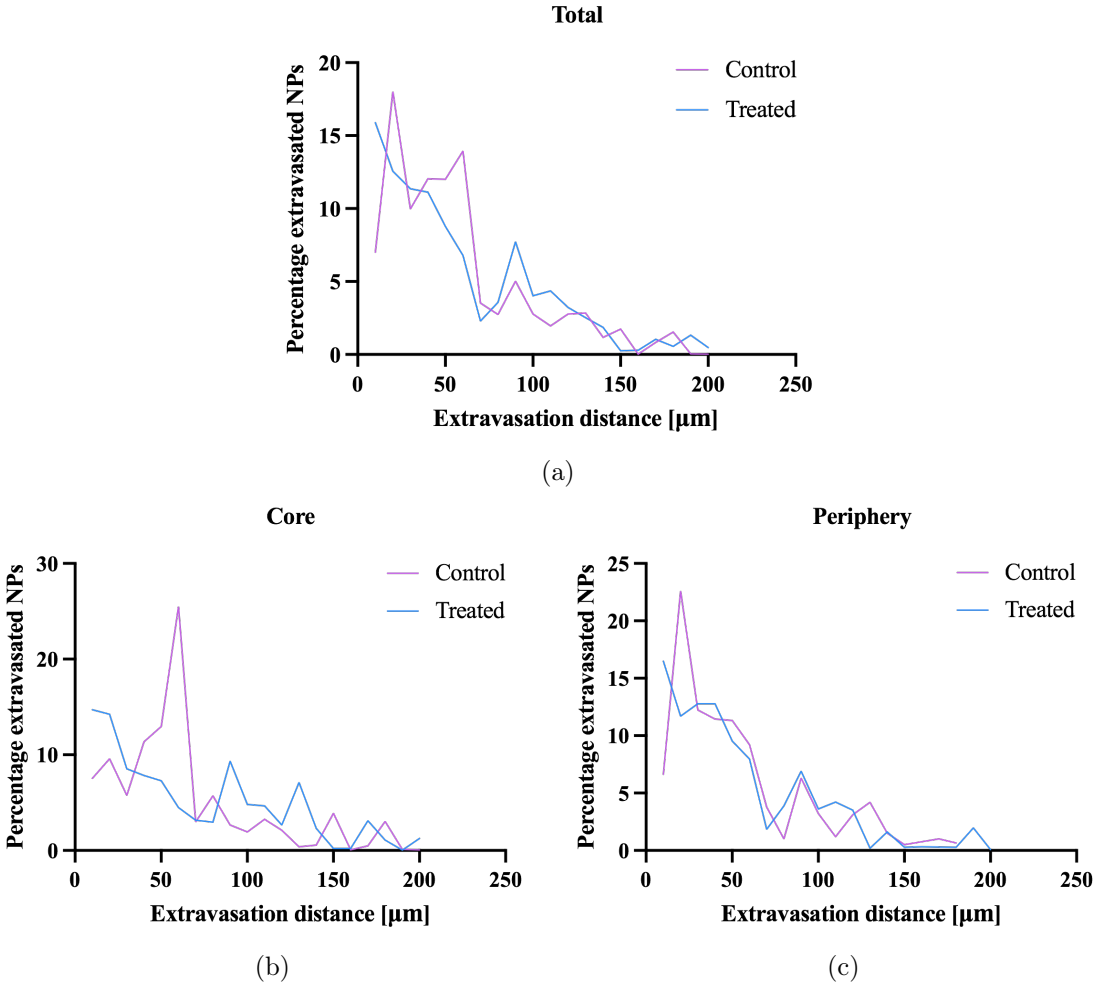

Figure 5.29: Distribution of non-colocalized NPs, i.e. extravasated NPs for (a) the total tumor, tumor (b) core and (c) periphery for control (pink) and treated (blue) animals. The ED on the x-axis in divided into bins of 10 µm. The y-axis shows the percentage of the total area of the extravasated NPs.

5.4.4 Relationship between Nanoparticle Uptake and CEUS data

Correlation between NP uptake data from Pearl and CEUS parameters was analyzed to investigate the relationship between NP uptake and perfusion. Correlation plots for peak enhancement (PE), wash-in area under the curve (WiAUC) and rise time (RT) versus mean fluorescence are presented in Figure 5.30 for CT26, Figure 5.31 for 4T1 and Figure 5.32 for KPC. Individual animals in the control and USMB treated group are indicated by dots and triangles, respectively. Correlation parameters are attached in Table A.32 for CT26, A.33 for 4T1 and A.34 for KPC in Appendix A.

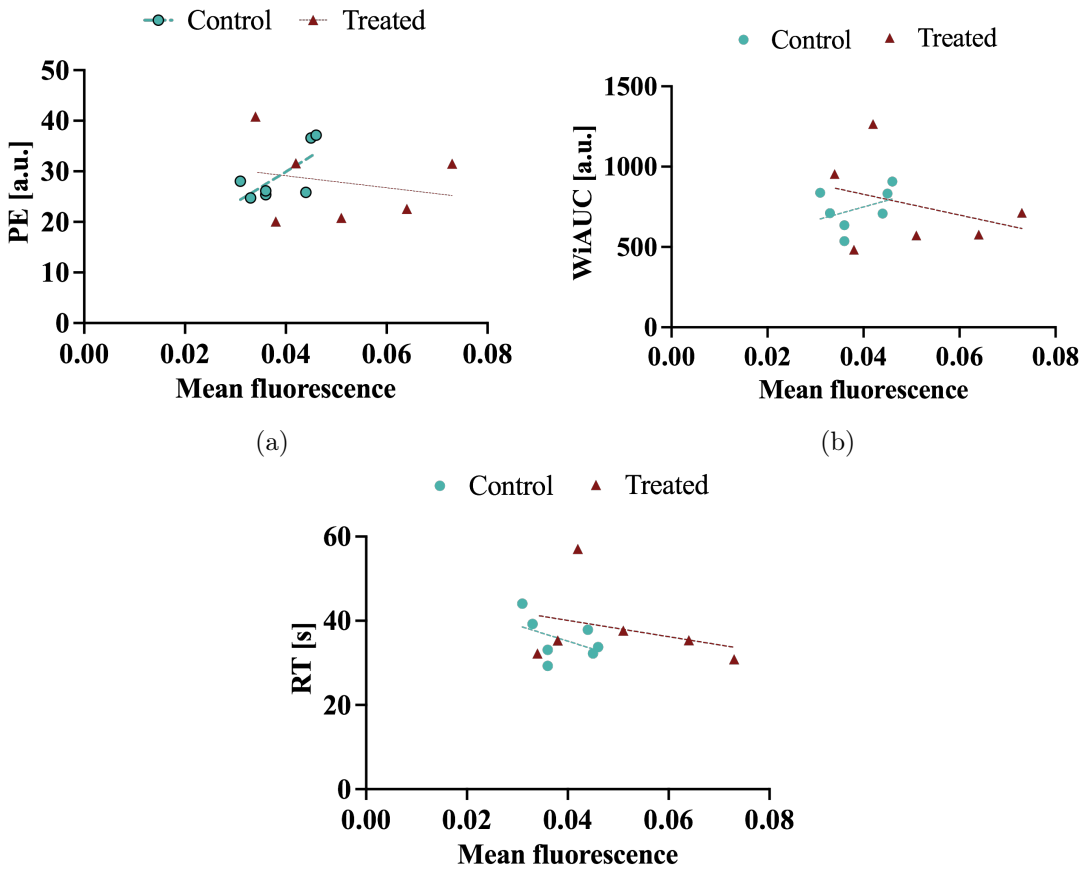

Figure 5.30: Correlation between mean fluorescence and CEUS parameters for CT26. Figure (a) displays PE, (b) WiAUC and (c) RT. Dots and triangles represents indvidual animals in the control and treated group, respectively. A dashed line indicates a insignificant correlation. Depending on the thickness of the line, the correlation is weak (thin line), moderate (medium line) or strong (thick line).

For CT26 tumors, the correlation between mean fluorescence and CEUS parameters was insignificant for all parameters and both groups. For PE, the correlation was strong and

positive for controls and weakly negative for treated animals. The correlation to WiAUC was moderate for both groups, positive for control and negative for treated animals. For RT, the correlation was moderate and negative for both groups.

Similarly, the correlation between mean fluorescence and CEUS parameters was also insignificant for all parameters and both groups for 4T1 tumors. For PE, the correlation was moderate, positive for controls and negative for treated animals. The correlation to WiAUC was moderate positive for controls, and negligible for treated animals. The correlation to RT was strong positive for both groups.

KPC tumors had a positive insignificant correlation between fluorescence and PE, moderate for controls and strong for treated animals. WiAUC showed a strong positive correlation for both groups, significant for controls and insignificant for treated animals. The correlation to RT was negligible for control and strong negative for treated animals.

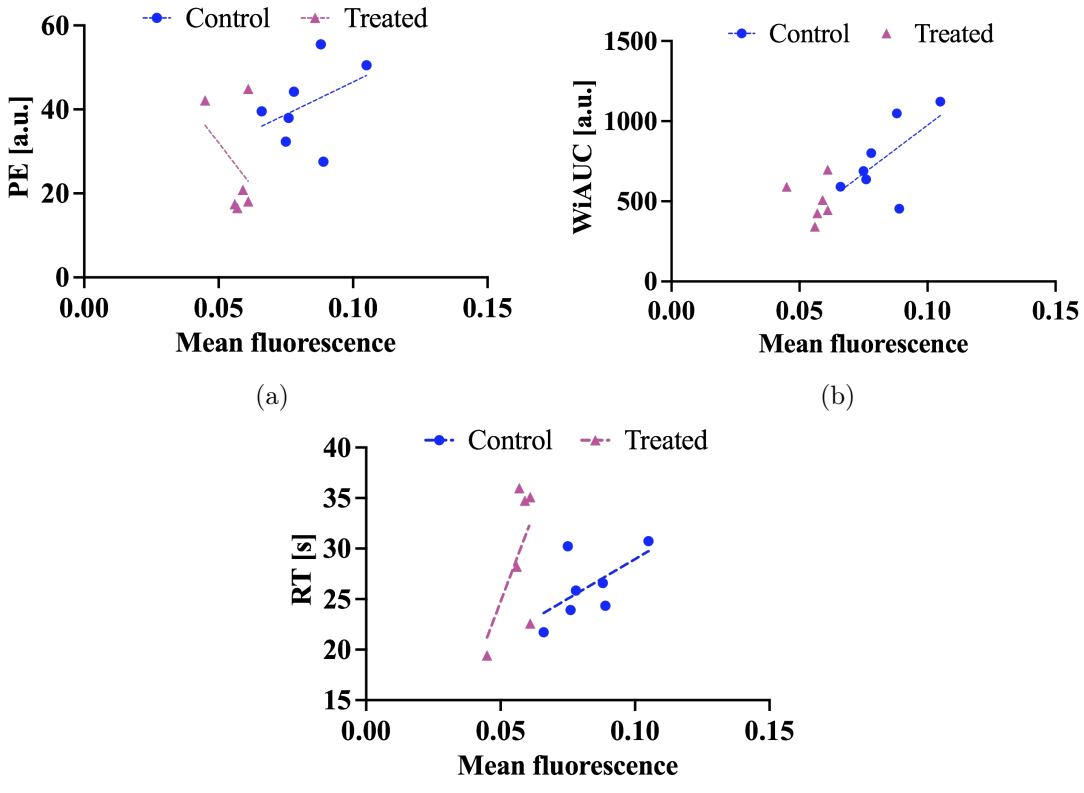

Figure 5.31: Correlation between mean fluorescence and CEUS parameters for 4T1. Figure (a) displays PE, (b) WiAUC and (c) RT. Dots and triangles represents indvidual animals in the control and treated group, respectively. A dashed line indicates a insignificant correlation. Depending on the thickness of the line, the correlation is weak (thin line), moderate (medium line) or strong (thick line).

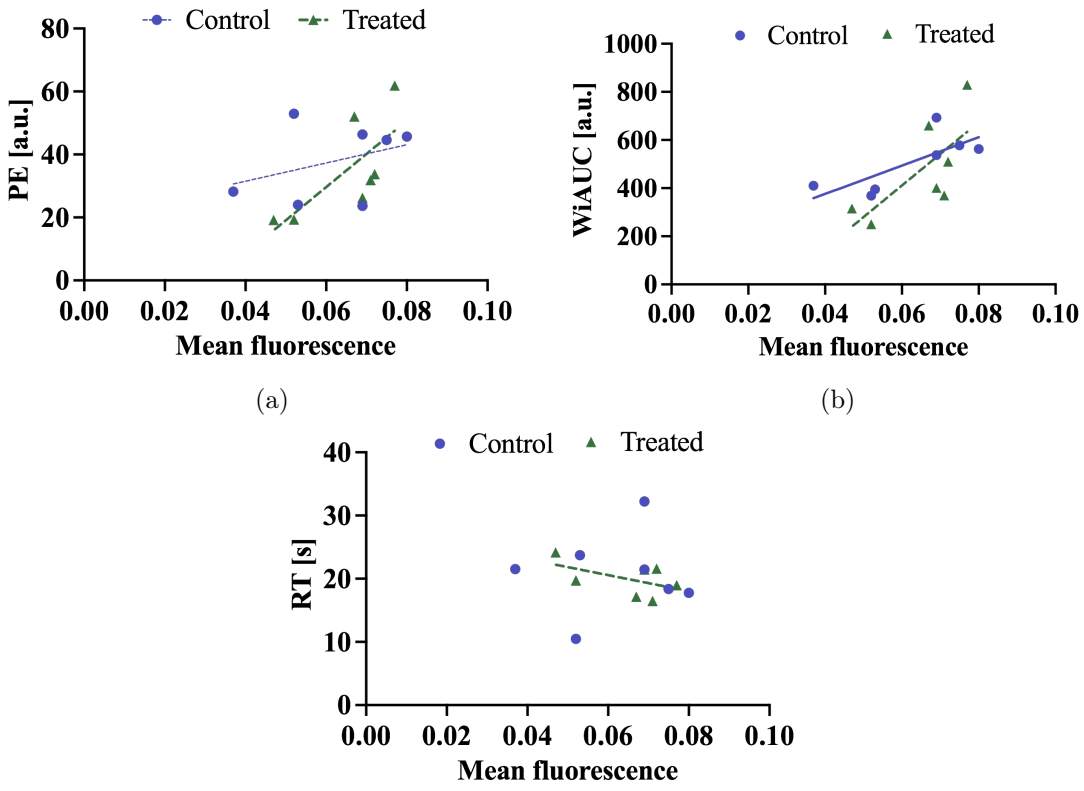

Figure 5.32: Correlation between mean fluorescence and CEUS parameters for KPC. Figure (a) displays PE, (b) WiAUC and (c) RT. Dots and triangles represents indvidual animals in the control and treated group, respectively. A dashed line indicates a insignificant correlation, while a solid line indicated a significant correlation. Depending on the thickness of the line, the correlation is weak (thin line), moderate (medium line) or strong (thick line).

Chapter 6

Discussion

6.1 CEUS

Assuming that KPC is hypovascular [46], CT26 is well vascularized [37], and 4T1 in between, differences between tumor models were smaller than expected from what was known about their vasculature characteristics. CEUS results are discussed based on what was known about the vasculature from before, and the findings from the CLSM perfusion analysis. As expected, CLSM analysis confirmed that total amount of blood vessels was higher for CT26 than 4T1. Also, fraction of perfused vessels was found to decrease with tumor weight, meaning that larger tumors are less perfused than small ones. This will be discussed more in detail later.

First of all, the size of the different tumors types is assumed to impact how comparable the data are. The average weight of CT26-1 was 0.54 g and that of CT26-2 was 1.1 g. 4T1 had an average weight of 0.5 g, while KPC were the smallest with an average weight of 0.1 g. CT26-1 and 4T1 were of similar weight and thus more comparable than CT26-2. KPC tumors were probably too small to provide a good basis of comparison.

Significantly higher WiAUC and RT was observed for both CT26-1 and CT26-2 than 4T1 and KPC. For WiAUC, this was expected based on the assumption that CT26 are the tumors with the highest degree of vascularization. RT and WiR are related, and reflects the blood flow velocity. Despite that WiR is only insignificantly higher for 4T1 and KPC than for CT26, higher RT and WiR might indicate a faster blood flow in 4T1 and KPC.

No statistical difference was found for PE. PE reflects blood perfusion, and was thus expected to be more different. Low PE values are correlated to hypoxia, applicable for

KPC tumors, whereas high PE values are correlated to increased perfusion and/or tumor angiogenesis [71], assumed to be the case for CT26 tumors. Even if not significant, CT26-1 had higher PE than 4T1, which agrees with the vascularization of CT26 tumors. On the contrary, average PE is for example higher for KPC and 4T1 than CT26-2. Recalling that CT26-2 were double the size of CT26-1, this result can be explained by the negative relationship between perfusion and tumor weight. Large intra-group variability is present for all tumor models, contributing to lack of significant differences.

Further differences were observed between the two groups of CT26 animals. For CT26-1, the average of all presented CEUS parameters (PE, RT, WiAUC and RT) were higher than for the CT26-2. Statistical analysis did not reveal significant differences. However, the trend of higher PE in CT26-1 than CT26-2 was stronger than initially expected ($p=0.15$), as one would assume similar values for the same tumor type. Correlation between PE and tumor weight was significant and negative. Looking at the size of the tumors, the mean weight of CT26-2 tumors was the double of CT26-1 tumors, which explains the differences and agree with the negative correlation between PE and tumor weight and between CLSM perfusion parameters and tumor weight. To conclude based on the discussed CEUS parameters for the all three models, CT26 appears to have more perfused vessels but slower blood flow than 4T1 and KPC tumors.

Regarding differences between CEUS parameters in the tumor periphery and center, a trend of lower values for PE, WiAUC and WiR seemed to be present for all tumor models. More fragile blood vessels in the tumor center than the periphery has been demonstrated [30]. Rapid tumor growth increases solid stress in the tumor interior, and can cause development of fragile central tumor blood vessels and eventually cause vessel collapse. This can explain a recurring trend of low CEUS parameters in the tumor centers.

Observing the CEUS videos with the naked eye, the tumors do not appear as poorly perfused. This does not correspond with the low fractions of perfused blood vessels indicated by the CLSM analysis. US does not provide well resoluted images. Poor resolution might entail visualisation of only large blood vessels in CEUS videos, whereas smaller capillaries are only visible in highly resoluted CLSM images.

6.2 Effect of USMB Treatment on Tumor Perfusion

Altogether, the obtained results agree with results found in previous studies investigating the effect of USMB on tumor perfusion. The research group to which this project also belongs to, has now observed reduced perfusion as a consequence of US and Sonovue treatment in four murine tumor models; CT26, OHS, 4T1 and KPC. In the following sections, this will be discussed in more detail, as well as the compatibility between CLSM and CEUS perfusion measurements.

6.2.1 Effect of US and Sonovue on Tumor Perfusion

Perfusion in US and Sonovue treated CT26 and 4T1 tumors was significantly reduced in all tumor regions, except for the center of 4T1. For both CT26 and 4T1, the relative change in fraction of perfused vessels was larger in the center than the periphery. Furthermore, controls in both the Sonovue and ACT experiment exhibited a trend of lower fraction of functional blood vessels in the center compared to the periphery. In the US and Sonovue experiment, the average fraction of perfused vessels in the control group was 29% higher in the periphery compared to the center for CT26, and 111% higher in the periphery for 4T1. Tumors generally are less perfused in the center than periphery [30]. Rapid tumor growth induces elevated solid stress in the tumor interior, contributing to fragile vasculature in the tumor center[72]. The magnitude of this solid stress can be sufficient to cause vascular shutdown, and can explain the low fraction of functional blood vessels in the tumor center even without USMB treatment. A plausible cause of the reduced perfusion in controls versus treated tumors, is the USMB inducing collapse of blood vessels by rupturing the vascular membrane. Upon the applied mechanical stress from USMB treatment, it is likely that fragile tumor blood vessels will collapse easier than normal vasculature. Several studies suggest reduced tumor perfusion to be a result of disruption of blood vessels caused by USMB [11].

Chemotherapy combined with US and Sonovue treatment on CT26 murine tumors has been studied previously [73]. Results from the previous paper demonstrated enhanced delivery of a liposomal chemotherapeutic drug to the tumor. Furthermore, the results indicated reduced perfusion, blood vessel disruption and inhibited tumor growth. These findings agree with the results for CT26 tumors in this thesis, both in terms of reduced perfusion and enhanced uptake of liposomes in Sonovue and US treated tumors.

The effect of USMB with Sonovue and MI=0.5 on perfusion in 4T1 tumors was previously investigated by Årseth [70]. In the previous study, the animal was euthanized one hour

after treatment instead of 5 min after treatment, which was the case in this thesis. A trend towards reduced fraction of functional blood vessels in treated animals was observed, but the difference was not significant. The experiment carried out in this thesis followed up and confirmed the trend, showing significant reduction of perfused vessels in treated tumors. US and Sonovue treatment of 4T1 tumors with a higher MI of 0.8 was investigated in a previous study by Rix et al [74]. Also, this study demonstrated a significant reduction of perfused blood vessels in USMB treated tumors.

The effect of US and Sonovue on perfusion in KPC tumors was previously evaluated [75] [76], and is the reason why KPC was not included in this thesis. The experimental setup was similar to that of this thesis, and the utilized US was MI = 0.5. For KPC, a trend of reduced perfusion in USMB treated animals was observed, but the reduction was not significant.

The effect of USMB with Sonovue and MI=0.5 has also been investigated in human osteosarcoma (OHS) tumors [77]. For animals euthanized immediately after treatment, the treated group had a significant reduction of perfused tumor vessels compared to the control group. However, 24 post treatment, a trend towards higher fraction of perfused vessels in the control group than the treated group. Hence, the the effect of reduced perfusion was not sustained over time. As CT26 tumors, OHS tumors are characterized as well vascularized. An interesting continuation would be to investigate whether the effect of reduced perfusion in CT26 and 4T1 tumors persists after treatment, or if the behaviour is similar to that of OHS.

An alternative explanation of reduced perfusion as a consequence of USMB is that mechanical stress causes activation and aggregation of platelets upon ruptures in the endothelial wall [78] [79]. The papers suggest that the platelets block blood flow at the rupture site.

Antivascular effects induced by USMB has alone been suggested as a treatment strategy [72][80][81]. USMB may induce vascular damage and collapse and reduce blood flow, ensuing inhibited tumor growth [82]. In the case of USMB as antitumor treatment, reduced perfusion would be the desired effect of the treatment. As discussed previously, the tumor periphery is often less affected by USMB treatment. Thus, the peripheral vessels can facilitate revascularization and re-growth of the tumor. This "vascular rebound effect" constitute a limitation of the treatment strategy, counteracting the antitumor effects induced by USMB. Recently, the combined use of USMB with chemotherapy has exhibited more promising results compared to USMB as a monotherapy.

6.2.2 Effect of US and ACT on Tumor Perfusion

Fraction of perfused tumor blood vessels was not significantly reduced by US and ACT treatment of CT26 tumors. However, a weak trend of reduction was observed in treated animals versus controls. In the same manner as tumors included in the Sonovue experiment, the tumor center appears as less perfused than the periphery. As expected, average fraction of perfused vessels in control CT26 animals in the ACT and Sonovue studies was similar. Previous evaluation of the effect of ACT on perfusion in KPC tumors demonstrated no significant difference between control and treated animals [83].

Opposed to what was demostrated for Sonovue, no perfusion reduction was demonstrated in US and ACT treated CT26 tumors. There are several possible explanations to why US and ACT did not reduce perfusion. First of all, the US parameters used for Sonovue and ACT treatments are optimized for each bubble type. For the Sonovue treatment, the US had higher pressure and longer pulses, and MI was 0.5. The MI for ACT treatment was 0.2 both during activation and enhancement. Lower MI imply lower probability of inertial cavitation, less mechanical forces on the blood vessels, which prevents the vessels from ruptures and collapse. Hence, these US parameters may not be sufficient to reduce perfusion.

ACT has been suggested to overcome important shortcomings of MBs as Sonovue, such as short circulation time and small size [61]. The diameter for ACT bubbles is 20-30 µm versus 2.5 µm in average for Sonovue. ACT transiently lodge the capillaries for 5-10 min, while Sonovue has a half life of 1 minute. Even though ACT bubbles are large and the contact area between the bubble and the blood vessel is significantly improved compared to Sonovue, an important aspect to consider is that only a fraction of injected microclusters are actually activated. Only 1% of the tumor capillaries are lodged by ACT bubbles [84].

6.2.3 Relationship between Tumor Vasculature Parameters

For CT26 tumors, USMB treated animals demonstrated a positive correlation, except for the periphery of ACT treated animals. Controls in the Sonovue experiment also had a positive correlation, while controls in the ACT experiment had a moderate to negligible negative correlation. The correlation indicates that the fraction of functional blood vessels increase with total amount of BVs, which was expected. Opposed to CT26, 4T1 tumors revealed a insignificant negative relationship between amount of all blood vessels and perfused vessels for both control and treated animals. Such varying correlations as demonstrated for CT26 and 4T1 emphasize the importance of characterizing different tu-

mor models. A significant correlation for one tumor model is not necessarily transferable to another model.

Regardless of whether Sonovue or ACT bubbles were used for USMB treatment, both CT26 and 4T1 tumors demonstrated a negative correlation between tumor weight and fraction of perfused vessels. Sonovue and US treated CT26 animals stand out, exhibiting a strong significant correlation. One exception was USMB treated 4T1 tumors, where the correlation was weak or negligible. Solid stress and IFP increase with tumor size [30], and can explain less collapsing and in small tumors. Hence, fraction of perfused vessels decrease with increasing weight, leading to a negative correlation. This implies that USMB treatment might be beneficial for small tumors rather than large ones, since the distribution of MBs is dependent on the presence of a functional vasculature.

6.2.4 Relationship between Tumor Vasculature Parameters and CEUS

One objective of this thesis was to explore the potential of CEUS as screening method to reveal responders to USMB. Previously, CEUS has been proven as a useful tool to evaluate efficacy of antangiogenic treatments in humans [85] [86]. The aim of establishing a relationship between tumor vasculature parameters with CEUS parameters was to investigate the potential of CEUS stratification tool to predict the utility of USMB, based on the assumption that the amount of blood vessels is important to benefit from the treatment. If the CLSM and CEUS perfusion measurement are correlated, it suggests the potential of CEUS as a non-invasive technique for perfusion measurement. For this correlation analysis, an important notice is that the cross section analyzed is not the exact same for blood vessels and CEUS, as plane imaged with CEUS is perpendicular to the one CLSM imaged. Also, the time of measurement was different.

Since CT26-1 tumors were also CEUS imaged, this enabled establishment of the relationship between the parameters. PE had a moderate and positive correlation to fraction of perfused vessels, an thus the most relevant biomarker for potential patient stratification. For RT, WiAUC and WiR, the correlation was weak or negligible. Thus, no conclusions can be drawn regarding their relevance as biomarkers. Uncertainties in this correlation analysis include that the data are measured at two different time points, and that data represent two different cross sections in the tumor. As previously mentioned, it is also not certain that the same vessels are visualized by CEUS and CLSM imaging due to the different resolution.

6.3 Effect of USMB on Uptake and Microdistribution of Liposomes

The effect of USMB on uptake of NPs was investigated in CT26, 4T1 and KPC tumors. Results demonstrated that different tumor models respond differently to USMB treatment. For CT26 tumors ex vivo, uptake of NPs was significantly higher for USMB treated tumors than controls. Conversely, the opposite was observed in the case of 4T1. A possible explanation is that in 4T1 tumors, the EPR effect is stronger than the mechanical effect from USMB. Comparing the mean fluorescence of the control groups gives an indicator on the strength of the EPR effect. The mean fluorescence of all 4T1 control animals is twice that of CT26 controls, suggesting stronger EPR effect in 4T1. For 4T1, it seems like the EPR effect is hindered by reduced perfusion caused by USMB treatment. On the other hand, the weaker EPR effect in CT26 combined with USMB treatment enhance uptake of NPs, despite that USMB was found to reduce tumor perfusion significantly in the experiments performed in this thesis. As mentioned, the effect of US and Sonovue has been studied in KPC tumors previously [75], observing a trend but no significant reduction. For KPC, no significant difference in liposomal uptake was observed in control versus USMB treated tumors, which would be expected presuming unaltered perfusion.

When it comes to average NP extravasation distance, there were no significant differences neither in average extravasation or between the total, core and periphery of the tumor. In case of the distribution of extravasated NPs, no difference between control and USMB treated animals here either. A fellow master student had the same object of studying uptake and distribution of NPs in the same tumors that were involved in this thesis [87], specifically focusing at the adjacent section to that analyzed in this thesis. Results did not show significant differences between control and treated tumors. Neither did Wesche find that USMB treatment changed the NP extravasation distance. However, the distribution of extravasated NPs revealed a higher fraction of NPs closer to their originating blood vessel than what was found in this thesis. Hence, two analyses of the same tumors strengthen the results showing that NP ED in CT26 tumors was not affected by USMB treatment.

To label perfused blood vessels, FITC-LEL was injected 24 h after treatment. During the 24 hours, vessels might have collapsed. Thus, when deciding which vessel a NP has extravasated from, it is not certain that the particular vessel still exists. Another error source is that CLSM images only show a 8 µm thick section of the tumor. As a consequence, a NP in the imaged plane might not originate from the closest vessel in the imaged plane. Hence, the NP could be assumed to have extravasated from the wrong vessel. In particular, this could possibly explain why the distribution plots do not show the highest percentage

of NPs at a close distance from the blood vessel.

For some tumors, it was challenging to find blood vessels and NPs at all. Especially, some tumors had very few blood vessels in the core. Therefore, the number of NPs observed in some tumors are much lower for some tumors than others. For example, some images would contain only one NP lump, while the image with most NPs had 58 NP lumps. If this applies to several images, large variations in the amount of data accumulate. Time vs. tumor uptake curves from Pearl imaging revealed a shorter circulation time of the NPs than expected, and explains the low amount of particles observed in tumors ex vivo.

6.3.1 Relationship between CEUS and Liposomal Uptake in Tumors

The purpose of correlating CEUS parameters with NP uptake was to uncover biomarkers and evaluate if CEUS imaging can be utilized to predict which tumors will benefit from USMB treatment to improve drug delivery. Also in the case of this correlation analysis, the cross section CEUS imaged is perpendicular to the CLSM imaged cross section, introducing a limitation of the comparison. Supposed that any of the CEUS parameters were significantly correlated to tumor uptake, it would be a relevant biomarker to predict responders to USMB. Since CEUS was performed two days prior to euthanazia and resection of tumors, the time difference between measurements introduce a limitation of the correlation. CEUS imaging post treatment would have improved comparability of the data, and may reveal biomarkers more clearly.

Considering the CEUS parameters and uptake data for control animals, only PE and WiAUC has a similar positive correlation for both CT26, 4T1 and KPC animals. However, the correlations are not significant except for WiAUC for KPC. This weakly suggests that PE and WiAUC could be possible biomarkers to assess the usefulness of USMB. Correlation between CEUS parameters and NP uptake for treated animals did not resemble that of the control group. To conclude, none of the correlations were sufficient in order to designate biomarkers for patient stratification.

6.4 Implications and Clinical Relevance of USMB for Drug Delivery

A crucial question to ask is whether the observed effects of USMB on perfusion and NP uptake in murine tumor models are transferable to human cancer. One preclinical paper performed US and Sonovue treatment with MI 0.8 on both human and murine breast cancers [74]. Perfusion was not significantly effected in TNBC in humans, and the response to chemotherapy was lower for USMB treated tumors. On the contrary, USMB treated murine 4T1 tumors underwent a significant reduction of perfused blood vessels. Possible explanations of stronger vascular response in murine 4T1 tumors than in human TNBC tumors concluded by the authors are higher vascular immaturity and lower stromal stabilization. The findings emphasize that effects from USMB treatment vary in mice and humans.

The different tumor types investigated in the experiments of this thesis responded differently to USMB treatment both when it comes to perfusion and NP uptake. Results proved the importance of characterizing the effects of USMB for different tumor models. Characterization of murine tumor models provides an insight into which patients that will be responders to USMB, and brings USMB treatment of relevant cancers a step closer to clinical trials.

6.5 Future Work

A major limitation of the analysis performed in this thesis is the fact that only one section in each tumor is analyzed when it comes to CLSM images. Despite this, there is a considerable amount of blood vessels within one section, which is why one section was assumed to provide sufficient statistics. However, to obtain more representative data, several sections per tumor should be analyzed. Varying tumor size constitutes another limitation, with CT26 being very large, KPC very small and 4T1 in between. If the tumors were more equally sized, comparison of data would become easier.

Another suggestion for the future when it comes to perfusion, is to assess how perfusion is affected also after some time, not only right after treatment. As mentioned previously in the discussion, perfusion could for example be measured in animals euthanized 24 h post treatment. This would require a high number experimental animals.

Regarding CEUS, the parameters were acquired from the cross section of the tumor.

VevoLAB provides a tool to quantify the percentage agent in 3D videos. This would provide an indicator of the perfusion in the entire tumor, not only the cross section. In the CEUS experiment, 3D videos were acquired pre and post MB injection, but were not analyzed. While wash-in parameters are measured in VevoCQ, wash-out parameters are not provided. Wash-out parameters could be useful to observe how the outflow behavior of MBs. A possible objective would be to develop a method to assess wash-out parameters.

One can speculate about how necrosis and perfusion are related. Correlating necrosis to fraction of perfused blood vessels would be useful in order to investigate this. The amount of necrosis could be quantified by image analysis of HES-stained tumor sections. In addition, poorly perfused areas can be identified in CEUS videos. These areas could be quantified. Necrotic areas and correlated to perfusion parameters would establish a relationship between necrosis and perfusion.

Chapter 7

Conclusion

The objectives of this thesis was to study the effect of USMB on perfusion and on liposomal uptake and microdistribution in murine tumor models, CEUS was performed in order to characterize perfusion parameters in murine tumor models, with the aim of exploring whether CEUS can be a tool for patient stratification, and to assess the compatibility between CLSM and CEUS as methods for perfusion measurement.

To summarize, the findings underlined the importance of investigating the effect of USMB in various tumor models, since the response was demonstrated to vary. Results revealed that USMB with Sonovue MBs significantly reduced perfusion in CT26 and 4T1 tumors, while ACT treatment of CT26 tumors did not reduce perfusion significantly. This is likely attributed to longer pulses or higher MI used for US and Sonovue treatment compared to the ACT experiment, or that the number of ACT bubbles in the vasculature is lower than the number of Sonovue. US and Sonovue treatment improved tumor uptake of NPs in CT26 tumors significantly, whereas tumor uptake was significantly reduced for 4T1 animals. This may be attributed to a stronger EPR effect in 4T1 tumors than in CT26 tumors. To translate the findings into possible clinical implications, the results suggest that patients with colorectal cancer might benefit from USMB treatment. Correlation between CEUS parameters and NP uptake did not reveal clear biomarkers for USMB patient stratification, while correlation between CLSM and CEUS perfusion parameters revealed PE as possible biomarker.

Suggestions for future work include analysis of several sections per tumor, correlating perfusion and necrosis, and to assess CEUS wash-out parameters.

Bibliography

[1] World Health Organization. https://www.who.int/health-topics/cancer. Accessed 2023-06-28.

[2] Global Cancer Observatory: Cancer Today. https://gco.iarc.fr/today/. Accessed 2023-06-28.

[3] American Cancer Society. https://www.cancer.org/cancer/risk-prevention/understanding-cancer-risk/lifetime-probability-of-developing-or-dying-from-cancer.html. Accessed 2023-06-28.

[4] Stefan Wilhelm et al. "Analysis of nanoparticle delivery to tumours". In: *Nat. Rev. Mater.* 1.16014 (Apr. 2016), pp. 97–111.

[5] Qin Dai et al. "Quantifying the ligand-coated nanoparticle delivery to cancer cells in solid tumors". In: *ACS nano* 12.8 (2018), pp. 8423–8435.

[6] Marieke Olsman et al. "Ultrasound-mediated delivery enhances therapeutic efficacy of MMP sensitive liposomes". In: *Journal of controlled release* 325 (2020), pp. 121–134.

[7] Benjamin Theek et al. "Sonoporation enhances liposome accumulation and penetration in tumors with low EPR". In: *Journal of controlled release* 231 (2016), pp. 77–85.

[8] Georg Dimcevski et al. "A human clinical trial using ultrasound and microbubbles to enhance gemcitabine treatment of inoperable pancreatic cancer". In: *Journal of Controlled Release* 243 (2016), pp. 172–181.

[9] Spiros Kotopoulis et al. "Sonoporation-enhanced chemotherapy significantly reduces primary tumour burden in an orthotopic pancreatic cancer xenograft". In: *Molecular imaging and biology* 16 (2014), pp. 53–62.

[10] Ayache Bouakaz, Aya Zeghimi, and Alexander A Doinikov. "Sonoporation: Concept and mechanisms". In: *Therapeutic Ultrasound* (2016), pp. 175–189.

[11] Sofie Snipstad et al. “Ultrasound and microbubbles to beat barriers in tumors: Improving delivery of nanomedicine”. en. In: *Adv. Drug Deliv. Rev.* 177.113847 (Oct. 2021), p. 113847.

[12] Andrea Berge Kastellet. “Effect of Ultrasound-Stimulated Microbubble Therapy on Vasculature in Murine Colon Cancer Tumors”. 2023.

[13] National Cancer Institute. https://www.cancer.gov/about-cancer/understanding/statistics. Accessed 2023-06-20.

[14] Sasi S Senga and Richard P Grose. “Hallmarks of cancer-the new testament”. en. In: *Open Biol.* 11.1 (Jan. 2021), p. 200358.

[15] Qin Dai et al. “Quantifying the ligand-coated nanoparticle delivery to cancer cells in solid tumors”. en. In: *ACS Nano* 12.8 (Aug. 2018), pp. 8423–8435.

[16] Dan Peer et al. “Nanocarriers as an emerging platform for cancer therapy”. In: *Nature nanotechnology* 2.12 (2007), pp. 751–760.

[17] Hans-Peter Gerber, Peter D Senter, and Iqbal S Grewal. “Antibody drug-conjugates targeting the tumor vasculature: current and future developments”. In: *MAbs*. Vol. 1. 3. Taylor & Francis. 2009, pp. 247–253.

[18] Fabienne Danhier, Olivier Feron, and Véronique Préat. “To exploit the tumor microenvironment: Passive and active tumor targeting of nanocarriers for anti-cancer drug delivery”. en. In: *J. Control. Release* 148.2 (Dec. 2010), pp. 135–146.

[19] Achilleas D Theocharis et al. “Extracellular matrix structure”. In: *Advanced drug delivery reviews* 97 (2016), pp. 4–27.

[20] Erik Henke, Rajender Nandigama, and Süleyman Ergün. “Extracellular matrix in the tumor microenvironment and its impact on cancer therapy”. en. In: *Front. Mol. Biosci.* 6 (2019), p. 160.

[21] Zongmin Zhao et al. “Targeting strategies for tissue-specific drug delivery”. en. In: *Cell* 181.1 (Apr. 2020), pp. 151–167.

[22] Dan Peer et al. “Nanocarriers as an emerging platform for cancer therapy”. en. In: *Nat. Nanotechnol.* 2.12 (Dec. 2007), pp. 751–760.

[23] Remon Bazak et al. “Cancer active targeting by nanoparticles: a comprehensive review of literature”. en. In: *J. Cancer Res. Clin. Oncol.* 141.5 (May 2015), pp. 769–784.

[24] Yechezkel Barenholz. “Liposome application: problems and prospects”. In: *Current opinion in colloid & interface science* 6.1 (2001), pp. 66–77.

[25] Alberto Gabizon et al. “Tumor cell targeting of liposome-entrapped drugs with phospholipid-anchored folic acid–PEG conjugates”. In: *Advanced drug delivery reviews* 56.8 (2004), pp. 1177–1192.

[26] Simona Mura, Julien Nicolas, and Patrick Couvreur. “Stimuli-responsive nanocarriers for drug delivery”. In: *Nature materials* 12.11 (2013), pp. 991–1003.

[27] M K Pugsley and R Tabrizchi. “The vascular system. An overview of structure and function”. en. In: *J. Pharmacol. Toxicol. Methods* 44.2 (Sept. 2000), pp. 333–340.

[28] Ivan Bačić et al. “Tumor angiogenesis as an important prognostic factor in advanced non-small cell lung cancer (Stage IIIA)”. en. In: *Oncol. Lett.* 15.2 (Feb. 2018), pp. 2335–2339.

[29] Jamal Majidpoor and Keywan Mortezaee. “Angiogenesis as a hallmark of solid tumors - clinical perspectives”. en. In: *Cell. Oncol.* 44.4 (Aug. 2021), pp. 715–737.

[30] Triantafyllos Stylianopoulos et al. “Coevolution of Solid Stress and Interstitial Fluid Pressure in Tumors During Progression: Implications for Vascular CollapseEvolution of Solid and Fluid Stresses in Tumors”. In: *Cancer research* 73.13 (2013), pp. 3833–3841.

[31] Brian Olson et al. “Mouse Models for Cancer Immunotherapy ResearchCoclinical Mouse Models for Cancer Immunotherapy”. In: *Cancer discovery* 8.11 (2018), pp. 1358–1365.

[32] Edward A Sausville and Angelika M Burger. “Contributions of human tumor xenografts to anticancer drug development”. In: *Cancer research* 66.7 (2006), pp. 3351–3354.

[33] Kelly Kersten et al. “Genetically engineered mouse models in oncology research and cancer medicine”. In: *EMBO molecular medicine* 9.2 (2017), pp. 137–153.

[34] Maryland Franklin. https://drugdevelopment.labcorp.com/industry-solutions/oncology/preclinical/tumor-spotlights/ct26-murine-colon-carcinoma.html. 2016.

[35] John C Castle et al. “Immunomic, genomic and transcriptomic characterization of CT26 colorectal carcinoma”. en. In: *BMC Genomics* 15 (Mar. 2014), p. 190.

[36] Anna Orlova et al. “Raster-scan optoacoustic angiography of blood vessel development in colon cancer models”. en. In: *Photoacoustics* 13 (Mar. 2019), pp. 25–32.

[37] Johanne Seguin et al. “Evaluation of nonradiative clinical imaging techniques for the longitudinal assessment of tumour growth in Murine CT26 colon carcinoma”. en. In: *Int. J. Mol. Imaging* 2013 (July 2013), p. 983534.

[38] National Cancer Institute. https://www.cancer.gov/types/breast. Accessed: 2023-06-05.

[39] Carey K Anders and Lisa A Carey. "Biology, metastatic patterns, and treatment of patients with triple-negative breast cancer". en. In: *Clin. Breast Cancer* 9 Suppl 2 (June 2009), S73–81.

[40] Barbara Schrörs et al. "Multi-omics characterization of the 4T1 Murine mammary gland tumor model". en. In: *Front. Oncol.* 10 (July 2020), p. 1195.

[41] Alexander M Saucedo et al. "Multimodal imaging of the tumor microenvironment and biological responses to immune therapy". en. In: *Biomed. Microdevices* 20.4 (Dec. 2018), p. 105.

[42] Jun Ushio et al. "Pancreatic ductal adenocarcinoma: Epidemiology and risk factors". en. In: *Diagnostics (Basel)* 11.3 (Mar. 2021), p. 562.

[43] Panagiotis Sarantis et al. "Pancreatic ductal adenocarcinoma: Treatment hurdles, tumor microenvironment and immunotherapy". In: *World journal of gastrointestinal oncology* 12.2 (2020), p. 173.

[44] Ximbio. https://ximbio.com/reagent/153474/kpc-cell-line-c57bl6-genetic-background. Accessed: 2023-05-14.

[45] Jae W Lee et al. "Genetically engineered mouse models of pancreatic cancer: The KPC model (LSL-kras(G12D/+) ;LSL-Trp53(R172H/+) ;Pdx-1-cre), its variants, and their application in immuno-oncology drug discovery". In: *Curr. Protoc. Pharmacol.* 73.1 (June 2016), pp. 14.39.1–14.39.20.

[46] Michael A Jacobetz et al. "Hyaluronan impairs vascular function and drug delivery in a mouse model of pancreatic cancer". en. In: *Gut* 62.1 (Jan. 2013), pp. 112–120.

[47] Raefa Abou Khouzam et al. "Hypoxia, a targetable culprit to counter pancreatic cancer resistance to therapy". In: *Cancers* 15.4 (2023), p. 1235.

[48] Douglas L Miller et al. "Overview of therapeutic ultrasound applications and safety considerations". In: *Journal of ultrasound in medicine* 31.4 (2012), pp. 623–634.

[49] Taner Şen, Omaç Tüfekçioğlu, and Yavuzer Koza. "Mechanical index". In: *Anatolian journal of cardiology* 15.4 (2015), p. 334.

[50] *Vevo CQ User Manual*. Fujifilm VisualSonics.

[51] Richard J Browning et al. "Prospects for enhancement of targeted radionuclide therapy of cancer using ultrasound". en. In: *J. Labelled Comp. Radiopharm.* 57.4 (Apr. 2014), pp. 279–284.

[52] Zahra Izadifar, Paul Babyn, and Dean Chapman. "Mechanical and biological effects of ultrasound: A review of present knowledge". en. In: *Ultrasound Med. Biol.* 43.6 (June 2017), pp. 1085–1104.

[53] Sofie Snipstad et al. "Sonopermeation to improve drug delivery to tumors: from fundamental understanding to clinical translation". en. In: *Expert Opin. Drug Deliv.* 15.12 (Dec. 2018), pp. 1249–1261.

[54] David E Goertz et al. "Antitumor effects of combining docetaxel (taxotere) with the antivascular action of ultrasound stimulated microbubbles". en. In: *PLoS One* 7.12 (Dec. 2012), e52307.

[55] J Todd Belcik et al. "Augmentation of limb perfusion and reversal of tissue ischemia produced by ultrasound-mediated microbubble cavitation". In: *Circulation: Cardiovascular Imaging* 8.4 (2015), e002979.

[56] J Todd Belcik et al. "Augmentation of muscle blood flow by ultrasound cavitation is mediated by ATP and purinergic signaling". In: *Circulation* 135.13 (2017), pp. 1240–1252.

[57] Caitlin W Burke et al. "Ultrasound-activated agents comprised of 5FU-bearing nanoparticles bonded to microbubbles inhibit solid tumor growth and improve survival". In: *Molecular Therapy* 22.2 (2014), pp. 321–328.

[58] Sofie Snipstad et al. "Ultrasound improves the delivery and therapeutic effect of nanoparticle-stabilized microbubbles in breast cancer xenografts". In: *Ultrasound in medicine & biology* 43.11 (2017), pp. 2651–2669.

[59] Sofie Snipstad et al. "Sonopermeation enhances uptake and therapeutic effect of free and encapsulated cabazitaxel". In: *Ultrasound in Medicine & Biology* 47.5 (2021), pp. 1319–1333.

[60] Per Sontum et al. "Acoustic Cluster Therapy (ACT)–A novel concept for ultrasound mediated, targeted drug delivery". en. In: *Int. J. Pharm.* 495.2 (Nov. 2015), pp. 1019–1027.

[61] Annemieke van Wamel et al. "Acoustic Cluster Therapy (ACT) enhances the therapeutic efficacy of paclitaxel and Abraxane® for treatment of human prostate adenocarcinoma in mice". In: *Journal of controlled release* 236 (2016), pp. 15–21.

[62] Shino Magaki et al. "An introduction to the performance of immunohistochemistry". en. In: *Methods Mol. Biol.* 1897 (2019), pp. 289–298.

[63] Michael J Sanderson et al. "Fluorescence microscopy". en. In: *Cold Spring Harb. Protoc.* 2014.10 (Oct. 2014), db.top071795.

[64] S W Paddock. “Principles and practices of laser scanning confocal microscopy.” en. In: *Mol Biotechnol* 16.5 (2000), pp. 127–149.

[65] S W Paddock. “Confocal laser scanning microscopy”. en. In: *Biotechniques* 27.5 (Nov. 1999), pp. 992–6, 998–1002, 1004.

[66] FujiFilm Visualsonics. Preparation Protocol for the Non-Targeted Vevo MicroMarker Contrast Agent.

[67] Michel Schneider. “Characteristics of sonovue™”. In: *Echocardiography* 16 (1999), pp. 743–746.

[68] Per Christian Sontum. “Physicochemical characteristics of Sonazoid™, a new contrast agent for ultrasound imaging”. In: *Ultrasound in medicine & biology* 34.5 (2008), pp. 824–833.

[69] Hamdi Nsairat et al. “Liposomes: structure, composition, types, and clinical applications”. en. In: *Heliyon* 8.5 (May 2022), e09394.

[70] Charlotte Årseth. “Effect of Ultrasound and Microbubbles on Vasculature and Extracellular Matrix Components in Murine Breast Cancer Tumors”. MA thesis. NTNU, 2022.

[71] Hans J Welkoborsky, Maria Albers, and Julian Küstermeyer. “Perfusion analysis of benign parotid gland tumors by contrast-enhanced ultrasonography (CEUS)”. In: *European Archives of Oto-Rhino-Laryngology* 279.8 (2022), pp. 4137–4146.

[72] David E Goertz, Raffi Karshafian, and Kullervo Hynynen. “Antivascular effects of pulsed low intensity ultrasound and microbubbles in mouse tumors”. In: *2008 IEEE Ultrasonics Symposium*. IEEE. 2008, pp. 670–673.

[73] Chung-Yin Lin et al. “Ultrasound sonication with microbubbles disrupts blood vessels and enhances tumor treatments of anticancer nanodrug”. In: *International journal of nanomedicine* (2012), pp. 2143–2152.

[74] Anne Rix et al. “Effects of contrast-enhanced ultrasound treatment on neoadjuvant chemotherapy in breast cancer”. In: *Theranostics* 11.19 (2021), p. 9557.

[75] Anna Kurbatskaya. “Effect of Ultrasound-Stimulated Microbubble Treatment on Blood Perfusion in Tumors”.

[76] Matilde Maardalen. “Effects of Ultrasound and Microbubble Treatment on Blood Perfusion in Tumor Xenografts”.

[77] Anna Kurbatskaya. “Effects of ultrasound-stimulated microbubble treatment on blood perfusion and vascular permeability in tumors”. MA thesis. NTNU, 2020.

[78] Xiaowen Hu et al. "Insonation of targeted microbubbles produces regions of reduced blood flow within tumor vasculature". In: *Investigative radiology* 47.7 (2012), p. 398.

[79] Joo Ha Hwang et al. "Vascular effects induced by combined 1-MHz ultrasound and microbubble contrast agent treatments in vivo". In: *Ultrasound in medicine & biology* 31.4 (2005), pp. 553–564.

[80] Andrew KW Wood et al. "Antivascular ultrasound therapy extends survival of mice with implanted melanomas". In: *Ultrasound in medicine & biology* 36.5 (2010), pp. 853–857.

[81] Caitlin W Burke et al. "Inhibition of glioma growth by microbubble activation in a subcutaneous model using low duty cycle ultrasound without significant heating". In: *Journal of neurosurgery* 114.6 (2011), pp. 1654–1661.

[82] David E Goertz et al. "Antitumor effects of combining docetaxel (taxotere) with the antivascular action of ultrasound stimulated microbubbles". In: *PloS one* 7.12 (2012), e52307.

[83] Charlotte Årseth. "Effects of Acoustic Cluster Therapy on the Vasculature of Murine Pancreatic Tumors".

[84] Annemieke van Wamel et al. "Ultrafast microscopy imaging of acoustic cluster therapy bubbles: Activation and oscillation". In: *Ultrasound in Medicine & Biology* 48.9 (2022), pp. 1840–1857.

[85] Nathalie Lassau et al. "Metastatic renal cell carcinoma treated with sunitinib: early evaluation of treatment response using dynamic contrast-enhanced ultrasonography". In: *Clinical Cancer Research* 16.4 (2010), pp. 1216–1225.

[86] Nathalie Lassau et al. "Validation of dynamic contrast-enhanced ultrasound in predicting outcomes of antiangiogenic therapy for solid tumors: the French multicenter support for innovative and expensive techniques study". In: *Investigative radiology* 49.12 (2014), p. 794.

[87] Håkon Fossland Wesche. "Identifying barriers in extracellular matrix for ultrasound-mediated delivery of nanoparticles in 4T1, KPC and CT26 tumor models". MA thesis. NTNU, 2023.

Appendix A

Tables

A.1 CEUS Data

Table A.1: CEUS parameters for the total tumor for all CT26 animals used in the perfusion study. If not specified, the unit is [a.u.].

Animal	**PE**	**WiAUC**	**RT[s]**	**TTP[s]**	**WiR**	**WiPI**	**QOF[%]**	**Area[mm^2]**
76	46.52	1438.54	43.48	46.90	2.20	33.08	98.88	33.81
77	85.47	6298.62	94.99	98.31	2.99	66.31	98.46	34.45
78	21.43	720.76	45.56	47.44	1.16	15.82	58.44	34.94
79	61.61	1813.05	40.81	43.34	3.31	44.43	98.93	46.42
80	69.20	814.00	17.69	22.12	6.27	46.00	96.27	23.33
81	82.83	1626.58	28.49	32.38	5.27	57.09	97.89	44.79
84	22.39	986.39	60.85	64.70	0.81	16.21	98.60	46.71
85	41.30	964.00	34.72	41.62	1.99	27.80	93.93	56.08
86	33.80	1080.00	45.31	49.46	1.48	23.80	98.98	67.25
87	22.95	903.29	54.47	57.70	0.93	16.58	98.50	72.08
88	46.74	1357.19	40.00	42.20	2.64	33.93	99.07	69.06
89	17.69	531.41	40.38	41.98	1.10	13.16	97.91	59.26
90	32.39	2909.82	107.01	109.41	1.42	27.19	96.24	52.16
Mean	44.95	1649.51	50.29	53.66	2.43	32.42	94.78	49.26
SD	23.33	1526.47	25.02	24.68	1.69	16.76	11.02	15.17

Table A.2: CEUS parameters for the tumor center for all CT26 animals used in the perfusion study. If not specified, the unit is [a.u.].

Animal	PE	WiAUC	RT[s]	TTP[s]	WiR	WiPI	QOF[%]	Area[mm^2]
76	38.08	1307.18	48.32	52.18	1.62	27.05	98.95	21.94
77	79.89	6935.68	113.35	118.23	2.19	61.19	97.30	19.25
78	22.84	748.76	46.00	49.46	1.03	16.28	91.78	22.77
79	58.16	1625.55	38.35	40.32	3.49	42.39	98.67	30.98
80	61.00	1100.00	25.92	28.80	4.45	42.50	97.62	13.1
81	67.44	1540.03	32.76	36.38	3.90	47.01	97.11	42.28
84	22.54	918.96	56.53	60.04	0.87	16.25	98.30	28.84
85	37.40	931.00	35.80	39.90	1.96	26.00	98.93	32.43
86	28.80	1110.00	53.46	56.94	1.17	20.70	98.29	42.49
87	18.68	813.40	60.10	63.54	0.70	13.53	97.65	47.65
88	46.58	1279.28	37.63	39.54	2.87	33.99	99.00	48.42
89	15.60	1173.42	87.58	89.16	0.91	13.40	96.40	39.78
90	29.03	3765.75	174.58	182.13	0.53	21.57	96.25	34.67
Mean	40.46	1788.38	62.34	65.89	1.98	29.37	97.40	32.66
SD	20.54	1727.67	41.34	42.47	1.31	14.97	1.93	11.22

Table A.3: CEUS parameters for the tumor periphery for all CT26 animals used in the perfusion study. If not specified, the unit is [a.u.].

Animal	PE	WiAUC	RT[s]	TTP[s]	WiR	WiPI	QOF[%]	Area[mm^2]
76	46.69	1441.30	43.47	46.96	2.20	33.16	98.92	34.27
77	85.74	6617.30	97.24	100.95	2.98	68.05	97.99	34.51
78	23.44	721.08	41.44	42.98	1.43	17.40	68.66	35.07
79	61.51	1800.23	40.65	43.24	3.29	44.29	98.98	46.66
80	72.50	826.00	17.23	22.10	6.61	47.90	97.73	23.52
81	83.40	1665.39	28.94	32.76	5.25	57.54	97.83	18.27
84	22.16	972.51	60.82	64.84	0.79	15.99	98.59	46.74
85	39.90	990.00	36.39	42.22	1.92	27.20	96.29	56.02
86	33.70	1060.00	44.72	48.96	1.48	23.70	98.89	67.44
87	22.78	895.74	54.27	57.38	0.94	16.50	98.58	72.54
88	47.82	1569.42	45.74	48.82	2.24	34.32	95.51	20.72
89	25.33	665.80	36.20	38.18	1.58	18.39	98.42	19.72
90	32.33	2897.97	106.65	109.03	1.43	27.17	96.23	52.48
Mean	45.95	1701.75	50.29	53.72	2.47	33.20	95.59	40. 61
SD	22.99	1596.65	25.36	25.10	1.72	16.72	8.17	18.08

Table A.4: CEUS parameters for the total tumor for all CT26 animals used in the nanoparticle study. Animals highlighted with * were excluded. If not specified, the unit is [a.u.].

Animal	PE	WiAUC	RT[s]	TTP[s]	WiR	WiPI	QOF[%]	Area[mm^2]
199	28.04	838.13	44.09	51.86	1.09	19.01	94.27	69.70
200	31.59	1266.10	57.10	62.66	1.08	22.18	95.78	83.01
201	36.59	832.91	32.21	35.02	2.28	25.86	93.13	97.00
202	20.82	572.65	37.67	39.56	1.28	15.20	98.88	125.47
203	25.84	708.47	37.86	40.04	1.52	18.71	98.39	113.85
204	24.74	710.21	39.26	41.18	1.47	18.09	91.01	112.14
205	20.09	483.72	35.34	41.00	0.99	13.69	95.74	123.11
206*	26.52	178.35	8.51	8.60	11.99	20.95	0.00	77.74
207	25.39	536.81	29.28	31.06	1.91	18.33	99.32	122.93
208	22.57	577.82	35.40	37.50	1.41	16.32	97.62	112.25
219	40.82	954.96	32.22	34.00	2.86	29.64	98.36	114.56
220	37.13	907.82	33.75	35.70	2.46	26.90	99.36	119.85
221	26.15	635.94	33.12	34.62	1.89	19.20	98.05	111.20
222	31.53	712.73	30.84	32.28	2.42	23.11	98.63	89.08
Mean	28.56	749.10	36.78	39.73	1.74	20.48	96.81	107.24
SD	6.53	212.73	7.27	8.71	0.61	4.76	2.64	17.28

Table A.5: CEUS parameters for the tumor center for all CT26 animals used in the nanoparticle study. If not specified, the unit is [a.u.]. Animals highlighted with * were excluded.

Animal	PE	WiAUC	RT[s]	TTP[s]	WiR	WiPI	QOF[%]	Area[mm^2]
199	17.63	520.37	43.04	49.28	0.73	12.09	98.92	41.82
200	22.02	918.48	62.83	79.10	0.56	14.62	98.10	48.71
201	39.54	840.86	29.97	32.40	2.69	28.06	98.91	55.75
202	15.96	474.12	40.25	41.92	0.97	11.78	97.30	79.17
203	24.56	739.33	41.64	44.12	1.31	17.75	98.12	68.56
204	12.97	267.70	28.52	30.18	1.01	9.39	98.43	66.52
205	16.74	444.27	37.45	40.56	0.91	11.86	98.72	76.06
206*	23.37	235.61	13.41	13.80	4.74	17.57	0.00	43.79
207	23.97	506.75	29.11	30.70	1.87	17.41	98.38	78.51
208	25.31	623.93	34.01	35.94	1.67	18.35	99.38	68.76
219	27.25	597.97	29.51	30.62	2.34	20.26	98.79	70.29
229	29.12	621.58	29.20	30.62	2.33	21.29	99.20	75.04
221	15.21	382.02	33.85	35.12	1.13	11.29	96.78	64.06
222	23.40	611.85	35.44	36.92	1.62	17.26	98.12	56.27
Mean	22.59	580.71	36.52	39.81	1.47	16.26	98.40	65.35
SD	7.16	179.88	9.38	13.23	0.68	5.17	0.73	11.65

Table A.6: CEUS parameters for the tumor periphery for all CT26 animals used in the nanoparticle study. If not specified, the unit is [a.u.]. Animals highlighted with * were excluded.

Animal	PE	WiAUC	RT[s]	TTP[s]	WiR	WiPI	QOF[%]	Area[mm^2]
199	29.60	874.39	43.27	50.04	1.20	20.21	93.42	70.05
200	31.35	1223.61	56.03	62.26	1.06	21.84	94.92	82.84
201	36.34	856.73	33.17	35.80	2.25	25.83	91.68	96.91
202	21.07	589.13	38.17	39.98	1.30	15.43	98.95	126.04
203	25.99	698.26	37.19	39.44	1.54	18.77	98.50	114.00
204	24.49	664.11	37.38	39.48	1.48	17.76	91.61	111.82
205	19.60	459.01	34.45	40.22	0.98	13.32	95.84	123.36
206*	26.46	174.55	8.34	8.42	12.36	20.93	0.00	77.52
207	25.40	532.11	29.06	30.86	1.91	18.31	99.24	123.33
208	22.97	561.32	34.04	36.30	1.45	16.49	98.23	112.74
219	36.01	629.52	24.45	26.20	3.11	25.74	99.28	114.21
229	37.15	898.81	33.47	35.46	2.46	26.85	99.28	119.75
221	42.27	949.72	31.37	33.56	2.86	30.27	97.89	46.99
222	31.62	712.04	30.70	32.12	2.45	23.19	98.64	89.53
Mean	29.53	742.21	35.60	38.59	1.85	21.08	96.73	102.43
SD	6.98	210.57	7.70	9.13	0.71	5.04	2.91	23.98

Table A.7: CEUS parameters for the total tumor for all 4T1 animals. If not specified, the unit is [a.u.]. Animals highlighted with * were excluded.

Animal	PE	WiAUC	RT[s]	TTP[s]	WiR	WiPI	QOF[%]	Area[mm^2]
209	50.18	1113.50	30.71	32.54	3.62	36.26	98.93	68.92
210	56.03	1054.37	26.46	28.52	4.37	39.85	99.26	71.76
211	17.43	342.11	28.22	31.42	1.16	12.12	99.04	71.13
212	44.90	698.08	22.58	25.64	3.60	30.91	98.22	77.71
213	32.18	684.06	30.16	32.90	2.12	22.68	99.54	73.57
214	37.71	633.19	23.91	26.22	3.08	26.48	99.35	75.85
215*	23.13	686.84	-152.81	41.32	1.70	-4.49	71.80	47.38
216	20.84	508.68	34.73	38.02	1.18	14.65	98.51	83.07
217	18.10	444.61	35.09	38.66	1.00	12.67	98.96	76.96
218	27.65	457.04	24.40	28.74	1.94	18.73	98.98	71.31
223	42.13	591.03	19.43	20.62	4.77	30.41	99.37	73.95
224	16.52	425.81	35.98	38.48	0.98	11.83	97.13	61.31
225	39.99	600.68	21.83	24.82	3.31	27.51	97.79	68.90
226	44.10	795.57	25.75	28.34	3.32	30.90	98.65	76.94
Mean	34.44	642.21	27.63	30.38	2.65	24.23	98.75	73.18
SD	13.33	233.25	5.38	5.63	1.32	9.53	0.69	5.34

Table A.8: CEUS parameters for the tumor center for all 4T1 animals. If not specified, the unit is [a.u.].

Animal	PE	WiAUC	RT[s]	TTP[s]	WiR	WiPI	QOF[%]	Area[mm^2]
209	45.36	626.14	20.13	23.02	4.02	31.11	98.08	36.01
210	59.63	1089.46	25.45	27.16	5.03	42.80	98.73	38.98
211	14.14	253.29	25.87	29.04	1.01	9.79	98.66	43.44
212	35.10	588.06	23.94	26.38	2.83	24.57	98.48	44.88
213	33.74	702.66	29.16	31.28	2.43	24.10	99.15	40.88
214	35.41	502.94	20.40	22.66	3.28	24.66	98.71	43.49
215	6.72	113.12	24.32	27.30	0.51	4.65	95.75	23.28
216	18.33	334.46	26.24	29.24	1.31	12.75	97.88	49.55
217	13.49	275.06	29.34	32.72	0.86	9.37	98.56	44.79
218	28.46	407.20	21.42	26.34	2.16	19.01	98.93	41.39
223	38.65	451.81	16.47	17.80	4.80	27.43	98.63	43.71
224	18.52	449.98	34.21	36.94	1.11	13.16	96.63	34.09
225	39.29	491.80	18.45	21.62	3.66	26.66	98.42	39.59
226	26.05	493.19	26.63	28.72	2.01	18.52	97.76	44.72
Mean	29.49	484.23	24.43	27.16	2.50	20.61	98.17	40.63
SD	14.39	233.83	4.78	4.89	1.48	10.20	0.94	6.37

Table A.9: CEUS parameters for the tumor periphery for all 4T1 animals. If not specified, the unit is [a.u.]. Animals highlighted with * were excluded.

Animal	PE	WiAUC	RT[s]	TTP[s]	WiR	WiPI	QOF[%]	Area[mm^2]
209	50.51	1121.88	30.74	32.58	3.63	36.50	98.93	68.91
210	55.51	1048.82	26.58	28.68	4.29	39.46	99.26	71.85
211	17.47	343.37	28.28	31.50	1.16	12.14	99.05	71.34
212	45.40	705.04	22.63	25.84	3.59	31.16	98.45	77.53
213	32.33	688.68	30.24	33.02	2.12	22.77	99.54	73.76
214	37.96	637.57	23.93	26.26	3.10	26.65	99.34	75.80
215*	23.52	721.61	-150.16	42.86	1.60	-4.81	70.80	47.29
216	20.83	507.37	34.66	38.00	1.18	14.64	98.50	83.02
217	18.11	442.70	34.94	38.54	1.00	12.67	98.95	76.80
218	27.55	454.18	24.35	28.74	1.93	18.65	99.00	71.28
223	42.54	606.95	19.74	20.92	4.77	30.74	99.41	73.99
224	16.51	424.99	35.93	38.42	0.98	11.83	97.14	61.45
225	39.56	590.92	21.72	24.70	3.28	27.21	97.80	68.98
226	44.22	800.76	25.85	28.44	3.31	30.98	98.70	76.96
Mean	33.72	649.63	14.96	31.32	2.57	22.18	96.78	71.35
SD	13.34	234.58	5.32	5.56	1.32	9.54	0.68	5.27

Table A.10: CEUS parameters for the total tumor for all KPC animals. If not specified, the unit is [a.u.].

Animal	PE	WiAUC	RT[s]	TTP[s]	WiR	WiPI	QOF[%]	Area[mm^2]
227	31.58	357.34	15.99	17.34	3.99	22.35	90.85	47.03
228	46.14	559.65	17.53	19.68	4.87	31.93	98.78	42.01
229	52.03	671.03	17.48	18.20	7.30	38.40	97.30	43.83
230	48.76	703.64	20.91	23.62	4.26	33.65	99.09	48.15
231	53.78	375.15	10.49	13.08	8.23	35.77	98.46	46.75
232	33.88	511.21	21.55	23.74	3.04	23.72	98.74	36.46
233	21.01	353.67	24.62	28.34	1.51	14.36	98.64	40.12
234	24.74	407.68	23.70	26.42	1.96	17.20	97.52	43.65
235	45.46	586.93	18.33	20.02	4.91	32.02	97.17	41.98
236	61.77	820.78	18.81	20.46	6.58	43.64	98.43	45.35
237	28.41	388.68	20.43	24.88	2.28	19.03	98.10	43.16
238	23.94	553.51	32.81	35.82	1.45	16.87	83.74	45.19
239	19.81	259.40	19.99	26.74	1.51	12.98	77.27	44.67
240	27.37	406.21	20.83	22.40	2.73	19.51	82.72	52.84
Mean	37.05	496.78	20.25	22.91	3.90	25.82	94.06	44.37
SD	13.85	159.94	5.00	5.57	2.24	9.86	7.36	3.87

Table A.11: CEUS parameters for the tumor center for all KPC animals. If not specified, the unit is [a.u.].

Animal	PE	WiAUC	RT[s]	TTP[s]	WiR	WiPI	QOF[%]	Area[mm^2]
227	25.43	347.37	19.32	20.98	2.65	17.98	98.43	25.57
228	36.87	442.34	17.17	18.98	4.11	25.76	98.75	21.84
229	31.19	426.69	19.01	20.22	3.57	22.45	98.14	23.30
230	44.70	614.65	19.86	22.28	4.17	30.96	99.27	26.14
231	28.58	296.84	15.09	17.12	3.43	19.68	99.21	24.93
232	26.93	407.96	21.33	23.04	2.59	19.13	98.34	20.03
233	13.30	238.28	25.96	29.30	0.94	9.18	99.07	21.91
234	23.21	398.14	24.21	26.24	1.94	16.44	98.33	23.29
235	40.76	526.64	18.54	20.56	4.18	28.41	92.83	22.55
236	62.71	759.80	17.13	18.60	7.37	44.35	98.26	26.51
237	18.57	310.81	24.08	26.84	1.45	12.91	98.91	22.12
238	8.94	231.59	35.77	37.82	0.56	6.47	96.18	26.57
239	18.29	343.76	26.27	28.14	1.47	13.08	81.97	26.35
240	28.45	457.06	22.04	23.18	2.97	20.73	98.86	31.95
Mean	29.14	414.42	21.84	23.81	2.96	20.54	96.90	24.50
SD	13.90	145.05	5.26	5.48	1.75	9.75	4.61	3.01

Table A.12: CEUS parameters for the tumor periphery for all KPC animals. If not specified, the unit is [a.u.].

Animal	PE	WiAUC	RT[s]	TTP[s]	WiR	WiPI	QOF[%]	Area[mm^2]
227	31.84	369.74	16.49	18.02	3.82	22.42	95.96	47.01
228	45.68	562.26	17.75	19.86	4.79	31.68	98.63	41.91
229	52.03	660.21	17.16	17.84	7.52	38.48	96.78	43.94
230	46.38	692.78	21.45	23.82	4.09	32.30	97.74	48.15
231	52.91	369.05	10.49	13.08	8.09	35.18	98.42	46.65
232	33.79	510.52	21.58	23.78	3.02	23.66	98.76	36.42
233	19.19	315.41	24.18	28.22	1.37	13.05	97.39	40.11
234	23.99	394.74	23.71	26.50	1.89	16.65	96.92	43.62
235	44.62	577.73	18.36	20.00	4.84	31.47	97.08	41.91
236	61.86	829.76	18.97	20.60	6.56	43.75	98.24	45.22
237	28.19	410.60	21.52	25.40	2.23	19.08	98.63	43.00
238	23.70	537.56	32.24	35.26	1.45	16.67	83.34	45.27
239	19.35	250.57	19.74	26.14	1.50	12.70	76.63	44.50
240	26.25	401.00	21.46	23.12	2.53	18.69	83.80	52.54
Mean	36.41	491.57	20.36	22.97	3.84	25.41	94.17	44.30
SD	13.92	162.03	4.87	5.41	2.27	9.97	7.22	3.83

A.2 Vasculature Parameters

Table A.13: Area fraction [%] of all blood vessels (BVs) and functional blood vessels (FBVs), and fraction of functional blood vessels (FBVs) for all tumor regions of CT26 tumors included in the USMB experiment.

Animal	All BVs [Area%]			FBVs [Area%]			Fraction of FBVs		
Control	**Total**	**Center**	**Per**	**Total**	**Center**	**Per**	**Total**	**Center**	**Per**
76	2.00	1.70	2.37	1.03	0.80	1.32	0.52	0.47	0.56
79	2.24	2.12	2.31	0.28	0.15	0.35	0.12	0.07	0.15
80	8.53	8.71	8.37	2.84	2.59	3.05	0.33	0.30	0.36
83	2.96	2.69	3.40	0.45	0.20	0.85	0.15	0.08	0.25
84	3.63	3.88	3.27	0.36	0.43	0.26	0.10	0.11	0.08
89	5.36	5.34	5.39	0.76	0.68	0.87	0.14	0.13	0.16
90	7.42	7.82	6.92	2.34	2.26	2.43	0.31	0.29	0.35
Mean	4.59	4.61	4.58	1.15	1.02	1.30	0.24	0.21	0.27
SD	2.579	2.785	2.369	1.024	0.994	1.056	0.154	0.151	0.163
Treated	**Total**	**Center**	**Per**	**Total**	**Center**	**Per**	**Total**	**Center**	**Per**
77	6.07	5.67	6.73	0.67	0.43	1.06	0.11	0.08	0.16
78	7.00	7.04	6.94	0.44	0.37	0.52	0.06	0.05	0.08
81	8.37	9.15	7.20	1.00	0.66	1.49	0.12	0.07	0.21
82	7.02	6.75	7.40	0.83	0.75	0.93	0.12	0.11	0.13
85	3.33	2.98	3.65	0.22	0.15	0.28	0.07	0.05	0.08
86	2.71	1.95	3.85	0.14	0.04	0.28	0.05	0.02	0.07
87	3.67	3.97	3.30	0.04	0.02	0.05	0.01	0.01	0.02
88	6.33	6.07	6.63	0.12	0.03	0.23	0.02	0.00	0.03
Mean	5.56	5.45	5.71	0.43	0.31	0.60	0.07	0.05	0.10
SD	2.056	2.358	1.774	0.362	0.292	0.502	0.043	0.037	0.064

Table A.14: Area fraction [%] of all blood vessels (BVs) and functional blood vessels (FBVs), and fraction of functional blood vessels (FBVs) for all tumor regions of 4T1 tumors included in the USMB experiment.

Animal	**All BVs [Area%]**			**FBVs [Area%]**			**Fraction of FBVs**		
Control	**Total**	**Center**	**Per**	**Total**	**Center**	**Per**	**Total**	**Center**	**Per**
53	3.01	3.84	2.16	0.44	0.39	0.48	0.14	0.10	0.22
55	5.28	5.63	4.80	0.28	0.12	0.49	0.05	0.02	0.10
56	2.68	2.21	3.24	0.85	0.58	1.17	0.32	0.26	0.36
57	2.82	2.39	3.27	0.31	0.17	0.46	0.11	0.07	0.14
61	3.44	3.54	3.33	0.39	0.19	0.60	0.11	0.05	0.18
62	2.44	2.31	2.57	0.31	0.13	0.31	0.13	0.06	0.12
Mean	3.28	3.32	3.23	0.43	0.26	0.59	0.14	0.09	0.19
SD	1.038	1.327	0.899	0.216	0.185	0.302	0.091	0.086	0.095
Treated	**Total**	**Center**	**Per**	**Total**	**Center**	**Per**	**Total**	**Center**	**Per**
52	1.68	1.43	1.97	0.02	0.01	0.04	0.01	0.004	0.02
54	6.96	8.35	5.77	0.20	0.08	0.29	0.03	0.01	0.05
58	5.42	6.02	4.72	0.28	0.16	0.43	0.05	0.03	0.09
59	4.51	4.27	4.74	0.07	0.04	0.10	0.02	0.01	0.02
60	1.62	1.73	1.50	0.13	0.05	0.21	0.08	0.03	0.14
63	4.69	5.08	4.24	0.27	0.09	0.49	0.06	0.02	0.12
Mean	4.14	4.48	3.82	0.16	0.07	0.26	0.04	0.02	0.07
SD	2.119	2.632	1.699	0.108	0.052	0.179	0.027	0.011	0.051

Table A.15: Area fraction [%] of all blood vessels (BVs) and functional blood vessels (FBVs), and fraction of functional blood vessels (FBVs) for all tumor regions of CT26 tumors included in the ACT experiment.

Animal	**All BVs [Area%]**			**FBVs [Area%]**			**Fraction of FBVs**		
Control	**Total**	**Center**	**Per**	**Total**	**Center**	**Per**	**Total**	**Center**	**Per**
183	5.57	4.81	6.57	1.71	1.51	1.98	0.31	0.31	0.30
188	4.04	3.92	4.18	0.66	0.44	0.93	0.16	0.11	0.22
192	4.64	5.24	3.82	1.15	1.10	1.22	0.25	0.21	0.32
195	5.37	5.15	5.64	0.83	0.76	0.91	0.15	0.15	0.16
198	6.38	5.84	7.19	0.72	0.57	0.96	0.11	0.10	0.13
Mean	5.20	4.99	5.48	1.01	0.87	1.20	0.20	0.18	0.23
SD	0.90	0.70	1.47	0.43	0.43	0.45	0.08	0.09	0.08
Treated	**Total**	**Center**	**Per**	**Total**	**Center**	**Per**	**Total**	**Center**	**Per**
182	3.22	3.21	3.24	0.48	0.42	0.56	0.15	0.13	0.17
187	2.34	2.13	2.57	0.29	0.14	0.47	0.13	0.07	0.18
189	7.82	6.86	9.16	1.29	1.29	1.27	0.16	0.19	0.14
193	3.67	3.26	4.33	0.38	0.26	0.55	0.10	0.08	0.13
194	5.08	5.63	4.44	0.87	0.68	1.09	0.17	0.12	0.25
197	6.14	6.11	6.19	1.23	1.12	1.40	0.20	0.18	0.23
Mean	4.71	4.53	4.99	0.76	0.65	0.89	0.15	0.13	0.18
SD	2.04	1.91	2.39	0.44	0.47	0.41	0.03	0.05	0.05

Table A.16: Mean and SD, relative change and p-value for the fraction of functional blood vessels for CT26 animals in the Sonovue experiment. Statistical significance is highlighted with *.

	Mean fraction ± SD			
Region	**Control**	**Treated**	**Rel. change (%)**	**p**
Total	0.24 ± 0.154	0.07 ± 0.043	-71	$0.0109*$
Center	0.21 ± 0.151	0.05 ± 0.037	-76	$0.0126*$
Periphery	0.27 ± 0.163	0.10 ± 0.064	-63	$0.0152*$

Table A.17: Mean and SD, relative change and p-value for the fraction of functional blood vessels for 4T1 animals in the Sonovue experiment. Statistical significance is highlighted with *.

	Mean fraction ± SD			
Region	**Control**	**Treated**	**Rel. change (%)**	**p**
Total	0.14 ± 0.091	0.04 ± 0.027	-71	$0.0264*$
Center	0.09 ± 0.086	0.02 ± 0.011	-78	0.0567
Periphery	0.19 ± 0.095	0.07 ± 0.051	-63	$0.0280*$

Table A.18: Mean and SD, relative change and p-value for the fraction of functional blood vessels for CT26 animals in the ACT experiment.

	Mean fraction ± SD			
Region	**Control**	**Treated**	**Rel. change (%)**	**p**
Total	0.20 ± 0.08	0.15 ± 0.03	-25	0.2406
Center	0.18 ± 0.09	0.13 ± 0.05	-28	0.2925
Periphery	0.23 ± 0.08	0.18 ± 0.05	-22	0.2823

A.3 Tumor Uptake Data from Pearl

Table A.19: Mean fluorescence from the Pearl analysis for CT26, 4T1 and KPC tumors, including means and standard deviations.

	CT26		**4T1**		**KPC**	
	Control	**Treated**	**Control**	**Treated**	**Control**	**Treated**
	0.031	0.042	0.105	0.056	0.08	0.071
	0.045	0.051	0.088	0.061	0.069	0.067
	0.044	0.038	0.075	0.086	0.052	0.072
	0.033	0.063	0.076	0.059	0.053	0.047
	0.036	0.064	0.089	0.061	0.075	0.077
	0.046	0.034	0.066	0.045	0.037	0.052
	0.036	0.073	0.078	0.057	0.069	0.069
Mean	0.039	0.052	0.082	0.061	0.062	0.065
SD	0.006	0.015	0.013	0.012	0.015	0.011

A.4 Nanoparticle Extravasation Data

Table A.20: Mean extravasation distance in µm for CT26 animals, control and USMB treated group and for the total tumor, core and periphery of the tumor. Means and standard deviations are also given.

Region	**Total**		**Core**		**Periphery**	
Group	**Control**	**Treated**	**Control**	**Treated**	**Control**	**Treated**
	33.42	44.28	85.63	87.52	33.42	44.28
	40.67	89.35	63.63	37.20	40.67	89.35
	22.68	69.00	70.46	34.90	22.68	69.00
	45.22	22.43	46.19	50.81	45.22	22.43
	42.77	66.55	74.14	145.68	42.77	66.55
	75.36	29.66	14.53	34.72	75.36	29.66
	32.34	29.62	53.23	53.09	32.34	29.62
	85.63	87.52				
	63.63	37.20				
	70.46	34.90				
	46.19	50.81				
	74.14	145.68				
	14.53	34.72				
	53.23	53.09				
Mean	50.02	56.77	58.26	63.42	41.78	50.13
SD	21.26	33.24	23.32	40.70	16.66	25.19

Table A.21: Distribution of extravasated nanoparticles (NPs) along each extravasation distance (ED).

Region	**Total**		**Core**		**Periphery**	
Group	**Control**	**Treated**	**Control**	**Treated**	**Control**	**Treated**
ED [µm]	**Percentage extravasated NPs**					
0-10	7.011	15.891	7.539	14.719	6.627	16.485
10-20	18.014	12.554	9.590	14.234	22.594	11.702
20-30	9.970	11.356	5.765	8.532	12.244	12.790
30-40	12.036	11.125	11.364	7.845	11.455	12.790
40-50	12.016	8.769	12.971	7.279	11.328	9.526
50-60	13.941	6.795	25.499	4.488	9.214	7.966
60-70	3.526	2.288	2.993	3.154	3.787	1.848
70-80	2.736	3.568	5.710	2.952	1.010	3.880
80-90	5.025	7.721	2.661	9.341	6.311	6.898
90-100	2.776	4.017	1.940	4.812	3.219	3.613
100-110	1.966	4.357	3.271	4.650	1.199	4.209
110-120	2.776	3.227	2.106	2.669	3.124	3.511
120-130	2.837	2.533	0.388	7.117	4.197	0.205
130-140	1.175	1.852	0.554	2.305	1.515	1.622
140-150	1.743	0.259	3.880	0.202	0.505	0.287
150-160	0.020	0.286	0.055	0.202	0.000	0.328
160-170	0.831	1.048	0.499	3.114	1.010	0.000
170-180	1.540	0.558	3.049	1.092	0.663	0.287
180-190	0.041	1.321	0.111	0.040	0.000	1.971
190-200	0.020	0.477	0.055	1.254	0.000	0.082

A.5 Tumor Weight

Table A.22: Tumor weight [g] for all animals. No. denotes animal number. CT26-1 and 4T1-1 was included in the Sonovue study, CT26-2, 4T1-2 and KPC in the liposome study, and CT26-3 in the ACT study.

CT26-1		**4T1-1**		**CT26-2**		**4T1-2**		**KPC**		**CT26-3**	
No.	**Weight**	**No.**	**Weight**	**No.**	**Weight**	**No.**	**Weight**	**No.**	**Weight**	**No.**	**Weight**
76	0.4619	53	0.3821	199	0.688	209	0.4243	228	0.1439	182	0.7197
77	0.3497	55	0.2568	201	0.91	210	0.4106	230	0.1123	183	0.6131
78	0.5434	56	0.0395	203	1.35	213	0.5127	231	0.108	187	0.7029
79	0.5863	57	0.3609	204	0.96	214	0.5161	234	0.0932	188	0.4583
80	0.2428	61	0.3395	207	1.03	218	0.6724	235	0.1042	189	0.421
81	0.3203	62	0.3886	220	1.29	225	0.4502	237	0.035	192	0.508
82	0.1726	52	0.3147	221	1.04	226	0.3674	238	0.1181	193	0.6149
83	0.4497	54	0.3462	200	0.88	211	0.5421	227	0.096	194	0.5035
84	0.926	58	0.0802	202	1.03	212	0.4698	229	0.1002	195	0.5256
85	0.4876	59	0.4613	205	1.57	215	0.1778	232	0.0723	197	0.5032
86	0.8008	60	0.5983	206	0.87	216	0.6675	233	0.0561	198	0.7008
87	0.7573	63	0.2598	208	1.19	217	0.5736	236	0.1519		
88	0.629			219	1.07	223	0.5931	239	0.07		
89	0.7246			222	0.901	224	0.4855	240	0.197		
90	0.6065										
Avg.	0.5372		0.3190		1.0556		0.4902		0.1042		0.5700

A.6 Correlation Data

A.6.1 Fraction of Functional Blood Vessels and Total Amount of Blood Vessels

Table A.23: Correlation between functional blood vessels and total amount of blood vessels for CT26 animals in USMB experiment, control and treated group.

	Control			**Treated**		
Tumor Region	**p**	**R^2**	**r**	**p**	**R^2**	**r**
Total	0.7795	0.01716	0.1310	0.1471	0.3158	0.5620
Center	0.6795	0.03699	0.1923	0.2240	0.2345	0.4842
Periphery	0.7527	0.02168	0.1473	0.1226	0.3497	0.5913

Table A.24: Correlation between functional blood vessels and total amount of blood vessels for 4T1 animals in USMB experiment, control and treated group.

	Control			**Treated**		
Tumor Region	**p**	**R^2**	**r**	**p**	**R^2**	**r**
Total	0.2405	0.3217	-0.5672	0.7928	0.0193	-0.1390
Center	0.2714	0.2889	-0.5375	0.9990	0.0000005	0.0007
Periphery	0.5639	0.0898	-0.2997	0.6100	0.0709	-0.2663

Table A.25: Correlation between functional blood vessels and total amount of blood vessels for CT26 animals in the ACT experiment, control and treated group. Statistical significance is highlighted with *.

	Control			**Treated**		
Tumor Region	**p**	**R^2**	**r**	**p**	**R^2**	**r**
Total	0.7532	0.03804	-0.195	0.153	0.4367	0.6608
Center	0.8998	0.006201	-0.07875	0.0234*	0.7611	0.8724
Periphery	0.3974	0.2442	-0.4942	0.7007	0.04091	-0.2023

A.6.2 Tumor Weight and Fraction of Functional Blood Vessels

Table A.26: Correlation between tumor weight and fraction of functional blood vessels for control and USMB treated CT26 animals. Statistical significance is highlighted with *.

	Control			**Treated**		
Tumor Region	**p**	**R^2**	**r**	**p**	**R^2**	**r**
Total	0.1899	0.315	-0.5612	0.0027*	0.8014	-0.8952
Center	0.3054	0.2067	-0.4546	0.0006*	0.8752	-0.9355
Periphery	0.1054	0.4379	-0.6617	0.0228*	0.6065	-0.7788

Table A.27: Correlation between tumor weight and fraction of functional blood vessels for control and USMB treated 4T1 animals.

	Control			**Treated**		
Tumor Region	**p**	**R^2**	**r**	**p**	**R^2**	**r**
Total	0.0791	0.5785	-0.7606	0.7223	0.0351	0.1873
Center	0.0566	0.6383	-0.799	0.8729	0.007211	-0.08492
Periphery	0.0866	0.561	-0.749	0.8716	0.007359	0.08579

Table A.28: Correlation between tumor weight and fraction of functional blood vessels for control and ACT treated animals.

	Control			**Treated**		
Tumor Region	**p**	**R^2**	**r**	**p**	**R^2**	**r**
Total	0.8418	0.01552	-0.1246	0.2105	0.3568	-0.5974
Center	0.9289	0.003119	0.05584	0.1082	0.5153	-0.7178
Periphery	0.5474	0.1323	-0.3637	0.7648	0.02499	-0.1581

A.6.3 CEUS Parameters and Vasculature Parameters

Table A.29: Correlation between CEUS parameters and fraction of functional blood vessels for CT26 animals.

	p	**R^2**	**r**
PE vs fraction of FBVs	0.5071	0.1169	0.3419
RT vs fraction of FBVs	0.9799	0.0001792	-0.01339
WiAUC vs fraction of FBVs	0.6709	0.04977	0.2231
WiR vs fraction of FBVs	0.6009	0.07445	0.2729

Table A.30: Correlation between CEUS parameters and total amount of (%) blood vessels for CT26 animals.

	p	**R^2**	**r**
PE vs % BVs	0.2752	0.107	0.3271
RT vs % BVs	0.8751	0.002348	0.04846
WiAUC vs % BVs	0.5978	0.02613	0.1616
WiR vs % BVs	0.077	0.2571	0.5071

Table A.31: Correlation between CEUS parameters and tumor weight for CT26 animals. Statistical significance is highlighted with *.

	p	**R^2**	**r**
PE vs weight	0.0012*	0.6324	-0.7952
RT vs weight	0.5285	0.03708	0.1926
WiAUC vs weight	0.2387	0.1237	-0.3517
WiR vs weight	0.0008*	0.6533	-0.8082

A.6.4 Pearl Data and CEUS Parameters

Table A.32: Correlation between CEUS parameters and mean fluorescence (MF) for CT26 animals.

	Control			**Treated**		
	p	**R^2**	**r**	**p**	**R^2**	**r**
MF vs. PE	0.0789	0.4924	0.7017	0.6703	0.04996	-0.2235
MF vs. WiAUC	0.3806	0.156	0.3949	0.5158	0.1125	-0.3354
MF vs. RT	0.2993	0.2114	-0.4598	0.5501	0.09599	-0.3098

Table A.33: Correlation between CEUS parameters and mean fluorescence (MF) for 4T1 animals.

	Control			**Treated**		
	p	**R^2**	**r**	**p**	**R^2**	**r**
MF vs. PE	0.3725	0.1609	0.4011	0.4592	0.1434	-0.3787
MF vs. WiAUC	0.1319	0.3929	0.6268	0.8662	0.007999	-0.08944
MF vs. RT	0.1525	0.3626	0.6022	0.2111	0.3562	0.5968

Table A.34: Correlation between CEUS parameters and mean fluorescence (MF) for KPC animals. Statistical significance is indicated by *.

	Control			**Treated**		
	p	**R^2**	**r**	**p**	**R^2**	**r**
MF vs. PE	0.4235	0.1318	0.363	0.0686	0.517	0.719
MF vs. WiAUC	0.0484*	0.5742	0.7578	0.074*	0.5037	0.7097
MF vs. RT	0.8409	0.009	0.0941	0.2284	0.2735	-0.523

Appendix B

IHC Staining Protocol

- Defrost sections $2-5$ min in RT (room temperature)

Fixation

- Wash with PBS, 2 min
- Fix in acetone, 10 min
- Wash with PBS, 5 min

Pap Pen

- Draw around the edges of the section with a Pap Pen

Blocking

- Incubate in 100 µL 12% BSA + PBS, 50 min in RT
- Wash with PBS, 5 min

Primary Antibody

- Dilute primary Ab (Anti-CD31) $1:50$ with 12% BSA + PBS
- Incubate each section in 100 µL primary Ab solution in a lightproof box together with wet paper towels, 1 h in RT

- Wash with PBS, 3x5 min

Secondary Antibody

- Dilute secondary Ab (IgG-AF647) 1 : 50 with 12% BSA + PBS
- Incubate each section in 100 µL primary Ab solution in a lightproof box with wet paper towels, 1 h in RT
- Wash with PBS, 3x5 minutes

Mounting

- Mount with 8 to 12 µL VectaShield Vibrance, depending on the section size
- Place cover glass
- Store lightproof at 4°C

Appendix C

ImageJ Macro Scripts

C.1 Nanoparticle Macro Script

```
run("Subtract...", "value=20");
run("Gaussian Blur...", "sigma=1");
setAutoThreshold("RenyiEntropy dark");
setOption("BlackBackground", true);
run("Convert to Mask");
//Change file name
run("Remove Outliers...", "radius=0.5 threshold=30 which=Bright");
saveAs("Tiff", "/Users/andreabergekastellet/Documents/Master/NP/MATLAB
    script & images/0222_NP_positionM1.tif");
```

C.2 Blood Vessel Macro Script

```
run("Subtract...", "value=10");
run("Gaussian Blur...", "sigma=2");
run("Gray Morphology", "radius=3 type=diamond operator=close");
setAutoThreshold("Triangle dark");
setOption("BlackBackground", true);
run("Convert to Mask");
run("Remove Outliers...", "radius=5 threshold=30 which=Bright");
//Change filename: animal id and position
saveAs("Tiff", "/Users/andreabergekastellet/Documents/Master/NP/MATLAB
    script & images/0222_BV_positionM1.tif");
```

Appendix D

Matlab Script for Extravasation Distance

```
%Note: Additional file required: tiffread/bfopen.m
%Pixel size: dxy = 0.312
%Change pathname to your computer:
    [Filename, Pathname] = uigetfile('*.tif;*.tiff;*.lsm', 'select the
    image file: ',...
         '/Users/andreabergekastellet/Documents/Master/NP/MATLAB script &
    images','MultiSelect','On');

fprintf(1,'First File: %s\n', [Pathname char(Filename(1))]);
fprintf(1,'Last File: %s\n', [Pathname char(Filename(end))]);

nrFiles = round(length(Filename)/2);

prompt = {'Enter name of the SUM result file:', 'Dimension of image: 2D or
    3D', ...
    'Pixel size dxy in microns: '};
dlg_title = 'Information';
%num_lines = 2;
dims = [1 35];
def = {'results.txt', '2D', '0.4545'};
answer = inputdlg(prompt,dlg_title,dims, def);

if answer{2} == '3D'
    prompt = {'Pixel size dz in microns: '};
    dlg_title = 'Information';
    %num_lines = 2;
    dims = [1 35];
    def = {'1.0000'};
```

```
    answer2 = inputdlg(prompt,dlg_title,dims, def);
    dz = str2num(answer2{1});
end


filnavn = answer{1};
datafile = strcat(Pathname, filnavn);
SUM_datafile = strcat(Pathname, 'SUM_', filnavn);
np_fid = fopen(char(datafile),'a');
SUM_fid = fopen(char(SUM_datafile),'a');
fprintf(np_fid,'NP lump\t Vol(u)\t coloc\t bor-bor(u)\n');
fprintf(SUM_fid,'Files\t Total NPs\t coloc NPs\t nocoloc NPs\t Vol NPs(u)\t
    ');
fprintf(SUM_fid, 'Vol BVs(u)\t Vol colocNPs(u)\t Vol nocolocNPs(u)\n');


%Syntax must be as follows: xxxx_BV_positionyy and xxxx_NP_positionyy
%locate all the NP-images in the list of files:
test = strfind(Filename', '_NP');
b = 1;
n = 1;
%group the NV and the BV files together, store position in the Filname cell
     array
for i = 1:length(Filename)
    if isempty(test{i})
        BVnr_Filename(b) = i;
        b = b+1;
    else
        NPnr_Filename(n) = i;
        % Locate the position of the '_' in '_NP', store in posn:
        posn(n) = test{i};
        n = n+1;
    end
end

dxy = str2num(answer{3});

for f = 1:nrFiles
    f_NP = [Pathname Filename{NPnr_Filename(f)}];
    % find the position yy and find the corresponding BV-image
    test = Filename{NPnr_Filename(f)}(posn(f)+4:end);
    BV_pos = strfind(Filename(BVnr_Filename),test);
    for b = 1:length(BV_pos)
        if ~isempty(BV_pos{b})
            f_BV = [Pathname Filename{BVnr_Filename(b)}];
        end
```

```
70      end
71
72      filetxt= Filename{f};
73      fprintf(1,'Start analysis of:  %s\n',Filename{f});
74
75      BV0 = bfopen(f_BV);
76      NP0 = bfopen(f_NP);
77      BV1 = BV0{1,1};
78      NP1 = NP0{1,1};
79      nrZ = size(BV1,1);
80      XYdim = size(BV1{1,1});
81
82      for i = 1:nrZ
83          %binary images from ImageJ are 0 (black) and 255 (white)
84          BWbv(:,:,i) = logical(BV1{1,1});
85          BWnptemp(:,:,i) = logical(NP1{1,1});
86      end
87
88      if answer{2} == '3D'
89          BWnp = imclearborder(BWnptemp,26);
90          % ...need to figure how to fin dthe dz parameter in a 3D image!
91
92      %calculate the nr (dr_dellump) of pixels in a 10 cubic micron big lump
        !)
93         % nr_dellump = round(10/(dxy^2*dz));
94         % lumps of 9 pisels are removed!
95          nr_dellump = 9;
96          BWbv = bwareaopen(BWbv,nr_dellump);
97
98      %For binary matrix BWbv and BWnp, max 3D connectivity = 26
99      %Holes are already filled in ImageJ
100         BWnp = imfill(BWnp, 26, 'holes');
101         BWbv = imfill(BWbv, 26, 'holes');
102
103     %Need only perimeter-pixels to calculate bor-bor distances!
104         BW_npp = bwperim(BWnp,26);
105         BW_bvp = bwperim(BWbv,26);
106     %CC = bwconncomp(BW_npp,26);
107     else
108         BWnp = imclearborder(BWnptemp,8);
109         %nr_dellump = round(10/(dxy^2));
110         %LUMPS SOM ER 1-2-3-4 PIXELS FJERNES!!!
111         nr_dellump = 4;
112         BWbv = bwareaopen(BWbv,nr_dellump);
113         BWbv = imfill(BWbv, 8, 'holes');
114         BWnp = imfill(BWnp, 8, 'holes');
```

```
115         BW_npp = bwperim(BWnp,8);
116         BW_bvp = bwperim(BWbv,8);
117     end
118 
119     STATSnp = regionprops(BW_npp, 'PixelList');
120     STATSnp_fill = regionprops(BWnp,'Area','PixelList');
121     N_np = length(STATSnp);
122     %Lnp = labelmatrix(CC);
123     %CC = bwconncomp(BW_bvp,26);
124     STATSbv = regionprops(BW_bvp,'PixelList');
125     STATSbv_fill = regionprops(BWbv,'Area','PixelList');
126     N_bv = length(STATSbv);
127 
128 
129     fprintf(1,'Number of NPs and BVs: %i\t%i\n',N_np, N_bv);
130     fprintf(1,'Pixelsize (um): %6.4f\n',dxy);
131     % For the NP = n that have no coloc for the BV (1 to N_bv), ie. all
    elements in row n = 0, calculate minimum bor-bor distance to all the BV
    's. Use the STATSnp and STATSbv for this!
132 
133     % For the NP = n having coloc, some elements in the row = 1, calculate
    the
134     % coloc, the fraction of n's volume that is inside a vessel.
135     % Use the STATSnp_fill and STATSbv_fill for this!
136 
137     BVvol = zeros(1,N_bv);
138     %NPfrac = zeros(1,N_np);
139     NPvol = zeros(1,N_np);
140     borbor = zeros(1,N_np);
141     coloc = zeros(N_np,N_bv);
142     NPfrac = zeros(1,N_np);
143     Volcoloc = zeros(1,N_np);
144     %For every NP....
145     for i = 1:N_np
146         frac = zeros(1,N_bv);
147         nrpix = zeros(1,N_bv);
148         %...test coloc with all the BV's!
149         for j = 1:N_bv
150             Lia = ismember(STATSnp_fill(i).PixelList, STATSbv_fill(j).
    PixelList,'rows');
151             if nnz(Lia) > 0
152                 coloc(i,j) = 1;
153                 frac(j) = nnz(Lia)/STATSnp_fill(i).Area;
154                 nrpix(j) = nnz(Lia);
155             end
156         end
```

```
157         %It could be that a NP is coloc'ed with several BV's
158         NPfrac(i) = 100*sum(frac);
159         if answer{2} == '3D'
160             Volcoloc(i) = dxy^2*dz*sum(nrpix);
161         else
162             Volcoloc(i) = dxy^2*sum(nrpix);
163         end
164         % If there's no coloc, calculate bor-bor distance!
165         if nnz(coloc(i,:)) == 0
166             [npix, dummy] = size(STATSnp(i).PixelList);
167             minpix = zeros(1,npix);
168             minBVpix = zeros(1,N_bv);
169             %Test for every BV
170             for j = 1:N_bv
171                 for k = 1:npix
172                     x1 = STATSnp(i).PixelList(k,1);
173                     y1 = STATSnp(i).PixelList(k,2);
174                     if answer{2} == '3D'
175                         z1 = STATSnp(i).PixelList(k,3);
176                     end
177                     diffx = (STATSbv(j).PixelList(:,1)-x1)*dxy;
178                     diffy = (STATSbv(j).PixelList(:,2)-y1)*dxy;
179                     if answer{2} == '3D'
180                         diffz = (STATSbv(j).PixelList(:,3)-z1)*dz;
181                         alldist=sqrt(diffx.^2+diffy.^2+diffz.^2);
182                     else
183                         alldist=sqrt(diffx.^2+diffy.^2);
184                     end
185                     %alldist=sqrt((STATSbv(j).PixelList(:,1)-x1).^2+(
    STATSbv(j).PixelList(:,2)-y1).^2+(STATSbv(j).PixelList(:,3)-z1).^2);
186                     minpix(k) = min(alldist);
187                 end
188                 minBVpix(j) = min(minpix);
189             end
190             borbor(i) = min(minBVpix);
191         end
192         if answer{2} == '3D'
193             NPvol(i) = dxy^2*dz*STATSnp_fill(i).Area;
194         else
195             NPvol(i) = dxy^2*STATSnp_fill(i).Area;
196         end
197         fprintf(np_fid,'%i \t',i);
198         fprintf(np_fid,'%6.4f\t %6.4f\t %6.4f\n', NPvol(i),NPfrac(i),borbor
    (i));
199     end
200
```

```
    if answer{2} == '3D'
        for j = 1:N_bv
            BVvol(j) = dxy^2*dz*STATSbv_fill(j).Area;
        end
    else
        for j = 1:N_bv
            BVvol(j) = dxy^2*STATSbv_fill(j).Area;
        end
    end

    fprintf(SUM_fid,'%s \t %i\t %i\t',char(Filename{f}), N_np, N_np-nnz(
    borbor));
    fprintf(SUM_fid,'%i \t %6.4f\t %6.4f\t',nnz(borbor), sum(NPvol), sum(
    BVvol));
    fprintf(SUM_fid,'%6.4f\t %6.4f\n',sum(Volcoloc), (sum(NPvol)-sum(
    Volcoloc)));
    %clear ind coloc borbor min_borbor max_coloc mass_c mass;
    clear BWbv BWnp

    fprintf(1,' Finished analysis of %s\n',Filename{f});
end
fclose(np_fid);
fclose(SUM_fid);
clear BVnr_Filename NPnr_Filename
```

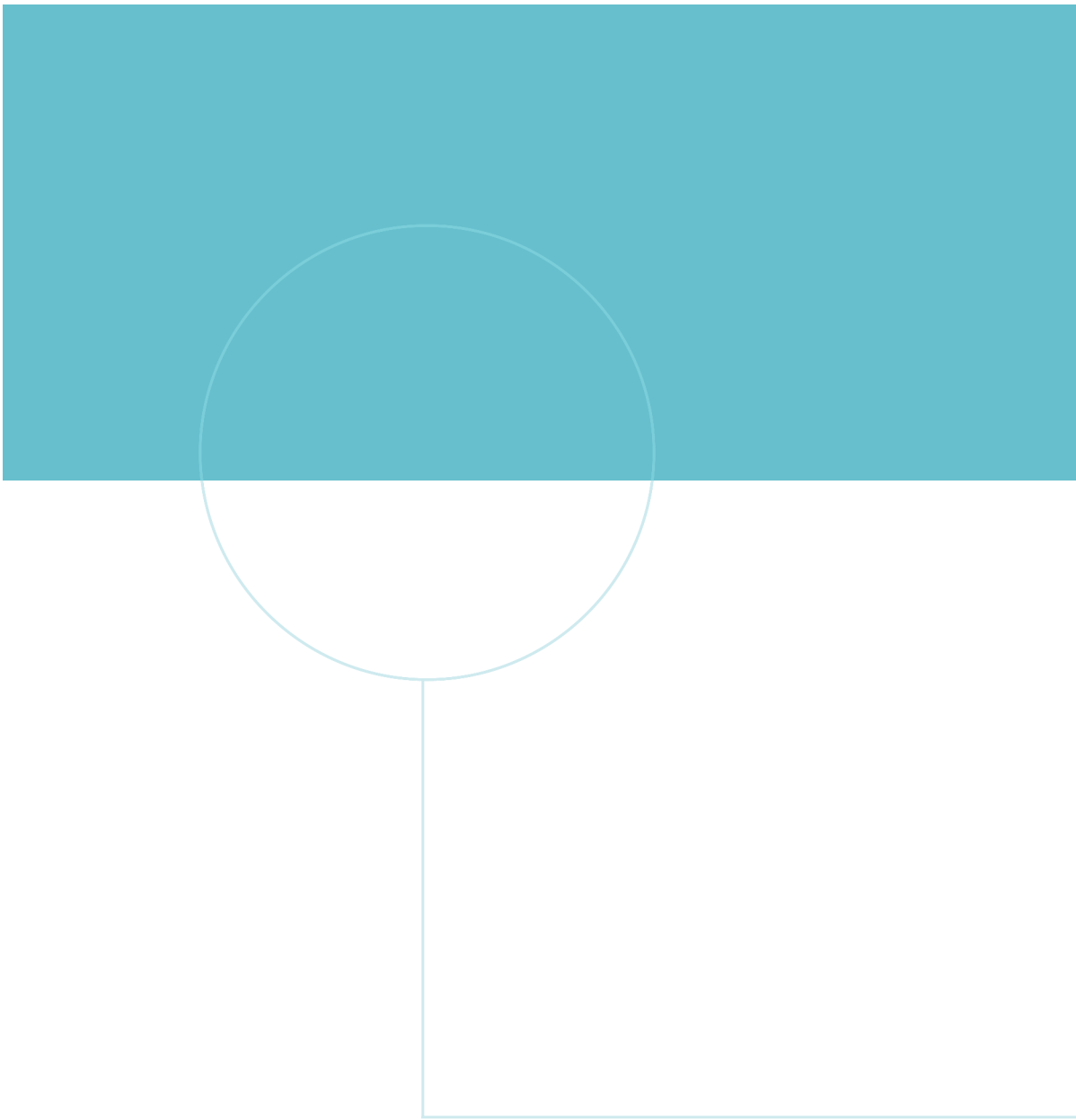

NTNU

Norwegian University of
Science and Technology